SIMULATION OF MOUNTAIN LEE WAVES IN A WIND TUNNEL

by

J. T. Lin and G. J. Binder

Prepared under

U. S. Army Research Grant DA-AMC-28-043-65-G20
U. S. Army Material Command
Washington 25, D. C.

FLUID MECHANICS PROGRAM
ENGINEERING RESEARCH CENTER
COLLEGE OF ENGINEERING
COLORADO STATE UNIVERSITY
FORT COLLINS, COLORADO

Technical Report

SIMULATION OF MOUNTAIN LEE WAVES IN A WIND TUNNEL

by

J. T. Lin and G. J. Binder

Prepared under

U. S. Army Research Grant DA-AMC-28-043-65-G20
U. S. Army Material Command
Washington 25, D. C.

Fluid Mechanics Program
College of Engineering
Colorado State University
Fort Collins, Colorado

December 1967 CER67-68JTL-GJB24

ABSTRACT

Mountain lee-waves were simulated in a wind tunnel where the density stratification was produced by heating the ambient air and cooling the lower boundary. The flow patterns were visualized with smoke and were also determined from mapping of the temperature fields measured point by point with thermocouples and platinum resistance thermometers.

The magnitudes of the velocities were measured with a constant temperature hot-wire anemometer. Since this instrument is also temperature sensitive the compensation of this effect at very low velocities (the actual velocities were about 0.5 ft/sec) was experimentally determined.

The flow was composed of two layers of which the lower one (thickness 7-8 in.) had the large stability. The Froude number was calculated on the basis of the height, stability and average velocity in the lower layer. Two bell-shaped model mountains of the same height (4 in.) but of different horizontal scales were used.

This simulation experiment reproduced all the main features of mountain lee-waves, namely the wave profile, the rotor below the crest of the first wave, the strong velocity increase on the lee slope (1.5-1.8 times the average upstream velocity). Strong turbulence was found

in the upper part of the rotor. The wave length at a fixed elevation of the lee-waves was found to increase linearly with Froude number; the amplitudes did also increase with Froude number.

ACKNOWLEDGEMENTS

The writers wish to thank Drs. J. E. Cermak and L. C. Bartel for their advice and encouragement during the research. Financial support by the Integrated Army Meteorological Wind Tunnel Research Program under Grant DA-AMC-28-043-65-G20 is gratefully acknowledged. Thanks are due to Mr. Robin J. Kung for his help in collecting data and to Mrs. Ann Brown for her typing.

TABLE OF CONTENTS

Chapter		Page
	LIST OF FIGURES	ix
	LIST OF SYMBOLS	xi
I	INTRODUCTION	1
II	REVIEW OF LITERATURE	3
	2.1 Theoretical Studies	3
	2.1.1 Perturbation Theories	4
	2.1.2 Exact Solutions	8
	2.2 Computer Models	9
	2.3 Field Investigations	11
	2.4 Laboratory Simulations	13
III	SIMULATION OF MOUNTAIN LEE-WAVES	14
	3.1 Froude Number - The Non-Dimensional Parameter Governing Gravity Waves	14
	3.2 Modeling of Mountain Lee-Waves	16
	3.2.1 Velocity Requirement	16
	3.2.2 Boundary Conditions	18
	3.3 Viscosity and Thermal Conductivity Effects in the Wind Tunnel	19
IV	EXPERIMENTAL EQUIPMENT AND PROCEDURES	23
	4.1 Wind Tunnel	23
	4.2 Flow Visualization	25
	4.3 Temperature Measurements	26
	4.4 Low-Speed Anemometry in a Temperature Field	29
	4.4.1 Difficulty of Using Previous Results of Hot-Wire Anemometry	29

Chapter Page

4.4.1.1 Review of Hot-Wire Anemometry 29

4.4.1.2 On the Difficulty of Determining Re and Nu Accurately 34

4.4.2 A Simple Temperature Compensation for the Constant Temperature Hot-Wire Anemometer at Low Velocities . 38

4.4.3 Apparatus and Procedure 41

4.4.3.1 Instrumentation 42

4.4.3.2 Calibration Procedure . . . 45

4.4.4 Results 46

4.4.4.1 Uncompensated Calibration Curves 46

4.4.4.2 Evaluation of Exponent n in $(\frac{\theta_f}{\theta_g})^n$ 47

4.4.4.3 Use of the Results 49

4.4.4.4 Accuracy of This Temperature Compensation 50

4.4.4.5 Check of Results 51

V RESULTS AND ANALYSIS 52

5.1 Computation of Froude Number and Reynolds Number 53

5.1.1 Froude Number 53

5.1.2 Reynolds Number 55

5.2 Wave Pattern 55

5.2.1 Flow Visualization Data 55

TABLE OF CONTENTS - Continued

Chapter Page

5.2.2 Constant Temperature Lines 59

5.3 Velocity Distributions, Blocking . . . 60

5.4 The Rotor 62

VI CONCLUSIONS AND SUGGESTIONS FOR FURTHER RESEARCH 64

6.1 Conclusions 64

6.2 Suggestions for Further Research . . . 65

BIBLIOGRAPHY 67

FIGURES 71

LIST OF FIGURES

Figure		Page
1	Flow over a symmetric mountain profile whose width is one critical wave length $2\pi b = 6.28$ km	71
2-3	Horizontal velocities and displacement of potential lines of Hovermale's computer model	72
4-5	Vertical cross section of flow patterns on the lee side of Sierra Nevada	74
6-7	Simulated Sierra Nevada lee-waves of Long's liquid model	76
8	Plan view of Army Micro Meteorological Wind Tunnel	78
9	Sketch of smoke generator and smoke rake	79
10	The circuit of the resistance thermometer and the support instrumentation	80
11	Calibration curve of resistance thermometer	81
12	Instrumentation for velocity measurement.	82
13	Calibration curve of micro wind tunnel. .	83
14-17	Calibration curves of wires at various temperature	84
18-21	Partly compensated calibration curves for wires	88
22	Values of exponent n as a function of air temperatures for four different wires	92
23	Values of $f(\theta_g)$ as a function of air temperature	93
24-27	Temperature compensated calibration curves for wires	94

LIST OF FIGURES - Continued

Figure		Page
28	Temperature compensated calibration curve for wire with Heat Flux System Anemometer	98
29-30	Dimensions of simulated mountain models.	99
31	Undisturbed temperature profile of flow with Fr = 0.308	101
32-39	Observed flows over models	102
40	Lee-wave lengths at different elevations as a function of Froude number	110
41	Lee-wave amplitudes at different elevations as a function of Froude number . .	111
42	Temperature profiles of flow with Fr = 0.254	112
43-48	Constant temperature lines and velocity profiles of flows	113
49	Sketch of lower level streamline of Queney's and Scorer's solution	119
50	Velocity fields of lee-waves	120

LIST OF SYMBOLS

Symbol	Definition or Description	Dimension
b	Half width in $\zeta_o(x) = \frac{a^2b}{x^2 + b^2}$	L
c	Sound speed	LT^{-1}
C_p, C_v	Specific heat at constant pressure, volume	QFT^2L^{-1}
d	diameter of wire	L
E, e	Voltage	V_o
Fr	Froude number, $\frac{V}{(gH \frac{\Delta\rho}{\rho})^{\frac{1}{2}}}$	----
g	Acceleration of gravity	LT^{-2}
H, L	Characteristic lengths	L
I	Electric current	$V_o\Omega^{-1}$
j	wave number	L^{-1}
k	Thermal conductivity	$QT^{-1}L^{-1}H^{-1}$
k''	Thermal diffusivity	L^2T^{-1}
ℓ_c	Cold length of hot wire	L
ℓ_e	Effective length of hot wire	L
Nu	Nusselt number, $\frac{\alpha L}{k}$	----
p	Pressure	FL^{-2}
$\underline{q}$	Velocity vector	LT^{-1}
Pr	Prandtl number, $\frac{\nu}{k''}$	----
R	Electric resistance	Ω
Re	Reynolds number, $\frac{VL}{\nu}$	----

LIST OF SYMBOLS - Continued

Symbol	Definition or Description	Dimension
S	Vertical density gradient	L^{-1}
t	Time	T
U	Mean velocity in x component	LT^{-1}
u,w	Velocities in x, z components	LT^{-1}
u',w'	Perturbation velocities in x, z components	LT^{-1}
V	Characteristic velocity	LT^{-1}
x,z	Cartesian coordinates	L
α	Heat-transfer coefficient	$QL^{-2}H^{-1}T^{-1}$
β	Thermal resistivity coefficient	H^{-1}
γ	Lapse rate of temperature $\frac{d\bar{\theta}}{dz}$	HL^{-1}
γ'	$\gamma' = \frac{C_p}{C_v}$	----
γ^*	Adiabatic lapse rate of temperature $\gamma^* = \frac{g}{C_p}$	HL^{-1}
δ	Thickness of boundary layer	L
θ	Temperature	H
θ_p	Potential temperature	H
μ	Dynamic viscosity	$FL^{-2}T$
ν	Kinematic viscosity	L^2T^{-1}
ρ	Density	FT^2L^{-4}
σ	Stability, $\frac{\gamma^*-\gamma}{\theta}$	FT^2L^{-5}
ψ	Stream function	L^2T^{-1}
∇	Gradient operator	L^{-1}

Symbol	Definition or Description	Dimension
∇^2	Laplace operator	L^{-2}
λ	Wave length	L

** F: force, L: length, T: time, H: temperature,
Q: heat, V_o: voltage, Ω: ohm

CHAPTER I

INTRODUCTION

Glider pilots had been aware of the strong, sometimes treacherous, ascending and descending air currents over mountains, and meteorologist had analysed the effects of the perturbation of the wind by the topography on local climates, long before the general problem of air flow over mountains had received much attention from hydrodynamicists. With the rapid growth of commercial aviation some thirty years ago, it soon was noticed that a large percentage of accidents occurred over and near high mountains. The search for causes of these accidents naturally leads to investigations of the general problem of air flow over mountain barriers.

The problem has since then been studied by all means available: analytically, experimentally by field and model studies and by use of large computers. All studies confirm the existence of large oscillations of the air stream behind the mountain, the so called lee-waves. Yet, although much light has been shed on this question, the results are only fragmentary still, for the problem is quite complex - as are all problems of geophysical hydrodynamics - so that only special cases may be treated. In addition, all approaches have inherent limitations.

The majority of the analytical studies are based on linearized equations and the few that are not refer to special boundary conditions. Computer size restricts the scope of numerical models. Field studies are very expensive, therefore they cannot be exhaustive. Laboratory simulations are not easily realized and the extension of their results to the prototype is not a simple matter. Large zones remain thus obscure in the picture of air flow over mountains.

So far, only two laboratory simulations (Abe, 1; Long, 20) of mountain lee-waves have been attempted. This field remains thus wide open. Since the large wind tunnel of the Fluid Dynamics and Diffusion Laboratory at Colorado State University has the capability of producing stratified flows - an essential feature when atmospheric motions are modeled - such an investigation appeared very promising.

The previous laboratory investigations concerned themselves only with the flow pattern, as most of the theoretical studies did. To our knowledge detailed measurements of the velocity field have not been taken in a mountain lee-wave flow, so that an effort in this direction seemed particularly worthwhile.

This, however, was not a simple routine task because the instrumentation for measuring very low velocities in a temperature gradient had to be developed first.

The original work reported here divides then into two main parts, first the development of the instrumentation, i.e., the temperature composition of the hot-wire anemometer at very low speeds, and second the flow pattern and the velocity field in some typical lee-wave situations.

CHAPTER II

REVIEW OF LITERATURE

In order to show the relevance of this work, the results obtained thus far will first be summarized and the limitations of the various methods will be pointed out. This review does not pretend to be exhaustive. It rather attempts to show the main axes along which the investigations on mountain lee-waves have proceeded. An excellent summary of most of the work on lee-waves is given in the Technical Note No. 34 of the World Meteorological Organization entitled "The Air Flow Over Mountains" by P. Queney et al.

2.1 Theoretical Studies.

It should first be pointed out that all theoretical studies, analytical and computational, assume the flow to be inviscid and laminar. These assumptions lead to considerable simplification of the equations of motion which otherwise would be intractable.

Viscosity plays a significant role only in a thin layer near the earth's surface and its influence may be ignored elsewhere. It is therefore not a relevant parameter in the air flow over mountains. The restriction imposed by the assumption of laminar flow is more difficult to assert. So far, not even the case of a constant eddy viscosity could be treated analytically.

With these assumptions of an ideal fluid, the continuity, momentum, and energy equations - this latter one reducing to the adiabatic equation and further to the condition of incompressibility if the flow is incompressible - may be written as

$$\begin{aligned}
&\frac{\partial}{\partial x}(\rho u) + \frac{\partial}{\partial z}(\rho w) = 0 \\
&u\frac{\partial u}{\partial x} + w\frac{\partial u}{\partial z} = -\frac{1}{\rho}\frac{\partial p}{\partial x} \\
&u\frac{\partial w}{\partial x} + w\frac{\partial w}{\partial z} = -\frac{1}{\rho}\frac{\partial p}{\partial z} - g \\
&u\frac{\partial p}{\partial x} + w\frac{\partial p}{\partial z} = c^2\left(u\frac{\partial \rho}{\partial x} + w\frac{\partial \rho}{\partial z}\right) \quad .
\end{aligned} \tag{2.1}$$

This is the basic system of equations that has to be solved. The boundary conditions to which this system is subjected must prescribe the values of u , w , ρ , and p in some plane far upstream of the mountain, say $x = -\infty$, and in the planes $z = 0$ (lower boundary condition) and $z = +\infty$ or $z = h$ (upper boundary condition). The variety of upstream and upper boundary conditions that exist in nature points out immediately the complexity of the problem.

2.1.1 Perturbation Theories.

If the various quantities above are split into basic variables, which would describe the flow if it were not disturbed by the mountain, and perturbations caused by the mountain, as for instance

$$u = U + u' \quad ,$$

and if it is assumed that all perturbations and their derivatives are small compared to the corresponding values in the base flow (linearization assumption), one arrives by elimination at the partial differential equation for the vertical velocity

$$\nabla^2 w_1 + f(z)\, w_1 = 0 \tag{2.2}$$

where $w_1 = \left(\frac{\rho}{\rho_o}\right)^{\frac{1}{2}} w'$ is the modified perturbation velocity

$$f(z) = \frac{\sigma g}{U^2} + \frac{S}{U}\frac{dU}{dz} + \frac{1}{4}S^2 + \frac{1}{2}\frac{dS}{dz} - \frac{1}{U}\frac{d^2U}{dz^2}$$

$$S = -\frac{1}{\rho}\frac{d\rho}{dz} \tag{2.3}$$

$$\sigma = S - \frac{g}{c^2} = \frac{1}{\theta_p}\frac{d\theta_p}{dz} \quad .$$

If $z = \zeta_o(x)$ defines the mountain profile, the tangency of the velocity to the mountain implies when the perturbation approximation is used

$$\frac{d\zeta_o}{dx} = \frac{w'(x,o)}{U(o)} \quad . \tag{2.4}$$

If the upper boundary condition prescribed is the vanishing of the kinetic energy of the perturbation at infinite heights, one arrives at

$$\lim_{x^2+z^2\to\infty} w_1 = 0 \quad . \tag{2.5}$$

A difficulty arising in the solution of this system is the occurrence of so called "free" or "resonance" waves. These are waves of arbitrary amplitude which satisfy the differential equation, the upper boundary condition and which automatically vanish at ground level. This indeterminateness can be lifted by either requiring all waves to vanish far upstream, or by introducing a viscosity which is then permitted to approach zero, or by applying the Sommerfeld radiation condition.

This difficulty of uniqueness does not arise when the non-stationary problem is considered. Wurtele (30) and Queney (25) have shown that the time dependent solution asymptotically approaches the steady-state solution.

A good approximation of $f(z)$ is

$$f(z) = \frac{\sigma g}{U^2} - \frac{1}{U}\frac{d^2U}{dz^2} \quad . \tag{2.6}$$

It is evident that the differential Eq. 2.2 can only be solved in closed form when $f(z)$ takes some particular functional forms. The simplest case is of course when $f(z)$ is constant, and this may be achieved by taking $U(z) = \text{const.}$ and $\sigma(z) = \text{const.}$, i.e., a uniform velocity and a constant temperature.

In this form the problem was first attacked by Lyra (21), who used a Green's function to solve the differential equation. He used a rectangular hill, a semi-infinite plateau as well as a concentrated obstacle at the origin as disturbing mountain profiles. The solution he obtained was expressed as a series of Bessel functions. It clearly showed a flow pattern with periodic oscillations. Lyra must be given credit for having been the first to show in a rigorous way the existence of mountain lee-waves.

In his beautiful report, Queney (23) used a Fourier transform technique to reduce Eq. 2.2 to an ordinary differential equation

$$\frac{d^2w_1}{dz^2} - (j_s{}^2 - j^2) \, w_1 = 0 \tag{2.7}$$

where

$$j_s{}^2 = f(z) = \frac{\sigma g}{U^2} \quad .$$

Queney introduced a bell-shaped mountain of the type

$$\zeta_o(x) = \frac{a^2 b}{x^2 + b^2}$$

He pointed out that lee-waves only exist when

$$j_s \doteq \frac{1}{b} \quad .$$

This solution is shown in Fig. 1.

These solutions of Lyra and Queney displayed waves covering a continuous spectrum, whereas observations showed that mountain lee-waves are essentially composed of one or two harmonic waves. Wurtele (31), however, by taking a velocity profile with constant shear, transformed Eq. 2.7 into a Bessel equation and showed that the solution had resonance waves whose wave length increased with altitude. At ground level these waves had wave lengths comparable to the dimension of the mountain.

Scorer (28) considered an atmosphere composed of two layers in which $f(z)$ assumed two different values. In this two layer model the boundary condition at the interface gives rise to resonance waves. Palm (22) considered a three layer model extending into the stratosphere and obtained a discrete number of resonance waves with amplitudes depending on altitude. He pointed out that his results were consistent with observations of the Mother of Pearl clouds.

Despite the simplifying assumption of a small perturbation produced by the mountain, the problem can only be solved in some particular cases. It should be added, that it has been shown that the solutions of some linearized equations differ from the exact solution of the corresponding non-linear differential equations to a degree such as not even being good first approximations. Numerical predictions of wave lengths and amplitudes based on solutions from perturbation theories should therefore be accompanied with reservations.

2.1.2 Exact Solutions.

Long (18) was the first to study the non-linear problem. He derived the following differential equation of the motion for an incompressible fluid.

$$\nabla^2 z_o + \frac{1}{2}\left((\nabla z_o)^2 - 1\right)\frac{d}{dz}\ln(\rho U^2) - \frac{g}{\rho U^2}\frac{d\rho}{dz_o}(z_o - z) = 0 \qquad (2.8)$$

where z_o is the altitude far upstream of the particle at (x,z).

U is the velocity distribution far upstream. Long was able to reduce this equation to a linear partial differential equation and then to find a solution in case of a rigid upper boundary at $z = H$ and of a linear density distribution. A remarkable feature in one case is the existence of streamlines which partly fold back on themselves.

Yih (32) showed that Eq. 2.8 may be considerably simplified by the transformation

$$\psi' = \int \left(\frac{\rho}{\rho_o} \right)^{\frac{1}{2}} d\,\psi \qquad (2.9)$$

into

$$\rho_o \nabla^2 \psi' - gz \frac{d\rho}{d\psi'} = F(\psi') \quad , \qquad (2.10)$$

where ψ is the stream function, ψ' is the associated stream function obtained by the above transformation and ρ_o is a reference density. $F(\psi')$ is the left hand side of Eq. 2.10 evaluated far upstream. This equation becomes completely linear if far upstream the vorticity of the associated flow is zero and the density gradient is constant.

Kao (13, 14) obtained a solution to this equation for the flow over a barrier with a stagnant zone upstream of the obstacle. His solution displays not only the characteristic lee-waves but also closed streamlines below the wave crests, which may be identified with the so-called rotor which has frequently been observed in nature.

2.2 Computer Models.

Foldvik and Wurtele (7) were the first workers to attempt a computer experiment. Because of the impossibility of prescribing an a priori value to the stream function at the downstream and on the upstream grid points, Foldvik and Wurtele decided to solve the non-stationary problem, i.e., a disturbance in the form of an obstacle suddenly appearing at time zero. Since the perturbation travels at finite speed, the end points remain undisturbed until this perturbation arrives there. But then the disturbance reflects entirely back into the flow. The computation must be stopped at that time, since, after the reflection has occurred, the result is meaningless. The salient feature of the result of Foldvik and Wurtele is one very strong and steep wave in the immediate lee of the mountain. The non-linear effect seems to decrease the hangauf wind and to considerably intensify the downslope winds.

Hovermale (12) used the same idea to solve the problem of air flow over a bell-shaped barrier. In his analysis, a specified system xyp'', instead of the ordinary system xyp, was obtained by the hydrostatic assumption and the linear transformation,

$$p'' = \frac{p - p^{**}}{p^{*} - p^{**}} \quad , \tag{2.11}$$

in which p^{*} is the pressure at ground level and p^{**} is the pressure at a certain height. Through this transformation, the ground becomes the surface: $p'' = 1$, a very convenient definition of the lower boundary condition for the computer.

Hovermale encountered the difficulty already met by Foldvik and Wurtele concerning the upstream and downstream boundary conditions. He too used cyclic boundary conditions which unfortunately are the only available technique to solve such a problem by the relaxation method. One should be aware of the fact that this restricts a given streamline to entering and leaving the grid at the same level and corresponds to successive, equally-spaced, parallel ridges.

Hovermale's results (Figs. 2 and 3) also show very strong downslope winds. The upstream fronts of the waves located right above the lee-slope of the mountain are very steep, some even folding over slightly, which gives the streamlines the appearance of hydraulic jumps.

2.3 Field Investigations.

The World Meteorological Organization Technical Note "Airflow over Mountains" (see Ref. 26), mentioned earlier, reports half a dozen systematic field observations. The earliest work is due to Kuettner (17), who explored the mountain air currents in the Alps with gliders in the 1930s. From visual observations of clouds, Kuettner was able to present a correct description to mountain lee-waves.

The most systematic field study is the impressive Sierra Wave Project (see Ref. 11), undertaken to investigate the nature of the waves over the Sierra Nevada. The data were mainly provided from instrumented sailplanes which were tracked by theodolites and/or radar. Powered aircraft were also used at a later stage of the project. The data reduction made use of the continuity equation and of the assumptions of steady two-dimensional flow to obtain the streamlines. Figures 4 and 5 show two examples of the flow pattern obtained corresponding to Froude numbers of 0.14 and 0.24 respectively.

The main results of this field investigation are summarized below (see Ref. 26):

(i) In general, a strong wave corresponded to a long wave length, and a weak wave to a short wave length.

(ii) In comparing the streamline field with the field of potential temperature, the flow was found to be adiabatic with temperatures low in the crests and high in the troughs at all levels. Thus, the occurrence of lenticular and roll clouds on the lee side of a mountain indicates the existence of lee-waves and the position of the wave crests.

(iii) The maximum horizontal wind was in the troughs below and in the crests above the roll cloud zone.

(iv) Finally, strong lee-waves were associated with air flow having pronounced inversions in mid-troposphere (3,500 to 6,000 m) and strong vertical wind shear, around 50m/sec at 9,000 to 12,000 m.

2.4 Laboratory Simulations.

Only three laboratory investigations of the flow of a stratified fluid over a barrier have been carried out. Abe (1) investigated the formation of mountain clouds by Mount Fujiyama, which is an almost conical mountain. He also studied the air current associated with these mountain clouds. In his experiments, a model geometrically similar to Mount Fujiyama, scaled in the ratio 1:50,000, was used. The experiments were all conducted at the same Reynolds number on the assumption that molecular viscosity in the model corresponded to eddy viscosity in the atmosphere. An attempt was made to introduce velocity and temperature stratification, but the Froude number was not consistent between model and prototype flows.

Long (20) conducted simulation experiments with water in which the density stratification was obtained by additions of salt. In order to avoid turbulent mixing in the flow, Long kept the liquid stationary and moved the barrier through it. Figures 6 and 7 are flow patterns obtained in the simulation experiments of flows over the Sierra Nevada. These flow patterns were in good agreement with the results of the Sierra Wave Project. In other experiments (see Ref. 19) the agreement between theory and experiment was remarkable.

Suzuki and Yabuki (29) conducted similar experiments with as many as 7 different layers.

CHAPTER III

SIMULATION OF MOUNTAIN LEE-WAVES

The principle of similarity is used to determine the simulation requirements for the modeling of mountain lee-waves in a wind tunnel.

3.1 Froude Number - The Non-Dimensional Parameter Governing Gravity Waves.

The Navier-Stokes equations for incompressible and laminar flow on which the coriolis force has negligible effect (case of flows of small horizontal scale) is:

$$\rho \left(\frac{\partial \underline{q}}{\partial t} + \underline{q} \cdot \nabla \underline{q} \right) = - \nabla p - \Delta \rho \underline{g}$$

$$+ \mu \left(\nabla^2 \underline{q} + \frac{1}{3} \nabla (\nabla \cdot \underline{q}) \right) \quad . \qquad (3.1)$$

Define non-dimensional variables as follows:

$$x_i = Hx_i' , \quad t = \frac{H}{V} t' , \quad q_i = Vq_i'$$

$$p = \rho_o V^2 p' , \quad \rho = \rho_o \rho' , \quad \text{and} \quad \underline{g} = g \, \underline{g}' \qquad (3.2)$$

where the prime and the subscript o indicate the dimensionless and the reference quantity respectively, where $\underline{g}'$ is the unit vector along the acceleration of gravity and $\underline{q}$ is the total velocity vector. By use of relations (3.2), the N-S equations may be written in non-dimensional form

$$\left(\frac{\partial \underline{q}}{\partial t} + \underline{q}' \cdot \nabla \underline{q}' \right) = - \frac{1}{\rho'} \nabla p' + \frac{Hg\Delta\rho_o}{\rho_o V^2} \frac{\Delta\rho'}{\rho'} \underline{g}'$$

$$+ \frac{\mu}{\rho_o VH} \frac{1}{\rho'} \left(\nabla^2 \underline{q}' + \frac{1}{3} \nabla (\nabla \cdot \underline{q}') \right) . \tag{3.3}$$

It may be seen from the last two terms of the right hand side of Eq. 3.3 that the viscosity effect is small compared to the gravity effect if the velocity is relatively low and if the scale of motion is comparatively large. When the gravity effect is dominant, the parameter governing the flow is then the Froude number, Fr , defined as

$$\frac{1}{Fr^2} = \frac{gH\Delta\rho_o}{\rho_o V^2} . \tag{3.4}$$

It should be remarked here that ρ_o in $(1/\rho_o)$ $(\Delta\rho_o/H)$ or in $(1/\rho_o)$ $(d\rho_o/dz)$ should be changed to the potential density $\tilde{\rho} = \frac{\rho}{(p/p_o)^{1/\gamma}}$, (or to the potential temperature) if the fluid is compressible as, for instance, the atmosphere is. The expression $\sigma = (1/\tilde{\rho})$ $(d\tilde{\rho}/dz)$ is sometimes called the stability. The Froude number may be written in terms of σ as:

$$Fr = \frac{V}{H \ (g\sigma)^{1/2}} . \tag{3.5}$$

Of the wind-tunnel scale, the changes in hydrostatic pressure are quite small, so that:

$$\frac{1}{\rho} \frac{d\rho}{dz} \simeq - \frac{1}{T} \frac{dT}{dz} >> \frac{1}{p} \frac{dp}{dz}$$

and

$$\sigma = \frac{1}{\rho} \frac{d\rho}{dz} = - \frac{1}{T} \frac{dT}{dz} \quad . \qquad (3.6)$$

3.2 Modeling of Mountain Lee-Waves.

3.2.1 Velocity Requirement.

The first similitude requirement for a modeling experiment on gravity waves is the equality of Froude numbers for the model (subscript m) and the prototype (subscript p).

$$(Fr)_m = (Fr)_p$$

or (3.7)

$$\frac{V_m}{H_m (g_m \sigma_m)^{\frac{1}{2}}} = \frac{V_p}{H_p (g_p \sigma_p)^{\frac{1}{2}}} \quad .$$

g_m could be different from g_p if the experiment were performed in a rotating system where the body force originated from the centrifugal effect and where the Rossby number due to coriolis effects should be taken into account. However, for the wind-tunnel experiment,

$$g_m = g_p$$

so that

$$\frac{V_m}{V_p} = \frac{H_m}{H_p} \left(\frac{\sigma_m}{\sigma_p} \right)^{\frac{1}{2}} \quad . \qquad (3.8)$$

H_m and σ_m depend on the wind-tunnel characteristics, the thickness of the stratified layer and the temperature difference that may be maintained for the stratification. In the experiments described here

$$H_m = 4 \text{ in.} = 10^{-1}\text{m}$$

$$\sigma_m = 0.6 \text{ m}^{-1} \quad .$$

If a one km high mountain is modeled,

$$H_p = 10^3\text{m} \quad .$$

A typical value of the stability in a lee-wave situation is

$$\sigma_p = 1.5 \times 10^{-5}\text{m}^{-1} \quad .$$

This yields

$$\frac{V_m}{V_p} = 2 \times 10^{-2} \quad .$$

Field observations have shown that mountain lee-waves generally occur for (see Ref. 26 pp. 48 and 55)

$$7\text{m/sec} < V_p < 20\text{m/sec} \quad ,$$

which imposes the following limits on the velocity in the tunnel:

$$14 \text{ cm/sec} < V_m < 40 \text{ cm/sec} \quad . \qquad (3.9)$$

These velocities, although quite small, could be maintained in the wind tunnel at Colorado State University. However, the measurement of such small velocities in a temperature gradient revealed itself to be much more than a mere routine experimental task.

3.2.2 Boundary Conditions.

Complete similarity between model and prototype flow also requires the matching of the boundary conditions. Strictly speaking, this imposes geometric similarity and similar distributions of velocity and stability upstream, at ground level and at a certain height. To satisfy all these conditions would require a very particular wind tunnel. The facility at Colorado State University, which was not designed for this purpose, does not have the necessary degree of freedom for the adjustment of all these parameters.

However, since the purpose of this research was to investigate the possibility of a wind-tunnel simulation and the general features of lee-waves rather than to attempt to model any particular flow over mountains, these boundary conditions did not need to be strictly prescribed.

Geometric similarity in a general study such as this poses no problem. A bell-shaped mountain profile was chosen because it was used in several theoretical investigations. The upstream conditions, which in the Colorado State University wind tunnel are those which are the natural development of the velocity and temperature boundary layers produced by hot air flowing over a cold plate, can be accepted as corresponding to some atmospheric motion. A feature such as the stagnant zones at higher elevations obtained in the wind tunnel supposedly because of gravity currents may, however, not be commonly encountered in the atmosphere.

The tunnel condition differing the most from that of the atmosphere is the upper boundary condition of stability or stratification. In the tunnel outside the thermal boundary layer the density gradient is zero, whereas in the atmosphere this gradient increases markedly at the tropopause. It may, however, be argued that the effect of this zone on the lower layer may be small if the difference in height between them is large. The model test of this study simulates only the lower levels of the atmosphere.

The World Meteorological Organization Technical Note (see Ref. 26) states on page 47: "In air-streams containing lee waves, there is evidence that the air has greater static stability than the average at low levels surmounted by air of lesser stability above..... It seems an essential requirement, at least for strong waves, that there should be marked stability at levels where the air is disturbed by the mountain." Precisely such conditions exist in the wind tunnel used in the present study. The density gradient is indeed large at lower levels and then tends toward zero (see Fig. 23).

3.3 Viscosity and Thermal Conductivity Effects in the Wind Tunnel.

In the atmosphere, the effects due to viscosity and thermal diffusivity are negligible compared to those of gravity and inertia because of the large scale of the motion. These molecular effects cannot, however, be disregarded in model experiments which are necessarily performed on a small scale.

The question arises there whether viscosity and thermal diffusivity will or will not significantly distort the lee-wave pattern in the wind tunnel? This was already discussed by Cermak et al. (Ref. 3, pp. 47-51) who arrive at the conclusion that, despite the non-vanishing character of molecular effects, they have a minor influence on the flow in a short region in the lee of the model mountain.

By slightly modifying the arguments of Ref. 3, one may first calculate the change in velocity and thermal boundary-layer thickness - which are of the same order since the Prandtl number for a gas is nearly one - occurring over the distance of one wave length. The growth of a laminar boundary layer is given by

$$\delta \propto x^{\frac{1}{2}} \quad ; \tag{3.10}$$

hence

$$\frac{\Delta\delta}{\delta} = \frac{1}{2} \frac{\Delta x}{x} \quad . \tag{3.11}$$

The wave length of the lee-waves obtained in the tunnel is typically of the order of 2 ft (see Figs. 32-39). If the model mountain is at a distance of 20 ft from the leading edge of the plate, it follows that

$$\frac{\Delta\delta}{\delta} \simeq \frac{1}{20} \quad ; \tag{3.12}$$

i.e., the relative increase in boundary-layer thickness over one wave length is only 5%.

An alternative way of showing the predominance of the gravity effect over the influence of molecular effects is to compare the vertical velocities due to boundary layer growth to those generated by the lee-wave effect. The maximum vertical velocity W_b produced by boundary layer growth is (see Ref. 27 p. 120)

$$\frac{W_b}{U} = 0.8 \left(\frac{\nu}{Ux} \right)^{\frac{1}{2}} . \qquad (3.13)$$

Since the vertical velocities in a lee-wave W_m are of the same order as the horizontal free stream velocity,

$$\frac{W_b}{W_m} = 0.8 \left(\frac{\nu}{Ux} \right)^{\frac{1}{2}} . \qquad (3.14)$$

Thus for $x = 20$ ft , $U = 0.3$ ft/sec , and $\nu = 1.5 \times 10^{-4}$ ft^2/sec

$$\frac{W_b}{W_m} = 5 \times 10^{-3} \qquad (3.15)$$

Hence, the vertical velocity due to boundary layer growth is less than one percent of that due to the lee-wave. This result again confirms the dominant effect of gravity over molecular effects.

It should be emphasized, however, that this conclusion only holds over short longitudinal distances. On the other hand, it would also break down if separation were to occur with production of large scale eddies and turbulence.

But this occurrence, it may be added, is retarded by the very existence of density stratification which results in a considerable velocity increase on the lee side of the model.

CHAPTER IV

EXPERIMENTAL EQUIPMENT AND PROCEDURES

As mentioned earlier, this study endeavored to obtain not only the flow pattern downstream of a mountain barrier placed in a stratified flow but also measurements of the velocity. This latter task proved to be quite difficult because it required the measurement of very low velocities in a temperature field. As shown by Kung and Binder (16), the most reliable and convenient low-speed anemometer is the hot-wire anemometer. But this instrument is very sensitive to temperature at low velocities; this effect had therefore to be analyzed before this anemometer could be used. The core of this chapter is devoted to this instrumentation problem. Described herein are also the characteristics of the wind tunnel used to simulate mountain lee-waves and the flow visualization techniques used to reveal the flow patterns.

4.1 Wind Tunnel.

For the study of simulated mountain lee-waves, a stably stratified flow is necessary. In this investigation, the Army Meteorological Wind Tunnel at the Colorado State University Fluid Dynamics and Diffusion Laboratory was used for this purpose.

Figure 8 shows a plan view of this wind tunnel. The wind tunnel is of the closed circuit type and has a test section 80 ft long and 6 ft by 6 ft in cross section. The second half of the test section floor may be either heated electrically or cooled by circulating cold brine through a system of pipes installed in the floor. The ambient air temperature in the wind tunnel can be controlled by a system of heating or cooling coils installed in the return section through which the circulating air passes. Since a stably density-stratified flow was required in this investigation, the bottom plate was cooled to 32°F and the ambient air temperature in the free stream was heated to 85°F to 125°F.

As seen in the chapter on simulation, the Froude number modeling requires velocities between 0.5 and 1 ft/sec in the wind tunnel. Although the large tunnel was not designed for such low velocities, the velocity could be reduced to 0.5 ft/sec by putting two screens with 16% open area at both ends of the test section. But the flow at these low velocities was difficult to control. Above all, a reverse flow from downstream to upstream occurred in the test section in the region close to the tunnel floor. This reverse flow appears to be a gravity current. Indeed, the heavier air in the vicinity of the plate tends to flow down to lower elevations. The upstream contraction of the wind tunnel is such a region, and the density difference is apparently sufficient to overcome the viscous drag of the main air stream. No lee-waves could be observed in this situation.

Fortunately, by adjusting the pitch control of the fan, this difficulty could be overcome by running the tunnel backward so that the density current was in the same direction as the main flow.

4.2 Flow Visualization.

To render the streamlines visible, smoke was used. In order to avoid any appreciable disturbance to the flow by the introduction of smoke, it was desirable to be able to control the rate at which the smoke was introduced.

The smoke generator shown on Fig. 9 was developed for this purpose. It consists of a cylindrical 250 w "chromalox" electroheater, manufactured by the Edwin L. Wiegand Company, mounted into a closed pyrex jar. The lateral surface of the heater element is insulated from the surrounding atmosphere with glasswool; only the end plane is left exposed. The heating current is adjusted with a Variac; vacuum pump oil is allowed to drip at a controlled rate onto the exposed surface where it is partly vaporized. The oil droplet suspension is evacuated from the vessel by air originating from a compressed air tank with a flow rate adjusted by means of the tank valve. The smoke is passed through a second vessel to condense the heavier droplets which otherwise would condense in the feed-lines and form liquid plugs. In this smoke generator, all the inputs - heat, oil and air - can thus be controlled at will.

The smoke was introduced into the main flow through a rake. Once released into the main flow from the outlets of the rake, the smoke did fall sharply downward rather than staying in the horizontal plane of release as was desired. But after some distance, the smoke streams would approximately travel in horizontal flows. Apparently, the heavier droplets with large fall velocities (compared to very small ambient horizontal velocity required by the very nature of the experiment) created a down-draft strong enough to entrain the lighter droplets. With increasing distance downstream, owing to their larger fall velocities, they would, however, separate from the main smoke plume which would then be subjected only to the horizontal entrainment of the main flow. When the smoke rake was then placed far enough upstream, the smoke did approach the model horizontally. It was then no longer possible to have neat smoke filaments, since diffusion had had time to disperse the tracer. Yet the differences in smoke concentrations were sufficiently pronounced for the purpose of visual observation and the taking of still or even moving pictures.

4.3 Temperature Measurements.

Since the density stratification was obtained by temperature difference, the temperature profiles had to be measured so that the density distributions could consequently be calculated. In a steady incompressible nonhomogeneous fluid, constant density lines are stream lines, thus constant temperature lines indicate the flow pattern. But since molecular diffusion cannot be neglected on the laboratory scale, this is only approximately true; the temperature of a particle does not remain exactly constant, so that the constant temperature lines only approximate the stream lines. It was therefore desirable to check this flow pattern based on constant temperature line against that obtained by flow visualization. As shall be seen later, the temperature compensation of the constant temperature hot-wire anemometer also required the measurement of temperature.

The copper-constantan thermocouple was found to be an accurate thermometer, but as it was traversed across the temperature boundary layer, it had very slow response which rendered the measurements very tedious. This sluggishness may be attributed to heat transfer along the thermocouple wires which were at a different temperature than the junction.

The resistance thermometer developed by Chao and Sandborn (4) is highly sensitive to temperature and insensitive to velocity and has fast response; therefore, it was preferred to the thermocouple.

The circuit of the resistance thermometer is shown in Fig. 10, which also shows the support instrumentation. The circuit for measuring mean temperature is a Wheatstone bridge with a constant current supplied by a battery. The resistance wire itself is a 90% platinum - 10% rhodium alloy and has a nominal diameter of 2.5×10^{-5} in. The wire resistance ranged from 900 to 1100 Ω.

The transducing principle of the resistance thermometer is based on the temperature-resistance equation,

$$R_1 = R_o \left(1 + \beta (\theta_1 - \theta_o) \right) \qquad (4.1)$$

in which subscripts 1 and o indicate that the physical quantitites are measured at the temperatures θ_1 and θ_o, and β is the temperature-resistivity coefficient. Therefore, if R_1 at θ_1 are measured, θ_2 can be calculated from R_2 as follows

$$\theta_2 - \theta_1 = \frac{R_2 - R_1}{\beta R_o} . \qquad (4.2)$$

Now, if a constant current is supplied to the wire, θ_2 can be inferred from the voltage change across the wire:

$$\theta_2 - \theta_1 = \frac{I(R_2 - R_1)}{\beta\ IR_o} = \frac{e_2 - e_1}{\beta\ IR_o}$$

or

$$\frac{e_2 - e_1}{\theta_2 - \theta_1} = \frac{\Delta e}{\Delta \theta} = \beta\ IR_o \qquad (4.3)$$

From Eq. 4.3, it is seen that the sensitivity of this thermometer $\Delta e/\Delta\theta$ is proportional to I and R_o. A high wire resistance can easily be obtained by using a thin, long wire. The current, however, must be kept small, for if too high a current I is supplied to the wire it becomes "hot" and therefore sensitive to velocity. According to Chao and Sandborn, for a wire of 900 Ω, the temperature increase above the ambient air resulting from a heating current of 0.1 mA is only about 0.2°F and the sensitivity $\Delta e/\Delta\theta$ of such a wire is about 0.07 mV/°F.

Actually, Eq. 4.3 is not used in practice to obtain the voltage-temperature relation, but each wire is calibrated directly against a standard, such as a thermocouple. Figure 11 shows an example of a calibration curve.

4.4 Low-Speed Anemometry in a Temperature Field.

As mentioned previously, the most difficult experimental problem met in the laboratory study of mountain lee-waves was the measurement of the low velocities (say less than 1 ft/sec) in a temperature field required to produce such flows. If the hot-wire anemometer was known to be suitable for measuring such velocities, little could be said about the temperature effects on it at these velocities. The solution of this instrumentation problem is now described.

4.4.1 Difficulty of Using Previous Results of Hot-Wire Anemometry.

4.4.1.1 Review of Hot-Wire Anemometry.

The heat transfer from a heated wire in a continuum and forced convection flow (Goldstein, 8) may be expressed in the dimensionless form

$$\mathrm{Nu} = F\ (\mathrm{Re}, \mathrm{Pr}) \tag{4.4}$$

where the Nusselt, Reynolds and Prandtl numbers are defined as

$$\mathrm{Nu} = \frac{\alpha d}{k_f} \qquad \mathrm{Re} = \frac{U d \rho_f}{\mu_f} \qquad \mathrm{Pr} = \frac{C_p \mu_f}{k_f} \tag{4.5}$$

in which the subscripts f indicate that the corresponding physical quantities are taken at film temperatures θ_f, i.e., the mean of hot-wire temperature θ_w and ambient air temperature θ_g.

For an electrically heated wire in thermal equilibrium, the Nusselt number can easily be expressed in terms of the voltage e applied to the wire by writing that the heat loss by convection is balanced by the heat generated by the current in the wire:

$$\begin{aligned} \frac{e^2}{R_w} &= \pi d \ell_e\ \alpha\ (\theta_w - \theta_g) \\ &= \pi k_f\ \ell_e\ (\theta_w - \theta_g)\ \mathrm{Nu} \end{aligned} \tag{4.6}$$

or

$$\mathrm{Nu} = \frac{e^2}{\pi k_f\ \ell_e\ (\theta_w - \theta_g)\ R_w} \tag{4.7}$$

where R_w is the wire resistance at the wire temperature θ_w, and ℓ_e is the "effective" wire length of the wire, which will be discussed in detail later on.

Equation 4.4 may then be written

$$\frac{e^2}{\pi k_f \ell_e (\theta_w - \theta_g) R_w} = F\left(\frac{U d \rho_f}{\mu_f} , Pr \right) \tag{4.8}$$

If all quantities except e and U in this relation are either fixed or determined independently and if the function F is known, then the voltage e across the heated wire is only a function of the oncoming fluid velocity U. This is the basic principle of hot-wire anemometry.

If the empirical relation (Kramer, 15)

$$Nu = 0.42\, Pr^{0.2} + 0.57\, Pr^{0.33}\, Re^m \tag{4.9}$$

is used, where the Prandtl number is nearly a constant for air, and where $m \simeq 0.5$ for $10^{-2} < Re < 10^4$, Eq. 4.8 may be written as

$$\frac{e^2}{R_w (R_w - R_g)} = \frac{\pi k_f \ell_e}{\beta R_o} 0.42\, (Pr)^{0.20} + 0.57\, (Pr)^{0.33} \left(\frac{U d \rho_f}{\mu_f} \right)^{0.50} \tag{4.10}$$

since

$$\theta_w - \theta_g = \frac{R_w - R_g}{\beta R_o} \tag{4.11}$$

from the temperature-resistance formula.

In practice, Eq. 4.10 is used in the following form:

$$\frac{e^2}{R_w (R_w - R_g)} = A + B\, U^m , \tag{4.12}$$

where

$$A = 0.42 \frac{\pi k_f \ell_e}{\beta R_o} (Pr)^{0.20} \qquad (4.13)$$

$$B = 0.57 \frac{\pi k_f \ell_e}{\beta R_o} (Pr)^{0.20} (\frac{d\rho_f}{\mu_f})^{0.50} \qquad (4.14)$$

are, in general, determined experimentally by direct calibration of the hot wire.

Hilpert (9) first noticed that the correlation of experimental data could be appreciably improved if the dimensionless ratio θ_w/θ_g , which is a measure of the temperature loading of the wire, was introduced in the function F of Eq. 4.4. Hilpert arrived at the empirical relationship

$$Nu = 0.891 \left(Re (\frac{\theta_w}{\theta_g})^{\frac{1}{4}} \right)^{0.330} \qquad (4.15)$$

for $1 < Re < 4$.

The hot wire was reinvestigated by Collis and Williams (5) who took an extensive series of measurements extending from very low to fairly high Reynolds numbers with various wires. They found that their results, as well as those of other experimenters, were well correlated by the following relation

$$Nu (\frac{\theta_f}{\theta_g})^{-0.17} = 0.24 + 0.56 Re^{0.45} \qquad (4.16)$$

over a rather wide range of Reynolds numbers: $0.02 < Re < 40$.

In general the constants A and B of Eq. 4.12 or these in Eq. 4.16, with the exception of the exponents which are assumed independent of the characteristics of the wires, are determined experimentally for each particular wire by direct calibration against a primary velocity standard. Such a calibration may in general be performed very quickly by using a pitot tube, for instance, at velocities above 3 ft/sec, which is the case for the great majority of experiments.

In our case, however, the temperature as well as the velocity was varying. A wire should thus have been calibrated at various temperatures covering the entire range of utilization. This would, of course, have required a calibration facility in which the temperature could be controlled. In addition, the pitot tube could not be used as reference in our case since the velocities were below 1 ft/sec. It seemed thus desirable to avoid direct calibrations by using an empirical relationship between Nusselt and Reynolds numbers.

Considering the care with which Collis and Williams took their measurements, their results are undoubtedly trustworthy. In addition, the range of Reynolds numbers covered by them encompasses that corresponding to the velocities encountered in the mountain lee-wave study, since for a standard wire 0.2 mil in diameter, a velocity of 1 ft/sec corresponds to a Reynolds number of about 0.15. It appeared, then, that this result of Collis and

Williams was all that was needed for our velocity measurements, since it does well account for the temperature dependence.

The procedure seemed, then, straightforward: measure the wire length ℓ , diameter d , resistance R_w , and voltage e , and the gas temperature θ_g at the wire location. With this information, all other physical quantities ρ_f , μ_f , k_f could be read from tables; then Nu could be calculated, from which Re could be found by use of Eq. 4.16 which finally would yield the value of the velocity.

But before using this method, it seemed desirable to check whether the Nusselt and Reynolds numbers independently determined by us would satisfy Eq. 4.16 of Collis and Williams. Unfortunately, our points Nu vs Re would not fall on their curve of Eq. 4.16 but would be off by as much as 40%. The reasons for these discrepancies are analyzed below.

4.4.1.2 On the Difficulty of Determining Re and Nu Accurately.

The Reynolds number $Re = Ud\rho_f/\mu_f$ involves the diameter d of the wire. This diameter is generally less than 1/1000 in. Special methods are therefore required to determine d accurately. Collis and Williams used electromicrographs for this purpose. For our calculations, we only had the nominal diameter at our disposal which is only an indication of an average. The Reynolds number as calculated by us is thus affected by the same uncertainty, which accounts for one part of the discrepancies noted above.

Another source of inaccuracy is the wire length which appears in the Nusselt number of Eq. 4.7. The length used in this equation is not the actual length of the wire but the so called "effective" length which takes into account the cooling of the wire supports.

Indeed, the sensing wire is not only loosing heat by convection to the air but also by conduction to the wire supports. Because of this latter heat loss the temperature of the wire is not uniform but is minimum at both ends where the wire is soldered to the supports and maximum at the center. Since the convection heat transfer is proportional to $(\theta_w - \theta_g)$, it is less per unit length toward the ends than at the middle of the wire. The region of the wire cooled by the supports has been called the cold length. It was introduced by Betchov (2) and given by Hinze (10) as

$$\ell_c = \frac{d}{2}\left(\frac{\pi k_w}{\beta R_o \; (A + B\; U^m - I^2)} \right)^{\frac{1}{2}} \tag{4.17}$$

where k_w is the heat conductivity of the wire material, R_o the wire resistance per unit length at the reference temperature, and where the convective heat loss per unit wire length is taken as

$$\beta R_o \ (\theta_w - \theta_g) \quad (A + BU^m) \quad .$$

If for the whole wire relation (4.12) holds, then the above relation becomes

$$\ell_c = \frac{d}{2} \left(\frac{\pi k_w}{\beta R_o I^2} \quad \left(\frac{R_w}{R_g} - 1 \right) \right)^{\frac{1}{2}}$$

For the tungsten wires used

d	=	0.0002 in.	k_w	=	75 BTU/hr ft ^oF
I	=	50 mA (typically)	β	=	$2.89 \times 10^{-3}/^oF$
R_o	=	2.5 Ω	$\frac{R_w}{R_g}$	=	1.6 (overheating factor)

we find that

$$\ell_c \simeq 0.009 \text{ in.}$$

Since for the hot-wire probe used $\ell \simeq 0.05$ in.

$$\frac{\ell}{2\ell_c} \simeq 2.8 \quad .$$

According to Hinze (10) the temperature non-uniformity along the wire may be shown to be

$$\frac{(\theta_w)_{max} - \theta_g}{(\theta_w)_{av} - \theta_g} = \frac{\xi \cosh \xi - \xi}{\xi \cosh \xi - \sinh \xi}$$

$$\text{where} \quad \xi = \frac{\ell}{2\ell_c} \quad .$$

This yields in our case

$$\frac{(\theta_w)_{max} - \theta_g}{(\theta_w)_{av} - \theta_g} \simeq 1.36 \quad .$$

It is clear that the closer this ratio is to one, the better the temperature uniformity along the wire. This is far from being true for the wires used.

Owing to the large proportion of cold length in the wires used, the effective length to be used in the Nusselt number is difficult to determine. In order to avoid this difficulty long wires should be used, as was done by Collis and Williams. Their hot wires were about ten times longer than ours, i.e., $\ell/2\ell_c \simeq 30$ which yields a value of 1.03 for the above temperature difference ratio.

It should finally be noted that ℓ_c also depends on the gas velocity since either I or R_w depends on it according to whether a constant temperature or a constant current anemometer is used. Again, if very long wires are used, the influence of ℓ_c is small irrespective of velocity and this complication does not arise.

In order to be able to use the result of Collis and Williams as given in Eq. 4.16, one should therefore measure the wire diameter very accurately and use very long wires. But we did not have an electron microscope available neither did we have special probes to mount long wires.

Moreover, hot wires are very delicate sensors which not unfrequently are broken or burned, and the longer the wire the more fragile it is. For practical reasons, therefore, it was difficult to meet the requirements of Collis and Williams. Now in ordinary hot-wire anemometry, i.e., in a uniform temperature field, one never tries to match any general Nu vs Re curve, but one calibrates each wire individually which eliminates ipso facto all difficulties connected with wire length and diameter, as already mentioned above.

The question which arose then was whether a temperature compensation could be found for the calibration curve of an individual wire, in which case the effect of the characteristics of this wire would already be incorporated. Our interest was thus not to correlate the calibration of one hot wire to another, but rather to correlate the calibration curves at various temperatures for one and the same wire. What is sought, therefore, is a simple and practical temperature compensation for the hot-wire anemometer at low velocities since the general heat transfer data from heated wires could not be used.

4.4.2 A Simple Temperature Compensation for the Constant Temperature Hot-Wire Anemometer at Low Velocities.

Starting from the basic relation of Nu with respect to Re and θ_f/θ_g , the parameter associated with the effect due to temperature loading of wire

$$Nu = F_1 \left(Re, \frac{\theta_f}{\theta_g}\right) , \qquad (4.18)$$

we have

$$\frac{e^2}{\pi k_f \ \ell_e (\theta_w - \theta_g) \ R_w} = F_1 \left(\frac{U d \rho_f}{\mu_f} , \frac{\theta_f}{\theta_g} \right) \qquad (4.19)$$

by substituting Eq. 4.7 into Eq. 4.18. For a constant temperature hot-wire anemometer, whose feed back system maintains the wire resistance R_w constant irrespective of the heat convection losses due to the flow, the voltage e across the sensing hot wire is related to the bridge voltage output E, which is the quantity actually measured, by

$$e = \frac{E\ R_w}{C + R_c + R_w} \quad , \tag{4.20}$$

where C is the bridge factor of the anemometer and R_c is the cable resistance of the hot-wire probe. Hence Eq. 4.19 becomes

$$\frac{E^2\ R_w}{(C + R_c + R_w)^2\ \pi k_f\ \ell_e\ (\theta_w - \theta_g)}$$

$$= F_1\left(\frac{Ud\rho_f}{\mu_f}, \frac{\theta_f}{\theta_g}\right) \quad . \tag{4.21}$$

Now if a given wire, which implies given d and ℓ_e, is calibrated directly in the same fluid as the one in which it will be used, and if in addition the wire temperature θ_w is fixed (which is easily done with a constant temperature hot-wire anemometer by setting the value of R_w), then only E, θ_g and U in Eq. 4.21 remains variable,

$$E = E\ (U, \theta_g) \tag{4.22}$$

because all the other quantities are either fixed or dependent on θ_g and U.

It is now sought whether this relationship may be brought into the form

$$E\ (U,\ \theta_g) \times f\ (\theta_g) = F_2\ (U) \quad , \tag{4.23}$$

also a form where the dependence of E on θ_g and U are entirely separated. In the absence of a complete analytical theory of heat transfer from circular cylinders, the veracity of this postulated relationship can only be established experimentally.

From Eq. 4.21, $f\ (\theta_g)$ must be of the form

$$f\ (\theta_g) = \frac{1}{(\theta_w - \theta_g)^{\frac{1}{2}}}\ f_1\ (\theta_g) \quad , \tag{4.24}$$

and Collis and Williams' results indicate that $f_1\ (\theta_g)$, the remainder of the temperature dependence, may be put into a simple form $(\theta_f/\theta_g)^n$, thus

$$f\ (\theta_g) = \frac{1}{(\theta_w - \theta_g)^{\frac{1}{2}}} \left(\frac{\theta_f}{\theta_g} \right)^n \quad . \tag{4.25}$$

Now if Eqs. 4.23 and 4.25 are true, then once we know a calibration curve $E(U,\theta_g)$ vs U for a certain θ_g, we can plot the temperature compensated curve $E(U,\theta_{g_i}) \times f(\theta_{g_i})$ vs U, i.e., the function $F_2\ (U)$ which is the same for all θ_g's. This curve can subsequently be used to infer the velocity at a point from the measurement of E and θ_g.

The exponent n may be determined once a set of calibration curves E vs U for various θ_g's are known, since it must be such that all curves $E\ (U,\theta_{g_i}) \times f(\theta_{g_i})$ vs U for the various θ_{g_i}'s collapse on a single line. This may be repeated for several wires to obtain a better definition for n, and to see whether n varies from one wire to another. It should be remarked that n is not necessarily a constant but may depend on θ_g. If n is a constant or even a function of θ_g but not of the wire resistance R_w, then this value of n and the corresponding values of $f\ (\theta_g)$ may subsequently be used with any wire to predict velocities from the measurement of E and θ_g.

4.4.3 Apparatus and Procedure.

The first step in the determination of n is the measurement of E vs U curves at various θ_g's for several wires. A micro wind tunnel specially designed to produce very low velocities was available as a calibration wind tunnel at that time, but it had no provisions for the control of the air temperature. Since the large Army Meteorological Wind Tunnel at the Fluid Dynamics and Diffusion Laboratory is equipped with such temperature control, it was used as a temperature chamber and the micro tunnel was set inside. The instrumentation and experimental procedure are described in the following sections.

4.4.3.1 <u>Instrumentation</u>.

i) Hot-Wire Anemometer and Digital Voltmeter

In this investigation, a Disa (model 55 A01) constant temperature anemometer (see Fig. 12) and a Disa probe (model 55 A22) were used. The sensing elements were pure tungsten wires 0.0002 in. in diameter and approximately 0.06 in. long soldered to the probe.

The wire temperature was calculated from the temperature-resistance equation

$$R_w = R_o \left(1 + \beta \, (\theta_w - 32) \right) \tag{4.26}$$

in which R_o is the wire resistance at 32^oF, and β is the temperature resistivity coefficient, equal to $2.89 \times 10^{-3} \; (^oF)^{-1}$ for tungsten.

For this anemometer, the voltage e across the sensing hot wire is related to the bridge voltage output E by

$$e = \frac{1.04 \; (E \;\; R_w)}{100 + R_w + R_c} \quad . \tag{4.27}$$

In order to measure the bridge voltage output from the anemometer accurately, a 4-digit digital voltmeter (Hewlett-Packard model 3440A) was used. Hence, the anemometer output which in general is of the order of several volts could be read to the nearest millivolt.

ii) Thermocouple

A copper-constantan thermocouple was used to measure the mean air temperature. The electro-motive force of the thermocouple was measured with a Weston (model 1477) vacuum tube voltmeter as shown in Fig. 12, instead of the usual potentiometer. The lowest full scale of this meter is 1 millivolt and the rated accuracy is 1/2% of the full scale reading.

iii) Micro Wind Tunnel

This small, portable wind tunnel was designed for the specific purpose of investigating and calibrating instruments at very low velocities, say below 2 ft/sec. The tunnel consists of a circular test section 5½ in. in diameter following a 1 in. diameter control section. The velocity in the control section, therefore, is approximately 30 times larger than in the test section; it is measured with a pitot tube permanently mounted in it. The dynamic head from this pitot tube was measured with an "Equibar" pressure transducer manufactured by Transonics Inc. The velocity in the tunnel is controlled by changing the voltage applied to the fan motor.

In order to have a uniform velocity profile at the test section, four layers of uniform screen of opening 16% are placed upstream of the test section. The region of uniform velocity lies in the center zone with 3½ in. in diameter approximately. Using the continuity equation, and taking into account the velocity distribution, the relation

$$U_2 = f(U_1) \qquad (4.28)$$

was determined, where U_1 and U_2 are the velocities at the centers of the control and test sections, respectively. This calibration curve of the micro wind tunnel U_2 vs U_1 is shown in Fig. 13. With this relation, U_2 may be inferred from the pitot tube measurement. A detailed description of this low velocity tunnel may be found in "Ultra Low Speed Anemometer" by R. Kung and G. Binder (16).

iv) Army Micro-Meteorological Wind Tunnel and Uniform Temperature Chamber

As mentioned in the beginning of this section (4.4.3), the Micro-Meteorological Wind Tunnel - to which we shall refer as large wind tunnel for brevity - can be used as a temperature chamber. Since the air in the large wind tunnel is heated or cooled by a set of coils located in the return section through which hot or cold brine may be circulated, a steady uniform temperature throughout the tunnel can only be obtained when the tunnel is running. There is, then, a balance between the heat input from the coils and the conduction losses through the tunnel walls. And once the tunnel is stopped, the temperature in the test section decreases in case the tunnel is heated, and vise versa if the tunnel is cooled.

In order to improve the constancy of θ_g during any particular calibration run, the micro tunnel was set inside a sheet metal box which was put into the large wind tunnel. The temperature in the chamber never varied more than $1^{o}F$ between the beginning and the end of any calibration run.

4.4.3.2 Calibration Procedure.

The experimental setup for the calibration of hot wires at different ambient air temperatures consisted in setting the micro tunnel inside the uniform temperature chamber which was placed in the large wind tunnel. A thermocouple was installed in the box to indicate the ambient air temperature, and a hot wire heated at θ_w was installed at the center of the test section of the micro tunnel. All the electronic instruments were operated outside the large wind tunnel.

The lid of the chamber was kept open while the large tunnel was running and while its temperature was being brought to the desired value. When this temperature was approximately reached, the large tunnel was stopped, the lid of the chamber closed and the micro tunnel started. After temperature in the box became approximately steady and uniform owing to the mixing of the air produced by the micro tunnel, the calibration run was taken as quickly as possible.

For about ten different velocities ranging from 0.2 to 1.7 ft/sec, the hot-wire anemometer output and the voltage of the pressure transducer connected to the pitot tube of the micro-tunnel control section were read and recorded. The emf of the thermocouple was recorded at the beginning and the end of every run. Such a run took on the average of about three minutes.

4.4.4 Results.

4.4.4.1 Uncompensated Calibration Curves.

According to the calibration procedure described in section 4.4.3.2, four wires were calibrated at various air temperatures. The temperature was obtained from the thermocouple emf and the velocity from the dynamic head of the pitot tube of the control section of the micro tunnel, together with the calibration curve of this tunnel and the knowledge of the temperature. These data are shown in Figs. 14-17. The "hot" resistances of the wires R_w were respectively 4.7, 4.64, 4.39 and 4.37 ohms. The hot-wire temperature θ_w was fixed at 300°F, and the ambient temperature θ_g ranged from 49.4°F to 112°F.

Figures 14-17 display the large influence of θ_g on the anemometer output in the velocity range considered, i.e., from 0 to 1.6 ft/sec. For example, consider the two curves E vs U for θ_g equal to 86.7°F and 76°F in Fig. 17. For a reading of 5.400V, the corresponding velocities are respectively 0.58 and 0.95 ft/sec, i.e., a difference of almost 100% in velocity corresponds to temperature difference of only 10°F. It is quite clear that for lower velocities the relative error induced by neglecting temperature effects is even larger.

4.4.4.2 Evaluation of Exponent n in $(\frac{\theta_f}{\theta_g})^n$

To begin with, the curves $E/(\theta_w - \theta_g)^{\frac{1}{2}}$ vs U were plotted as shown in Figs. 18-21. Taking the same example as above, we see that the error in predicting the velocity is reduced to about 20% for a 10°F change in θ_g. This first step does, hence, partly compensate the temperature effects on the hot wire.

Next, we notice that the outputs for the same velocity but for two different air temperatures θ_{g_1} and θ_{g_2} for a given wire are related by

$$E(U,\theta_{g_1}) \times f(\theta_{g_1}) = E(U,\theta_{g_2}) \times f(\theta_{g_2}) = F_2(U); \quad (4.29)$$

hence, from the presumed expression of $f(\theta_g)$ given in Eq. 4.25

$$n = \frac{\log \dfrac{E(U,\theta_{g_1})}{(\theta_w - \theta_{g_1})^{\frac{1}{2}}} - \log \dfrac{E(U,\theta_{g_2})}{(\theta_w - \theta_{g_2})^{\frac{1}{2}}}}{\log \dfrac{\theta_{f_2}}{\theta_{g_2}} - \log \dfrac{\theta_{f_1}}{\theta_{g_2}}} . \quad (4.30)$$

The evaluation of n given in Eq. 4.30 can only be used when n is independent of θ_g and is a universal constant, and also when no errors exist due to experimental operations or instruments for any calibration run. But actually errors are unavoidable. If only two sets of data taken at any two θ_g are considered to evaluate n, the inaccuracy on any particular temperature leads to an exaggerated dispersion. Therefore the n values calculated by Eq. 4.30 can only be used as a first approximation. The exact values of n are chosen by comparing all data at different θ_g in the whole range of velocity for a given wire such as to obtain least dispersion of all points $E \times f(\theta_g)$ vs U from a single curve.

The values of n thus obtained are plotted on Fig. 22, as a function of θ_g. Above 70°F, n remains equal to 0.059 and below this temperature it slightly decreases. Figure 23 displays the temperature function $f(\theta_g)$ for the wire temperature $\theta_w = 300^{\circ}$F. It should be stressed that this function is the same for all four wires tested, and one may therefore assume that it will be the same for any other wire whose hot resistance R_w lies between 4 and 5 Ω.

This latter restriction should not be overlooked. Indeed two wires with resistances of 7.08 and 9.01 Ω respectively were tested in the same way. The values of n obtained were of the order of 0.07, markedly higher than 0.059. On the other hand, this restriction is not a serious one if standard Disa hot-wire probe and the same gage wire are used. The hot resistances of such sensing wires, with an overheating factor of 1.6, usually fall into the 4 to 5 Ω range.

Figures 24-27 are the plots of $E \times f(\theta_g)$ for the four wires with the values of n shown in Fig. 22. It is seen on these figures that all calibration curves collapse onto one line. The dispersion of the data points about the mean curve is not large. These results are, therefore, quite satisfactory.

Finally, it should be remarked that the curves $E \times f(\theta_g)$ are straight lines over most of the velocity range (0, 1.6 ft/sec). Therefore,

$$E\ (U,\theta_g)\ \times\ f\ (\theta_g) = A + BU \qquad (4.31)$$

for 0.2 ft/sec < U < 1.6 ft/sec. The constants A and B are determined from the calibration of each individual wire.

4.4.4.3 <u>Use of the Results</u>.

Let us illustrate how these results may be used for velocity measurements in a temperature field by outlining the various steps of the procedure to be followed.

Suppose we have a tungsten wire such that its resistance on the probe at 300°F is comprised between 4 and 5 ohms. Then successively:

i) Calibrate the hot wire in the micro tunnel at room temperature, say 70°F.

ii) Plot $E(U, 70^{\circ}F) \times f(70^{\circ}F)$ vs U, where the value of $f(70^{\circ}F)$ is read from Fig. 23.

The hot wire is now ready for use. It should now be set in the flow to be measured very close to a thermocouple or a resistance thermometer.

iii) Read the hot-wire anemometer output E_1 and the output of the thermocouple which yields θ_g, say 95°F.

iv) Obtain $f(95^{\circ}F)$ from Fig. 23 and compute $E_1 \times f(95^{\circ}F)$.

v) Read the velocity U_1 from the plot of step 2.

4.4.4.4 Accuracy of This Temperature Compensation.

Finally, let us evaluate the maximum error effecting a certain velocity measurement by use of this temperature compensation. If we assume that the data points represent true values, then the dispersion of the points from the $E \times f(\theta_g)$ vs U curve is a measure of the accuracy of this method of temperature compensation.

For example, if the curve $E \times f(\theta_g) = 0.365 + 0.0166\ U$ in Fig. 27 is used to predict velocities, the maximum error is 6% and for the curve $E \times f(\theta_g) = 0.383 + 0.0135\ U$ in Fig. 25, the maximum error is less than 4%.

As mentioned previously, the relative error in higher velocities is less than that for lower ones. In this case, one may then take $n = 0.059$. For example, given $R_w = 4.64$ ohms, $\theta_w = 300^{\circ}F$, $\theta_g = 55.6^{\circ}F$, $E = 5.588$ volts, $\theta_f/\theta_g = 3.14$, and if $n = 0.059$ instead of 0.056 is used, the resulting error is only 6.6%. Of course this error is the maximum one since the extreme value was used in this example.

From the above remarks, one may conclude that on the average the velocities thus determined are accurate to about 3%, the accuracy being better for higher velocities but less for lower velocities.

4.4.4.5 Check of Results

The relationship shown in Eq. 4.23 or 4.31 was obtained by using the Disa Constant Temperature Anemometer. In order to make sure that this relation is valid for any constant temperature anemometer, the compensation was applied to a wire used with a Heat Flux System (manufactured by Thermo-System Inc.). The correlation obtained for this data shown on Fig. 28 showed that the compensation is applicable to any constant temperature hot-wire anemometer. Note that the output from the Heat Flux System is about half of Disa Constant Temperature Anemometer.

CHAPTER V

RESULTS AND ANALYSIS

In this chapter the experimental observations of mountain lee-waves simulated in a wind tunnel by thermally stratified flow over model mountains are described and analysed.

Two models of the same height (4 in.) but of different widths were used. Their profiles are shown in Figs. 29 and 30. The wider one shall be referred to as "model I" and the narrower one as "model II." The models were always placed 30 ft downstream of the leading edge of the cold plate which creates the thermal boundary layer.

It would be desirable to change velocity and stability separately in order to observe their individual effects on the flow pattern. This was not possible with the wind tunnel available for these experiments. Indeed since the density stratification is provided by the temperature variations across the thermal boundary layer created freely by the flow of hot air over a cold plate and since effects due to free convection (density currents) partly determined the flow, velocity and temperature - or density - distributions were intimately coupled and could thus not be varied separately.

The wind tunnel was run in the same conditions for several hours after it was stabilized. The data consisted of two kinds: photographs of the flow pattern visualized by smoke and combined hot-wire anemometer and temperature profiles. Such profiles were taken at one location far upstream of the model and at several locations on the lee side of it.

5.1 Computation of Froude Number and Reynolds Number.

5.1.1 Froude Number.

As mentioned earlier in section 3.2, the Froude Number is defined by

$$Fr = \frac{V}{H\left(g\sigma\right)^{\frac{1}{2}}} = \frac{V}{H\left(g\frac{1}{\theta}\frac{d\theta}{dz}\right)^{\frac{1}{2}}} \tag{5.1}$$

where the stability is taken far upstream of the barrier where the flow is undisturbed.

Since the velocity upstream of the model was nearly uniform in a layer extending from the tunnel floor to elevations of four to five times the model height, the characteristic velocity was taken as the average velocity in this layer.

The stability, however, varied continuously from maximum at ground level to zero in the free stream so that the choice of a characteristic value is not evident a priori. One could indeed choose for σ the value of the arithmetical mean, the value at the midpoint in the thermal boundary layer, the value at the elevation of the mountain top etc.

After close scrutiny of the temperature profiles, it appeared that all profiles could fairly well be approximated by two straight lines. The thermal boundary layer could thus be divided into two sub-layers, of which the lower one has the larger stability. Figure 31 is a typical example of such a temperature profile. This layer was found to have approximately the same thickness of 0.6 ft for all flows considered. Since this layer seemed mainly responsible for the generation of lee-waves, it was then natural to choose its constant stability and its thickness as characteristic values for the Froude number.

This method of calculating the Froude number is similar to that used by Long (19). The Froude numbers thus calculated of the flows analysed here have values between 0.2 and 0.3, also values comparable to those of Long's experiments which varied from 0.103 to 0.283.

The authors of the World Meteorological Organization report (see Ref. 26) remark on p. 47 that: "In airstreams containing lee waves, there is evidence that the air has greater static stability than the average at low levels surmounted by air of lesser stability above.... It seems an essential requirement, at least for strong waves, that there should be marked stability at levels where the air is disturbed by the mountain."

It is fortunate that the conditions in the wind tunnel correspond precisely to this situation, i.e., a lower layer with strong static stability with a thickness one and a half times the model height surmounted by a layer in which the stability is less. Thus, although the stability distributions in these simulation experiments were all of the same type, this type is precisely the one which produces strong lee-waves.

5.1.2 Reynolds Number.

For reference we shall indicate the value of the Reynolds number:

$$Re = \frac{VH}{\nu} \quad .$$

Taking for the mean upstream velocity, i.e., about 0.25 ft/sec for H - the characteristic length - the height of stratified layer used in the Froude number, also 0.6 ft, and the value of ν for a temperature of about 75°F, one obtains

$$Re \sim 10^3 \quad .$$

This value of the Reynolds number is small so that viscous effects may not be entirely negligible throughout the flow.

5.2 Wave Pattern.

5.2.1 Flow Visualization Data.

The existence of lee-waves in the wind tunnel simulation experiments is beyond doubt. This striking effect of a barrier on a density stratified current is shown on the photographs of Figs. 32-39 on which the flow pattern has been visualized by smoke.

The smoke was being introduced several model lengths upstream of the barrier so that it moved in horizontal streams as it reached the "mountain." Owing to the very low entrainment velocity, it is not possible to produce sharply defined smoke lines as can be done in smoke tunnels, although it was introduced into the stream by a rake. The scale on these photographs is given by a one foot long strip of sheet metal clearly visible on the tunnel floor just downstream of the model.

On Figs. 40 and 41, the first wave lengths and wave amplitudes of several streamlines intersecting the vertical passing through the model crest at heights of 3/2 h, 2h, 5/2 h etc. (h: model height) are plotted vs Froude number. The wave lengths λ are measured from the point where the streamline crosses the vertical of the mountain crest to the point where it has completed a cycle. The amplitudes A are defined as half the difference in elevation between the first wave trough and the following wave crest.

The dominant feature of Fig. 40 is the linear increase of wave length with Froude number for waves at a given height. This result is in agreement with the linearized lee-wave theory. It is seen that one roughly has

$$\frac{\lambda}{2\pi H} = 2.5\,Fr + \text{constant for } 0.2 < Fr < 0.3 \,, \tag{5.2}$$

where H is the length used in the definition of Froude number. The constant depends upon the height but is small. The critical wave length λ_s which appears in the one layer linear theory is defined as

$$\lambda_s = \frac{2\pi}{j_s} = 2\pi \frac{V}{(g\sigma)^{\frac{1}{2}}} \quad ;$$

may be expressed as

$$\lambda_s = 2\pi \text{ H Fr} \quad .$$

By comparing these relations one sees that as a rough approximation

$$\lambda \approx 2.5 \lambda_s \quad .$$

It should be noticed that the wave lengths are nearly independent of the model width, since both models produce waves of the same length for a given Froude number although their half width are in the ratio of one to two. This is in contradiction with the results of Queney's (23, 24) which predicts wave lengths strongly dependent on the horizontal scale of the mountain.

In the laboratory simulation the lower streamline leaves the larger model somewhere half the way down the lee slope, whereas on the small model it remains attached almost to the very bottom of the slope. This separation on the wider model may be due to viscous effects whose braking action is more important over this model because of the greater length of contact.

In order to decide whether this separation occurs because of the independence of the wave length from the horizontal scale of the mountain or whether it is a simple viscous boundary layer separation, one should with the same model perform the experiment with the same Froude number but with larger velocity and larger static stability. This is unfortunately not possible with the present experimental setup which cannot produce stabilities larger than the ones reported here.

Finally, Fig. 40 seems to indicate that the wave lengths pass through a maximum at the height 2 h. This result is, of course, the result of the stability distribution proper to these experiments and is, hence, not of a general nature.

The plot of Fig. 41 shows that the wave amplitudes also increase strongly with Froude number but they decrease with height, a result of the decreasing static stability. Since the amplitudes are affected in a very complex manner by the Froude number in all analytical models, comparison between theory and experiment is rather difficult.

The smoke visualization also shows that the first wave crests lie about 0.8 to 0.85 downstream of the mountain top, which compares quite well with the 3/4 λ displacement predicted by theory. On the other hand, one also observes a certain upstream tilt of the first wave troughs. a result in agreement with some analytical predictions.

5.2.2 Constant Temperature Lines.

If diffusion effects are slow enough, as discussed in section 4.3, constant temperature lines coincide with streamlines. The measurement of temperature profiles at various locations combined with simple interpolations allowed to determine points with the same temperature. The lines joining those points show as the visualizations of the lee-waves in striking fashion.

Figure 42 is an example of the measured temperature profiles for $U = 0.3$ ft/sec , $\sigma = 0.121\ ft^{-1}$. Figures 43 - 48 show the streamlines thus determined for various flows. The wave pattern of these figures compares well with those of the smoke photographs.

These figures clearly show the second wave which cannot be seen on the photographs because the smoke is weakened out by turbulence at such a distance downstream. The second wave is seen to be damped compared to the first one.

It should be mentioned that the streamlines obtained above a height of 1 ft, i.e., at the edge of the temperature boundary layer, are subject to large degrees of error because of the smallness of the temperature gradient in this region. A small error in temperature reading results, there, in a large vertical displacement of a streamline.

5.3 Velocity Distributions, Blocking.

Velocity distributions were determined at several stations by the hot-wire technique and temperature compensation method described in section 4.4. These velocity profiles are displayed in Figs. 43 to 48.

The velocity distributions far upstream of the model, i.e., eight to nine feet from the mountain crest, are fairly uniform to a height of one foot at least, i.e., across the stratified layer. In Figs. 43, 44 and 45, this region of quasi uniformity reaches two feet. In the cases of Figs. 46, 47 and 48, this layer is followed by a layer of zero or nearly zero velocity, in other words by a stagnant zone. The existence of such a stagnant zone at a certain height is difficult to explain rigorously; it may be attributed to the particular flow conditions in the wind tunnel, where let us recall, the flow is partly driven by the gravity current into the tunnel entrance. In Figs. 47 and 48, this stagnant layer is clearly followed by a shear layer.

The velocity profiles just upstream of the model show similar characteristics.

The feature of the upstream velocity profiles that must be emphasized is the complete absence of "blocking." Indeed none of these profiles show a layer adjacent to the ground with zero velocity. This is in contradiction with the theoretical predictions of Kao (14), according to which a stagnant zone whose thickness may be an important fraction of the mountain height, should extend from the barrier to large distances upstream. This absence of a stagnant zone upstream may be due to viscous entrainment. On the other hand, it is not to be excluded that such stagnation would not occur at lower Froude numbers. It should be recalled that in Debler's experiments (6) stagnation occurred at values of the Froude number appreciably lower than the theoretical $1/\pi$, although at Froude numbers of 0.2 stagnation always occurred. Here again, in order to make sure that this absence of a stagnation zone at ground level is not due to viscous entrainment, the experiments should be repeated with flows of the same Froude but higher Reynolds numbers.

Over the mountain crest, all the velocity profiles show a sharp maximum at a very small distance from the mountain top. The magnitude of this maximum velocity is about 1.5 to 1.8 times the average upstream velocity. This increase in velocity persists on the lee slope. The flow visualizations gave a very vivid impression of the air streaming down the lee slope. This feature, observed and measured in the experiment, corresponds to the "Fohnwall" or "cloud fall" often observed over mountain ranges simultaneously with lee-waves.

Queney's theory predicts strong downslope winds in agreement with the observations reported here, whereas Scorer's model, on the contrary, yields maximum wind on the up-slope (see Fig. 49).

This strong downdraft on the lee side, in the vicinity of the mountain, results in most cases of a stagnant zone of air above (Figs. 43-48). Higher up, the shear layer is clearly seen. In the present cases of a decreasing static stability, the effect of the mountain is thus only felt to elevations two to three times the mountain height.

The redistribution of velocity due to gravity on the lee slope is thus considerable; the velocity being nearly doubled right above the mountain and reduced to zero in the layer above. To illustrate this effect the velocity vectors are drawn for two cases on Fig. 50.

5.4 The Rotor.

The rotors which develop between the wave crests and the ground have attracted the attention of many investigators and they have been sketched into the flow pattern early in the short history of mountain lee-waves.

Below the first wave crest on the smoke photographs, one notices at once a zone where the smoke is absent, which corresponds to the rotor. It is clear that the fluid in this area below the lowest streamline, coming over the mountain, cannot come from upstream. In order to bring the flow in the rotor out more clearly, it was tried to introduce smoke directly into this zone (see Fig. 33). The strong turbulence which exists there, however, quickly dissipates the smoke so that the system of closed streamlines could not be directly observed.

At ground level one could unmistakably see the smoke move upstream. The hot-wire anemometer output showed that the flow in this layer was laminar.

Above this layer and below the wave crest, the mean velocity was positive again but large fluctuations were present in the hot-wire output, which points to the existence of strong turbulence in this zone. It should be added that nowhere else was the flow turbulent. It is also worth mentioning that the lowest streamline, originating from upstream and in contact with the rotor, broke into small wavelets after the rotor.

These features of the rotor zone observed in the experiments coincide exactly with the natural observations (see Ref. 26, p. 2 and 9).

The temperature profiles across the rotor also show that the temperature there is nearly uniform (see Fig. 42) evidence of the strong mixing which takes place.

CHAPTER VI

CONCLUSIONS AND SUGGESTIONS FOR FURTHER RESEARCH

6.1 Conclusions.

In this investigation it was shown that the hot-wire anemometer is suitable for measuring very low velocities, between 0.2 and 1.5 ft/sec say, in a non-uniform temperature field. A simple method for the temperature compensation of this anemometer at these velocities and for temperatures between 50 and 110°F has been developed.

The other results of this research may be summarized in stating that a class of mountain lee-waves may be simulated in a wind tunnel where the density stratification is produced by flow of hot air over a cold plate. These lee-waves have been determined by flow visualization methods and by tracing constant temperature lines.

It was found that both wave lengths and wave amplitudes increase with Froude number. The first wave crest occurs about 0.8 wave lengths down stream of the crest of the barrier. The first wave trough tilts slightly upstream.

The measurements of velocity profiles show the considerable increase in velocity on the downstream slope. The maximum velocity just above the mountain crest was found to be 1.5 to 1.8 times stronger than the average upstream velocity. No stagnation zone was observed in the vicinity of the ground upstream of the model.

The flow under the first wave crest resembles in several aspects that of the rotors observed in nature, in particular, considerable turbulence just below the wave crest and reverse flow at ground level.

6.2 Suggestions for Further Research.

This investigation showed the possibility of producing lee-waves in a wind tunnel. It showed that it would be desirable to be able to change the stratification independently from the velocity. Also, that a stronger stratification would prove useful since it would permit the velocity to be increased and thus obtain larger Reynolds numbers. On the other hand, stronger stratification would also make possible the creation of flows of lower Froude numbers with the same velocity, and thus to hopefully be able to obtain blocking effects.

In short, these remarks point to the need of a specially designed wind tunnel for the simulation of stratified flows. In such a tunnel one could then systematically investigate the influence of various parameters on lee-wave characteristics.

BIBLIOGRAPHY

BIBLIOGRAPHY

1. Abe, M., 1941. "Mountain Clouds, Their Forms and and Connected Air Current" Part II. Bull. Central Meteor. Observatory of Japan, VII, vol. 3, pp. 93-145.

2. Betchov, R., 1948. "Proc. Koninkl. Ned. Akad. Wetenschap." vol. 51, pp. 721.

3. Cermak, J. E., ed., 1966. "Simulation of Atmospheric Motion by Wind Tunnel Flows." Fluid Dynamics and Diffusion Lab., Colorado State Univ., pp. 357-384.

4. Chao, L. T. and Sandborn, V. A., 1964. "A Resistance Thermometer for Transient Temperature Measurements." Paper No. 1, Fluid Mech. Papers, Colorado State Univ.

5. Collis, D. C. and Williams, M. J., 1959. "Two-Dimensional Convection from Heated Wires at Low Reynolds Numbers." J. of Fluid Mech. vol. 6, pp. 357-384.

6. Debler, W. R., 1959. "Stratified Flow into a Line Sink." J. Eng. Mech. Div., Proc. ASCE, vol. 85, pp. 51-65.

7. Foldvik, A. and Wurtele, M. G. "The Computation of the Transient Gravity Wave." Dept. Meteor., Univ. of Calif. L.A.

8. Goldstein, S. (Editor), 1938. "Modern Developments in Fluid Dynamics." vol. II, p. 608.

9. Hilpert, R., 1933. "Wärmeabgage von Geheizten Drähten und Rohren im Luftstorm." Forsch. Ingwes., vol. 4, pp. 215-224.

10. Hinze, J. O., 1959. "Turbulence." p. 87, McGraw-Hill.

11. Holmboe, J. and Klieforth, H., 1957. "Investigations of Mountain Lee Waves and the Air Flow Over the Sierra Nevada." Dept. Meteor., Univ. of Calif. L.A.

12. Hovermale, J. B., 1965. "A Non-Linear Treatment of the Problem of Air Flow Over Mountains." Doctoral Dissertation, Dept. Meteor., Penn. State Univ.

13. Kao, T. W., 1963. "The Phenomenon of Blocking in the Stratified Flow." Doctoral Thesis, Univ. of Michigan.

14. Kao, T. W., 1965. "The Phenomenon of Blocking in Stratified Flow." J. Geoph. Res., vol. 70, No. 4, pp. 815-822.

15. Kramers, H., 1946. "Physica." vol. 12, p. 61.

16. Kung, R. and Binder, G. J., 1967. "Ultra Low Speed Anemometer." Tech. Rep. Colorado State Univ.

17. Kuettner, J., 1939. "Moazagotl und Foehwell." Beitr. Phys. Frei. Atmos. vol. 25, pp. 79-114.

18. Long, R. R., 1953. "Some Aspects of the Flow of Stratified Fluids, I. A Theoretical Investigation." Tellus, vol. 5, pp. 42-58.

19. Long, R. R., 1955. "Some Aspects of the Flow of Stratified Fluids, III. Continuous Density Gradients." Tellus, vol. 7, pp. 341-357.

20. Long, R. R., 1959. "A Laboratory Model of Air Flow Over the Sierra Nevada Mountains." The Rossby Memorial vol., pp. 372-380.

21. Lyra, G., 1943. "Theorie der Stationären Leewellen-Strömung in Freier Atmosphäre." Zeit. f. Angew. Math. Mech. vol. 23, pp. 1-28.

22. Palm, E. and Foldvik, A., 1959. "Contribution to the Theory of Two-Dimensional Mountain Waves." Geof. Publ. vol. 21, No. 6, Oslo.

23. Queney, P., 1947. "Theory of Perturbations in Stratified Currents With Application to Air Flow Over Mountain Barriers." Dept. Meteor., Univ. of Chicago, Misc. Rept. No. 23.

24. Queney, P., 1948. "The Problem of Air Flow Over Mountains: A Summary of Theoretical Studies." Bull. Am. Meteor. Soc., vol. 29, p. 16.

25. Queney, P., 1954. "The Inertial Value Problems in a Double Couette-Flow." Auto-Barotropic Flow Project, Sci. Rep. No. 1, Contract No. AF 19 (604)-728.

26. Queney, P., et al. 1959. "The Air Flow Over Mountains." The World Meteor. Org. Tech. Note No. 34.

27. Schlichting, H., 1960. "Boundary Layer Theory." 4th ed., McGraw-Hill, p. 120.

28. Scorer, R. S., 1949. "Theory of Waves in the Lee of Mountains." Quart. J. Roy. Meteor. Soc., vol. 75, pp. 41-56.

29. Suzuki, S. and Yabuki, K., 1956. "The Airflow Crossing Over the Mountain Range." Geophys. Mag., Tokyo, vol. 27, pp. 273-291.

30. Wurtele, M. G., 1953. "The Initial-Value Lee-Wave Problem for the Isothermal Atmosphere." Sci. Rept. No. 3, Sierra Wave Project, Contract No. AF 19(122)263, Air Force Cambridge Res. Center, Cambridge, Mass.

31. Wurtele, M. G., 1953. "Studies of Lee Waves in Atmospheric Models with Continuously Distributed Static Stability." Sci. Rept. No. 4, Contract No. AF 19(122)263, Air Force Cambridge Res. Center, Cambridge, Mass.

32. Yih, C. S., 1958. "On the Flow of a Stratified Fluid." Proc. 3rd U. S. Nat. Cong. Appl. Mech., pp. 857-861.

FIGURES

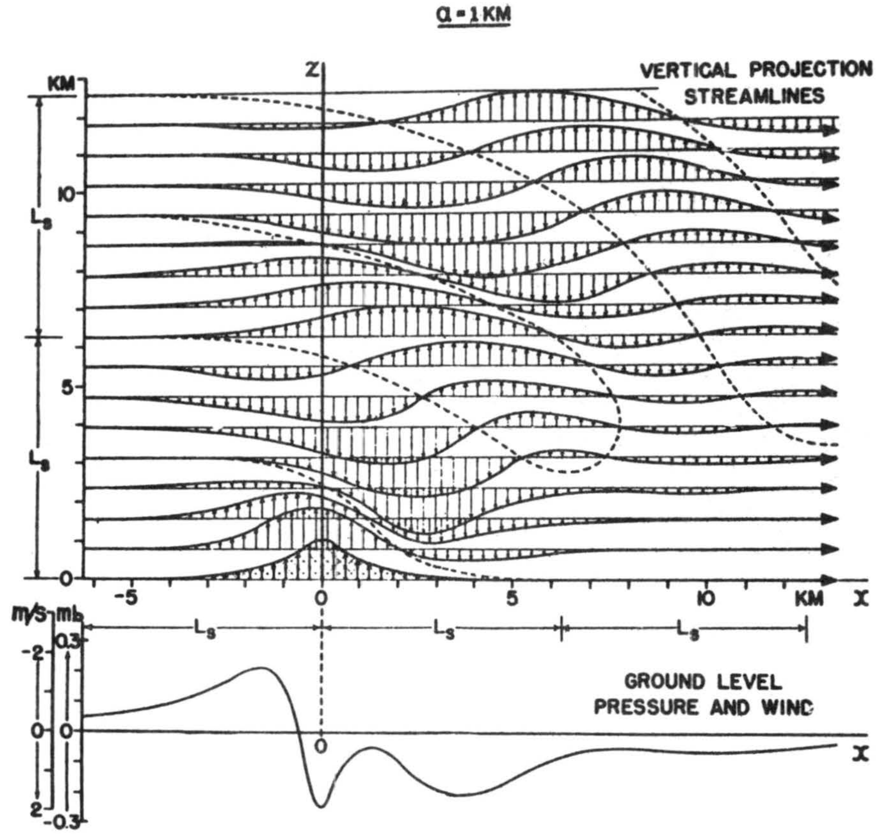

Fig. 1 Flow over a symmetric mountain profile whose width is one critical wave length $2\pi b = 6.28$ km

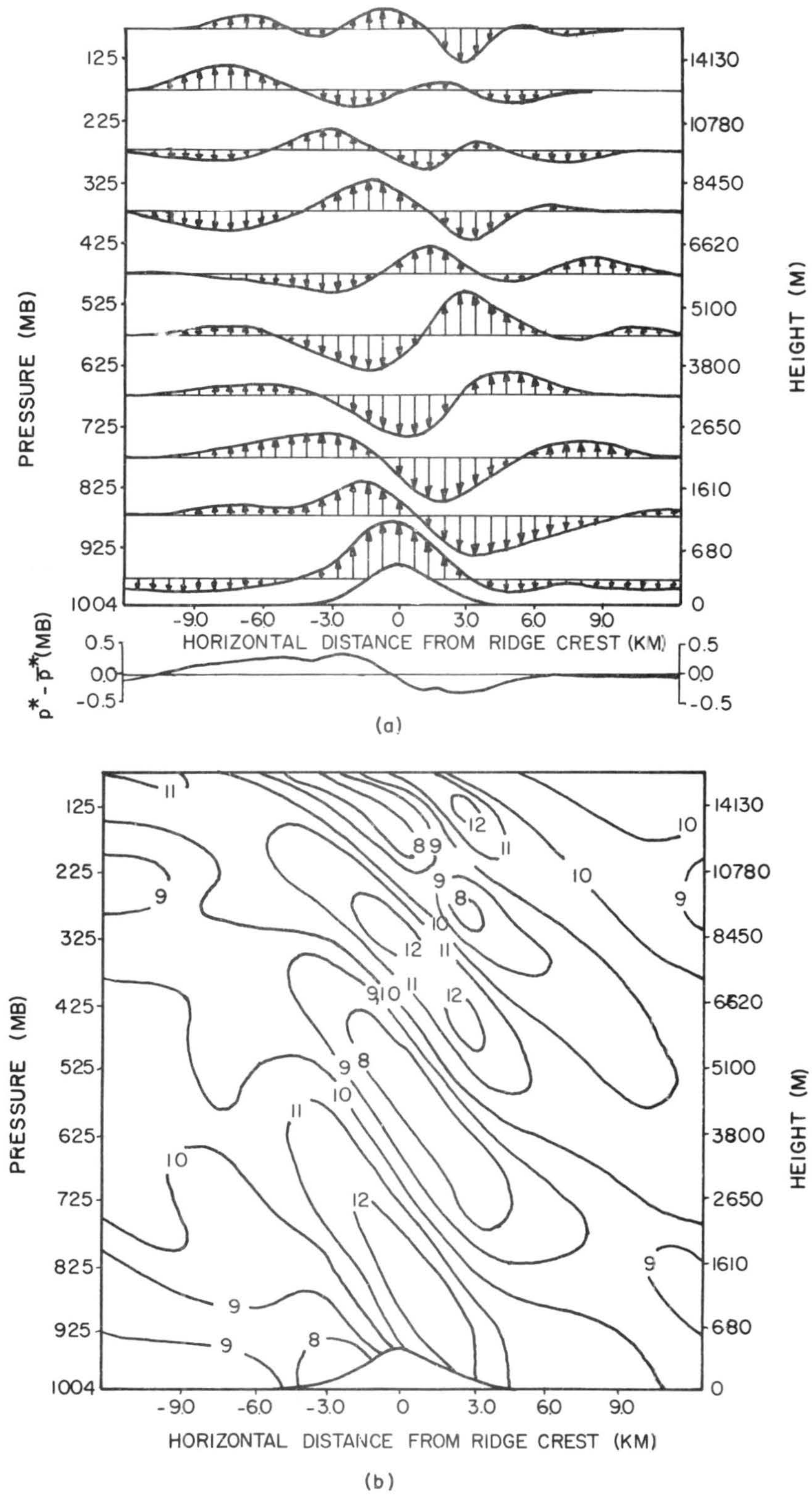

Fig. 2 Results of Hovermale's computer model
a) Displacement of potential temperature lines at 25 minutes
b) Horizontal velocities (m/sec) at 35 minutes

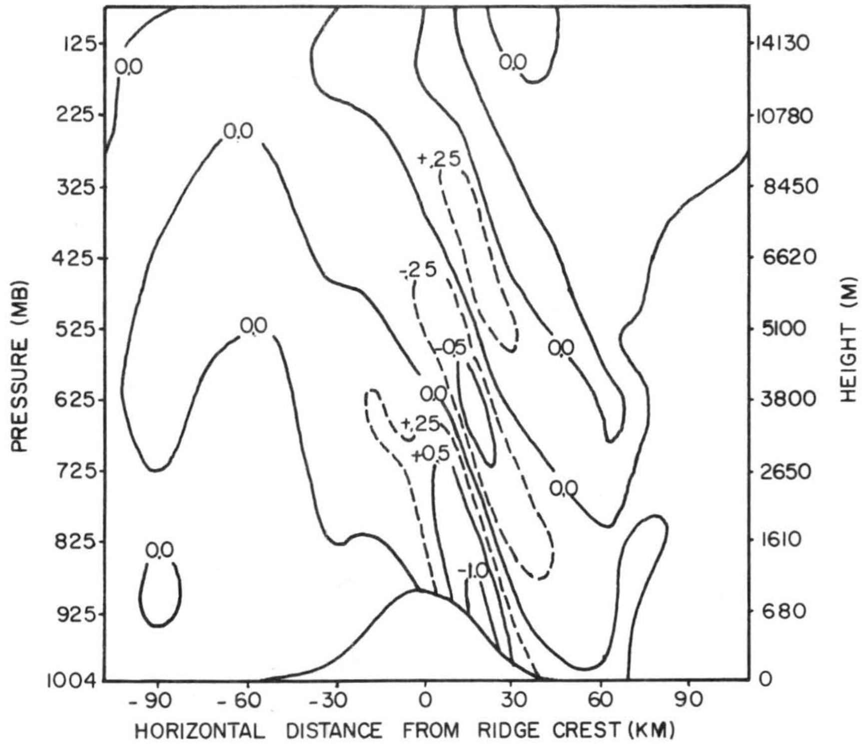

(a)

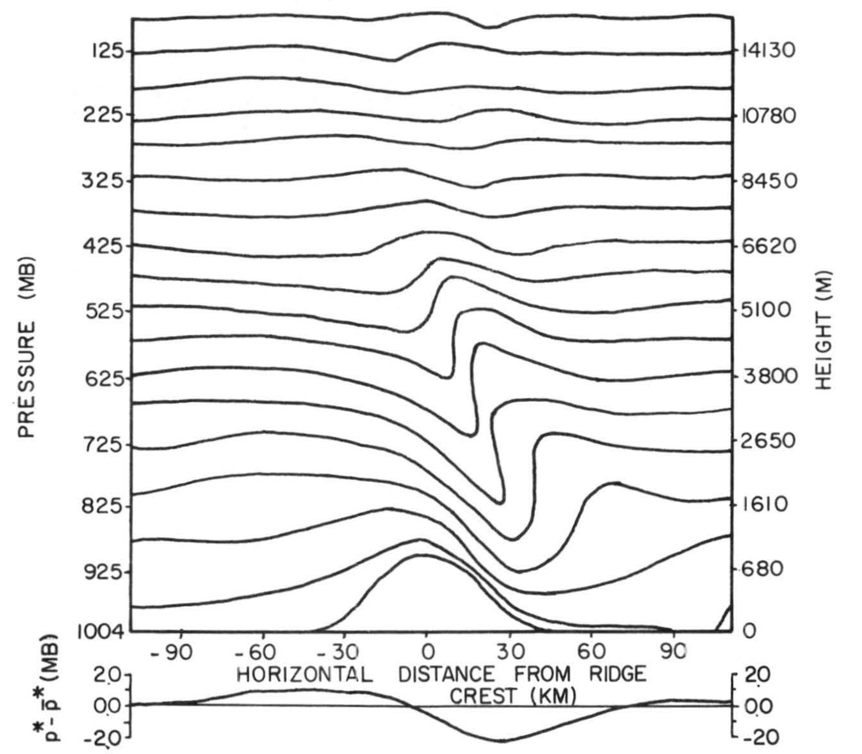

(b)

Fig. 3 Results of Hovermale's computer model
a) Vertical p-velocities (mb/sec x 10^{-1}) at 2 hrs.
b) Displacement of potential temperature lines at 3 hrs.

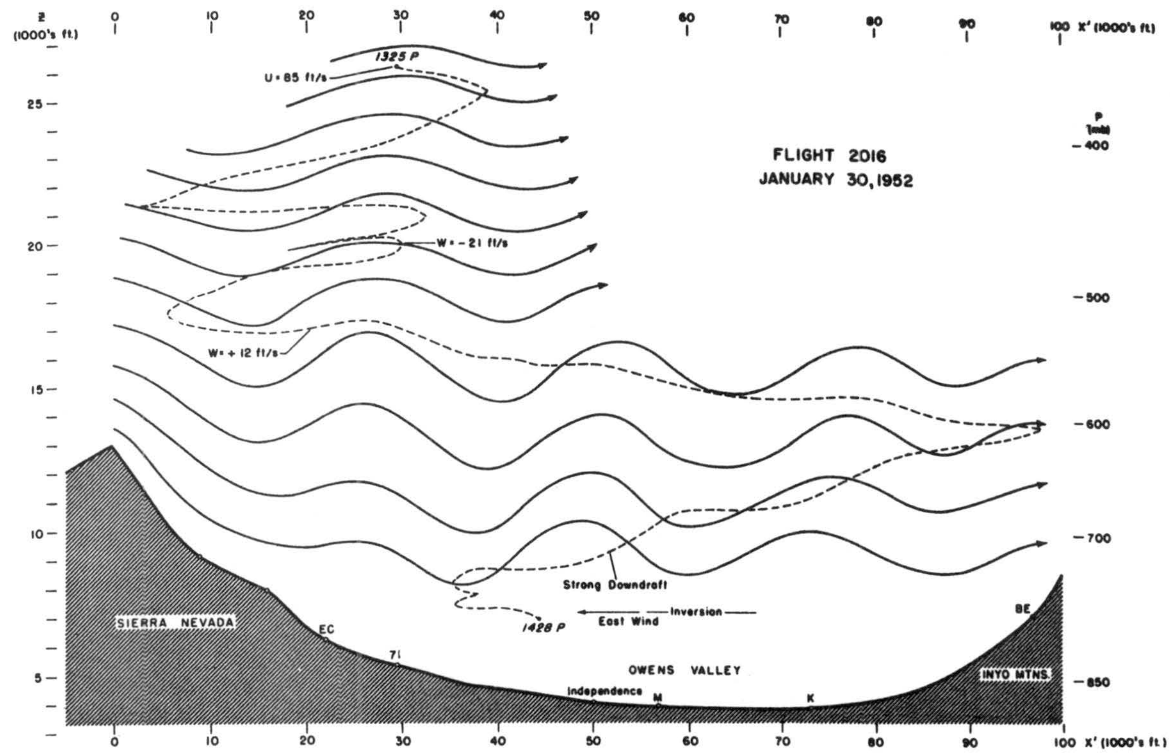

Fig. 4 Vertical cross section of flow patterns on the lee side of Sierra Nevada Fr = 0.14

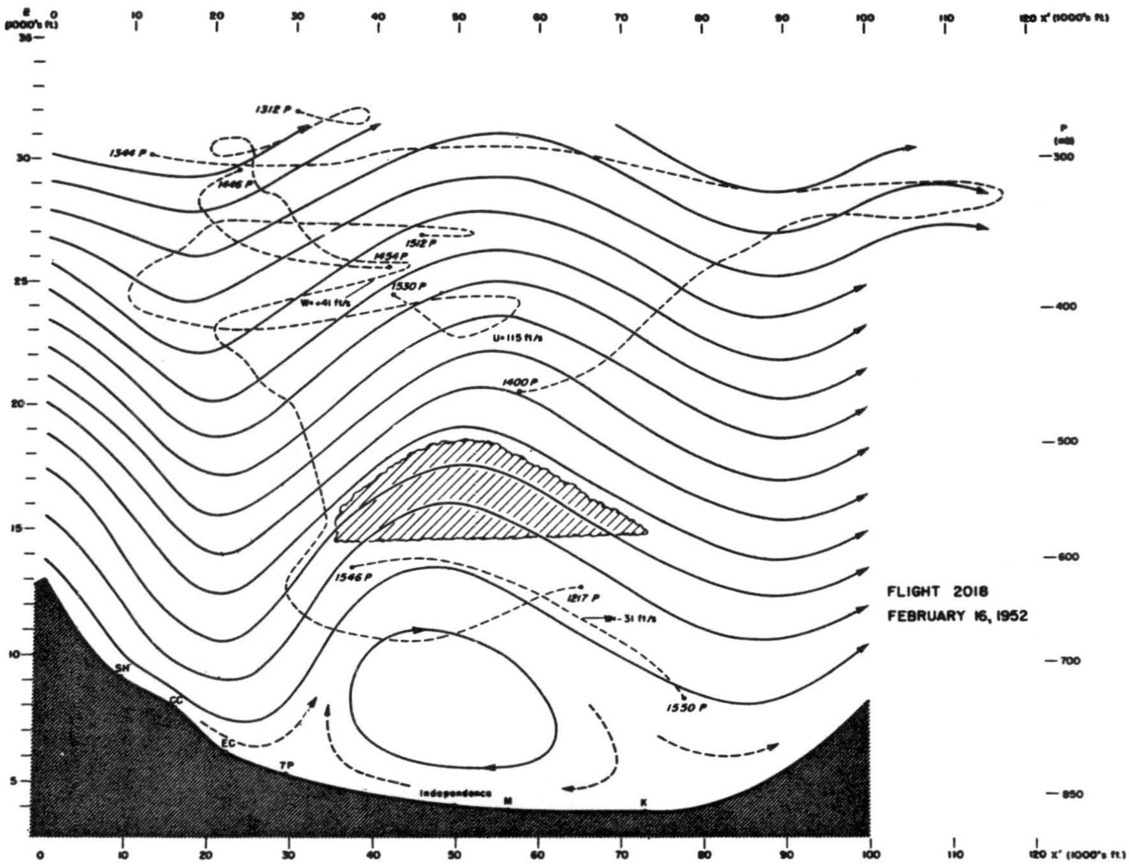

Fig. 5 Vertical cross section of flow patterns on the lee side of Sierra Nevada Fr = 0.24

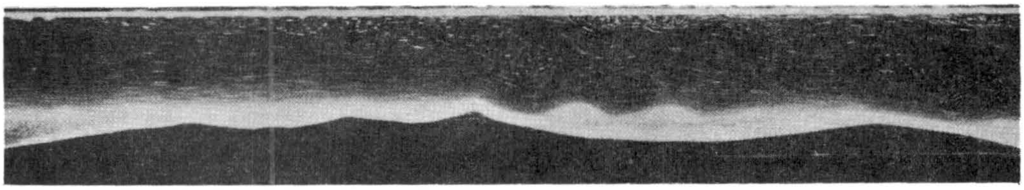

(a)

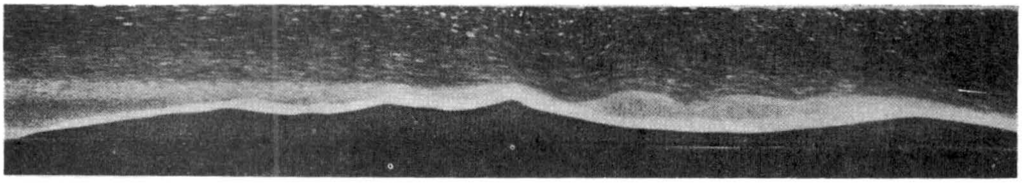

(b)

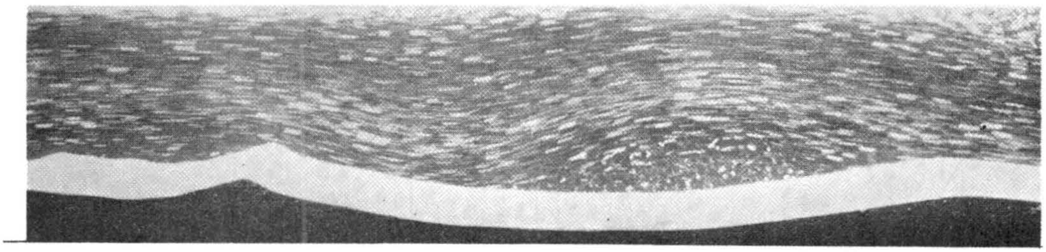

(c)

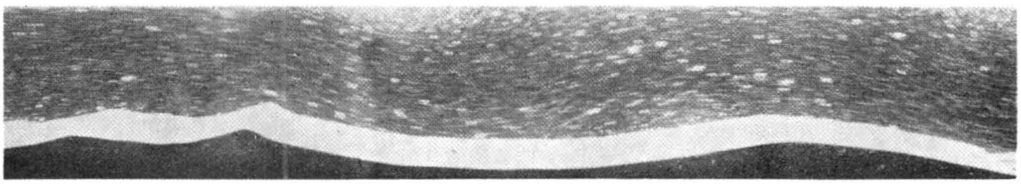

(d)

Fig. 6 Simulated Sierra Nevada lee-waves of Long's liquid model - single-fluid flow
a) Fr = 0.058 b) Fr = 0.103
c) Fr = 0.258 d) Fr = 0.283

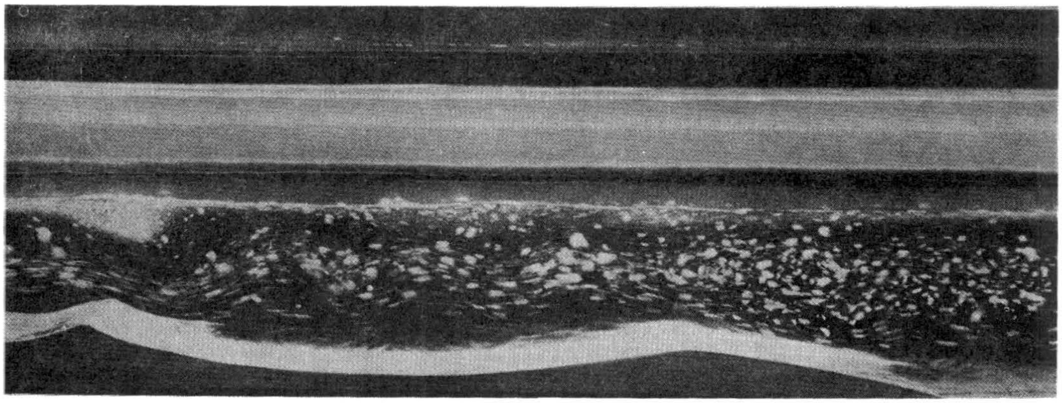

(a)

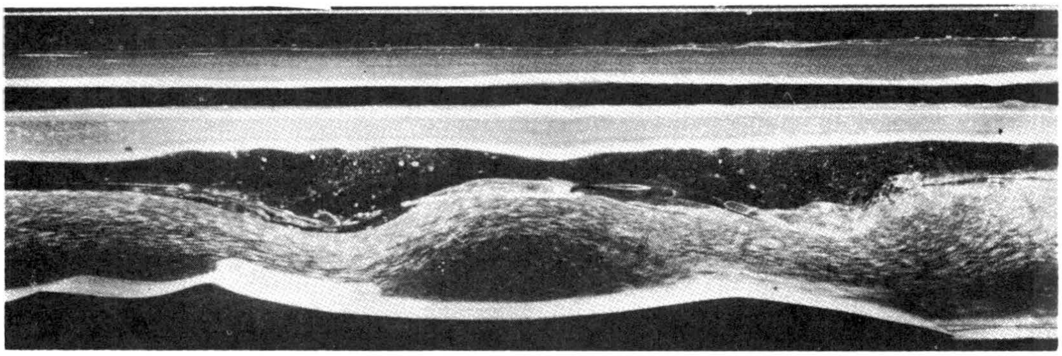

(b)

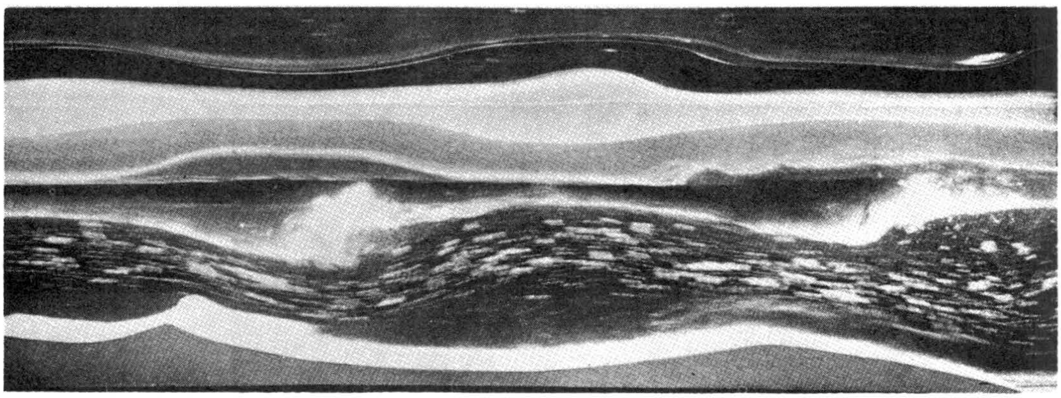

(c)

Fig. 7 Simulated Sierra Nevada lee-waves of Long's liquid model - multi-fluid flow
a) h=13 cm, $\Delta\rho/\overline{\rho}$=0.117, Fr=0.105
b) h=13 cm, $\Delta\rho/\overline{\rho}$=0.108, Fr=0.219
c) h=13 cm, $\Delta\rho/\overline{\rho}$=0.105, Fr=0.264

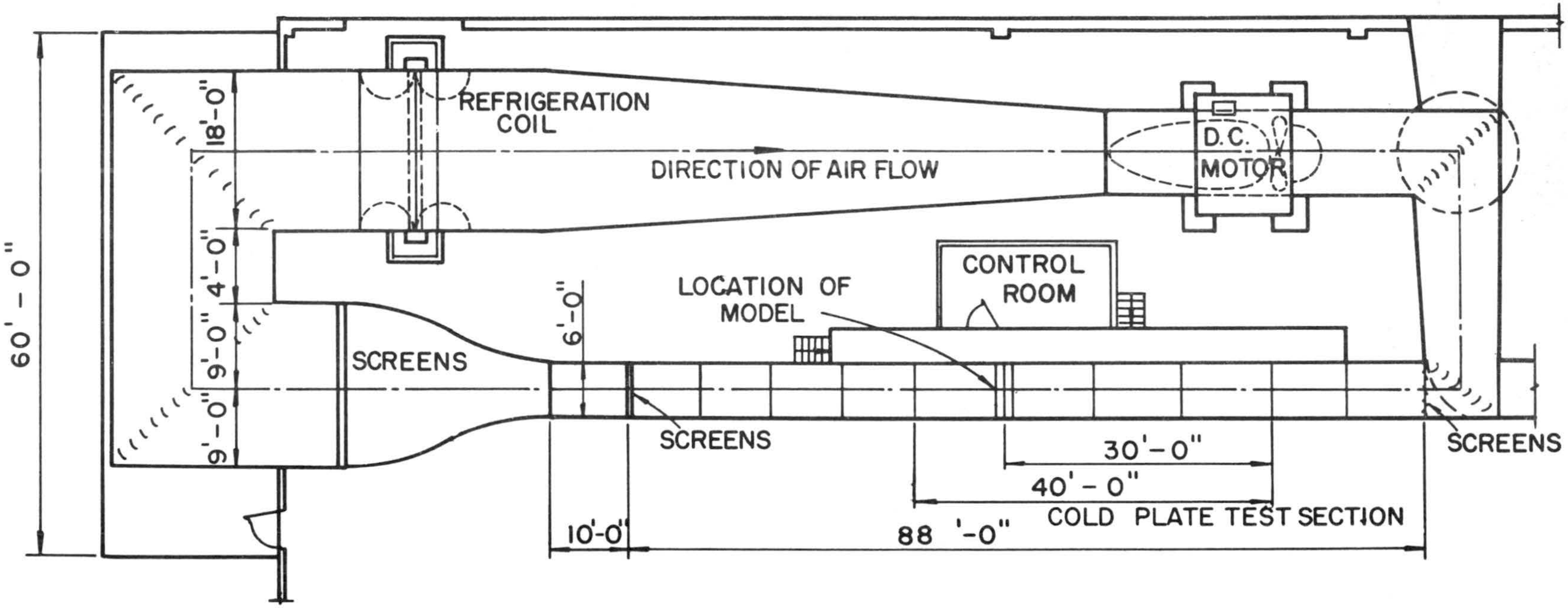

Fig. 8 Plan view of Army Micro Meteorological Wind Tunnel

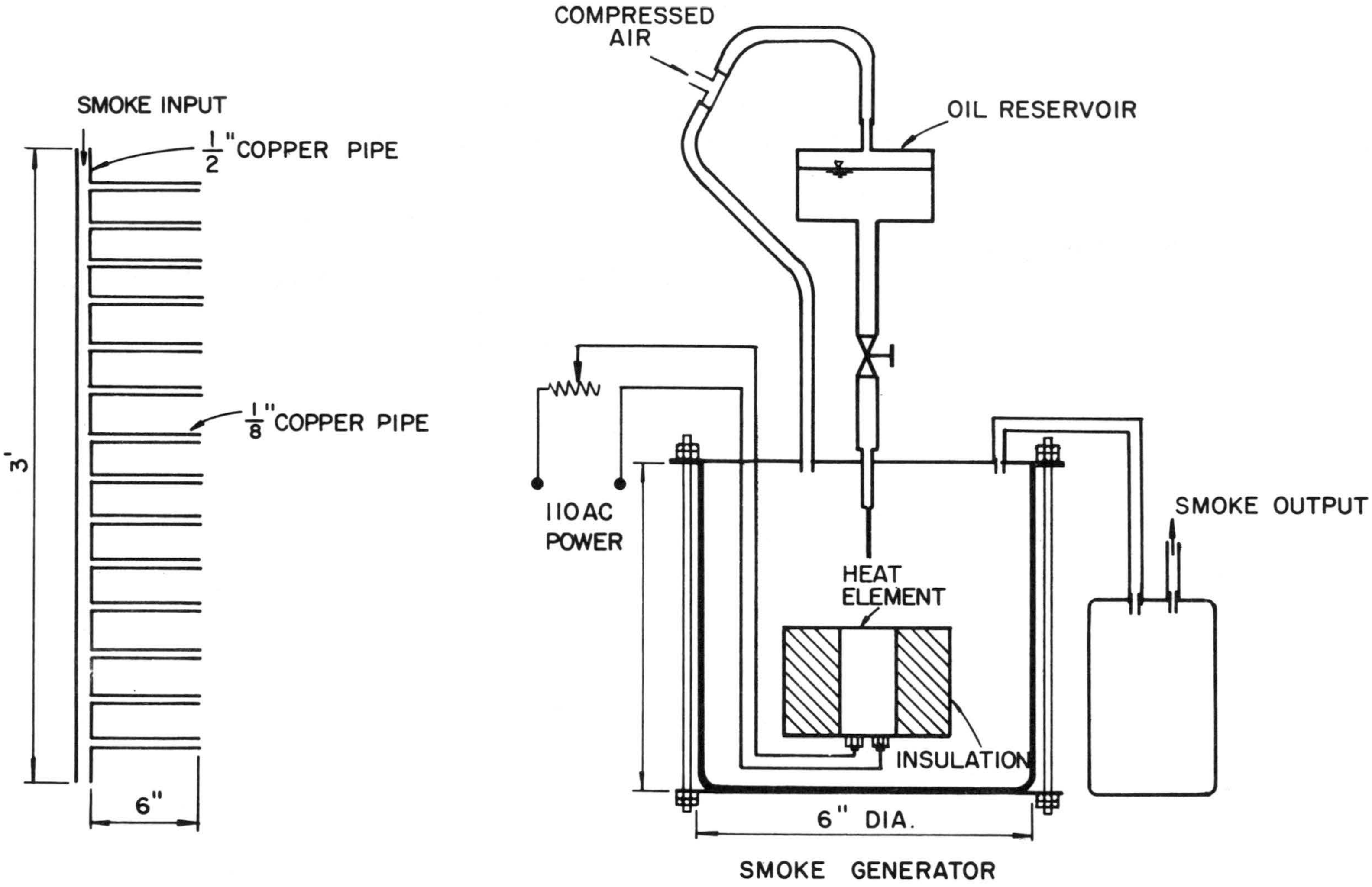

Fig. 9 Sketch of smoke generator and smoke rake

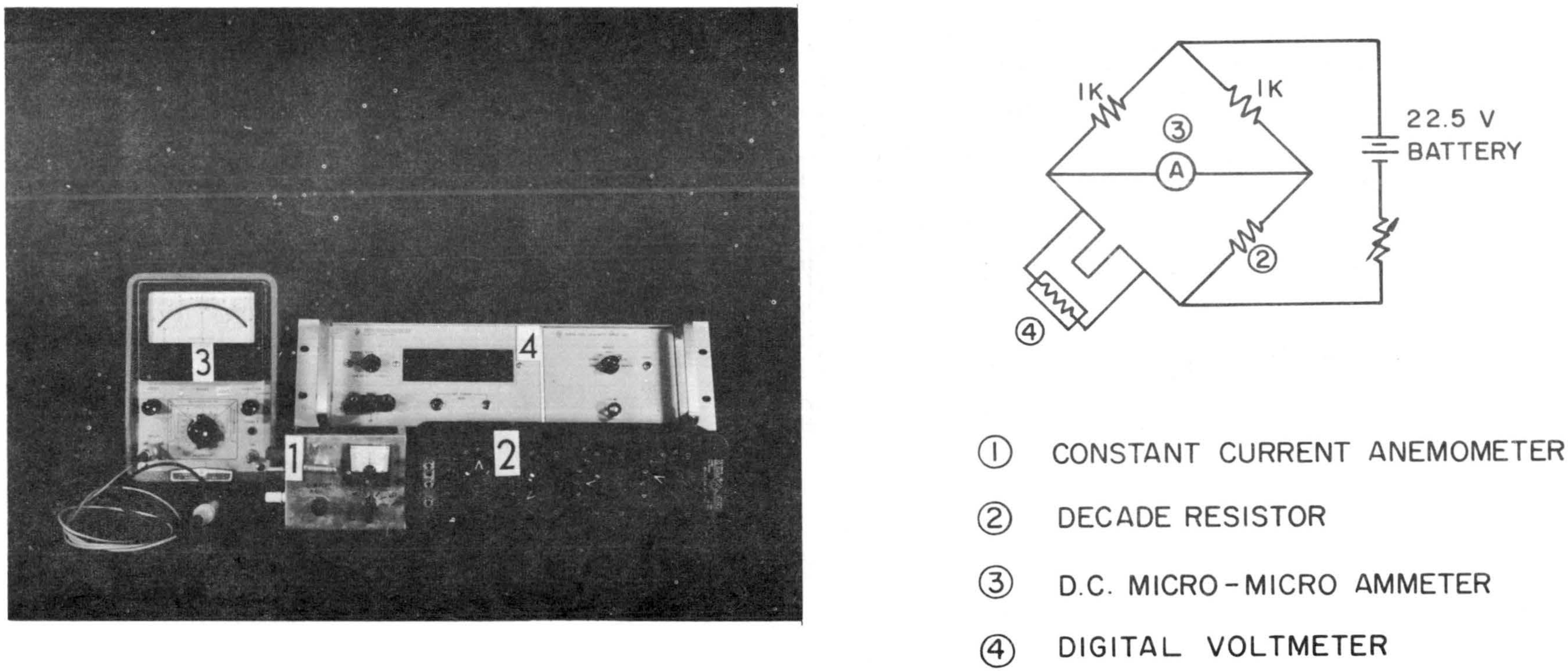

Fig. 10 The circuit of the resistance thermometer and the support instrumentation

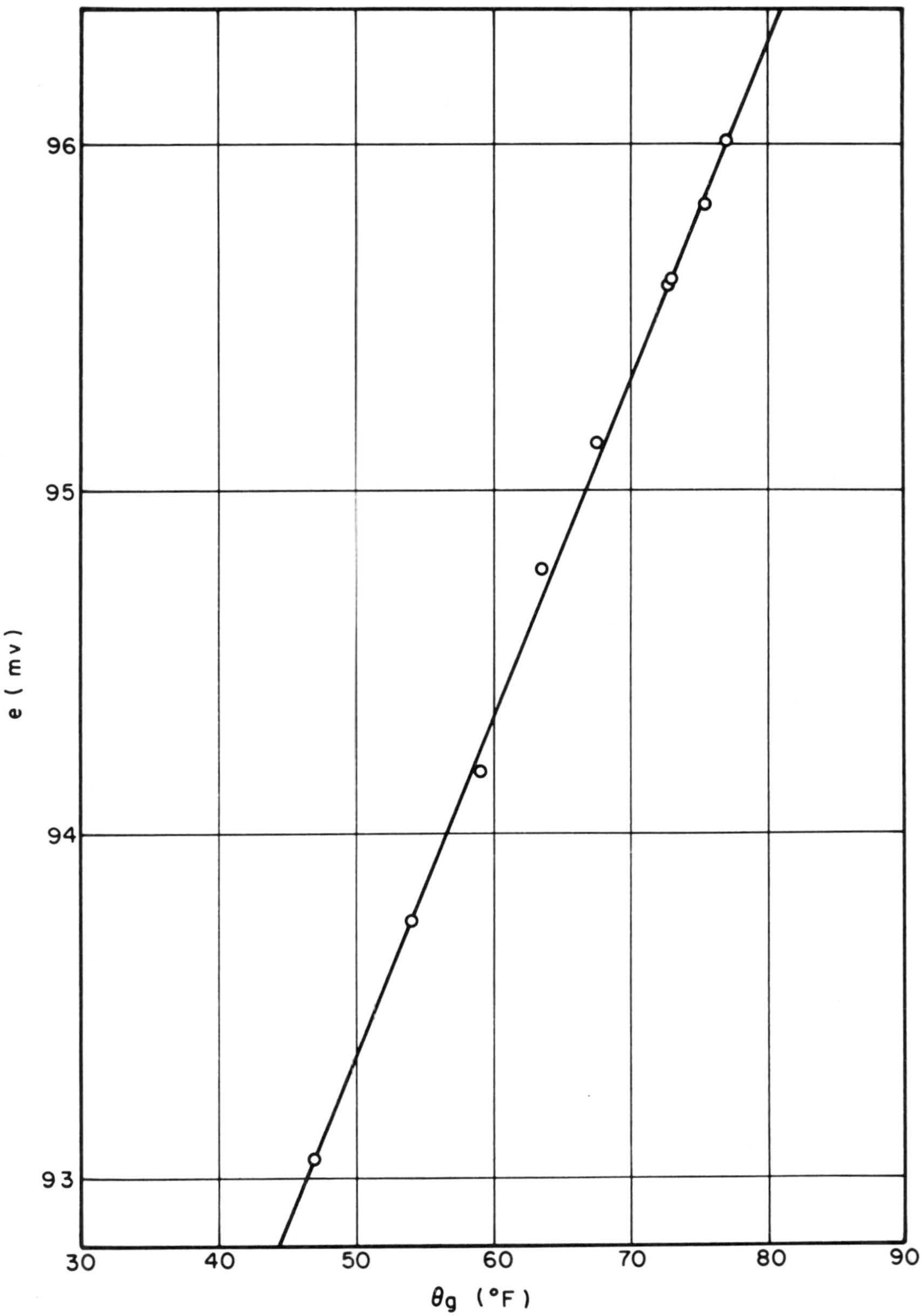

Fig. 11 Calibration curve of resistance thermometer

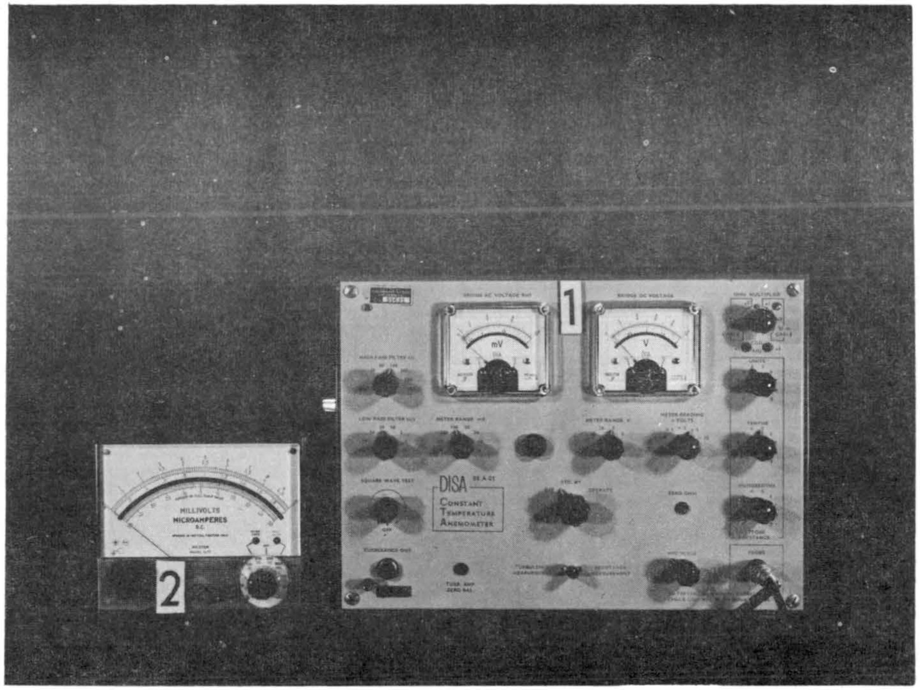

1. Disa (model 55A01) constant temperature anemometer

2. Weston (model 1477) vacuum tube

Fig. 12 Instrumentation for velocity measurement

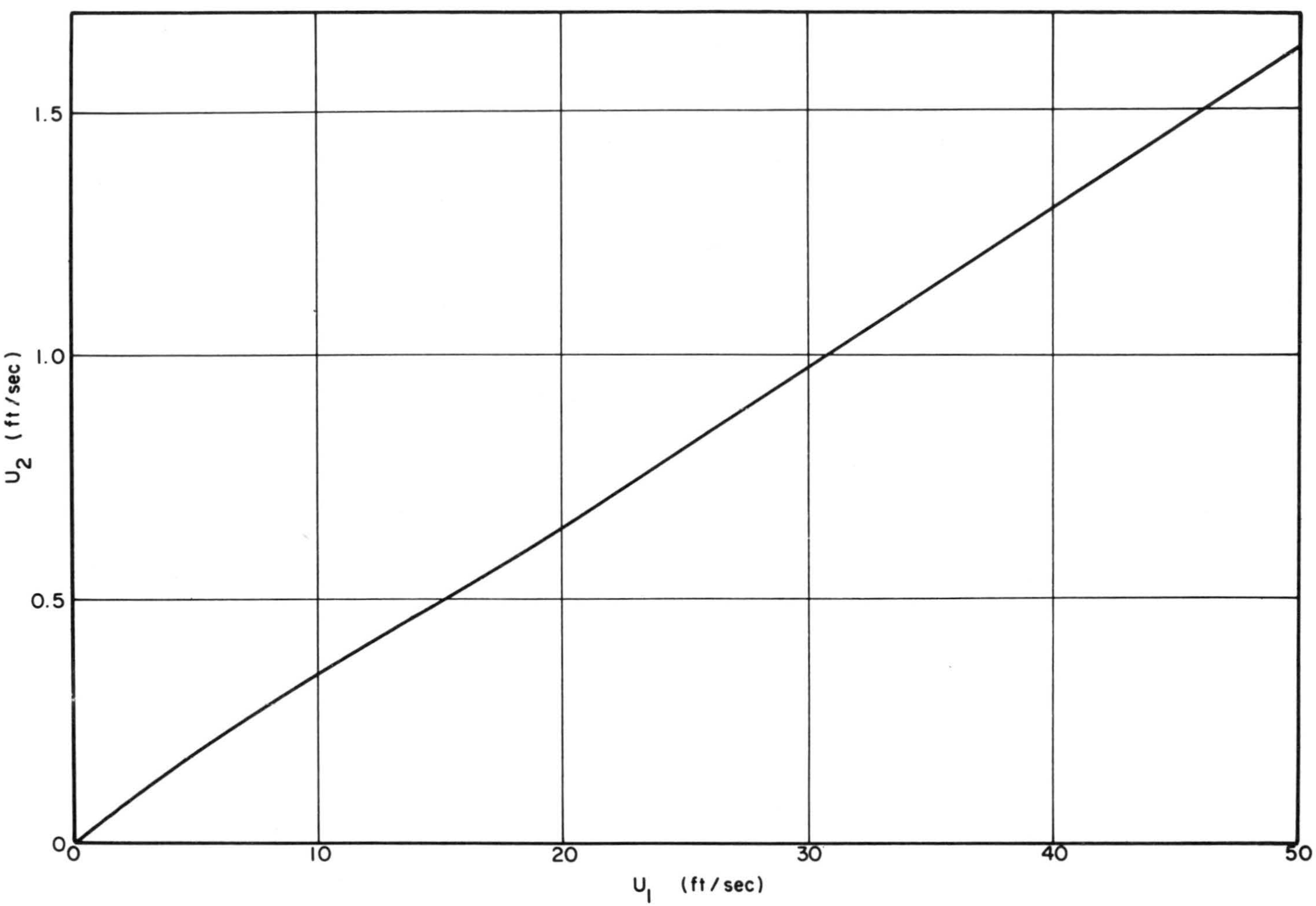

Fig. 13 Calibration curve of micro wind tunnel

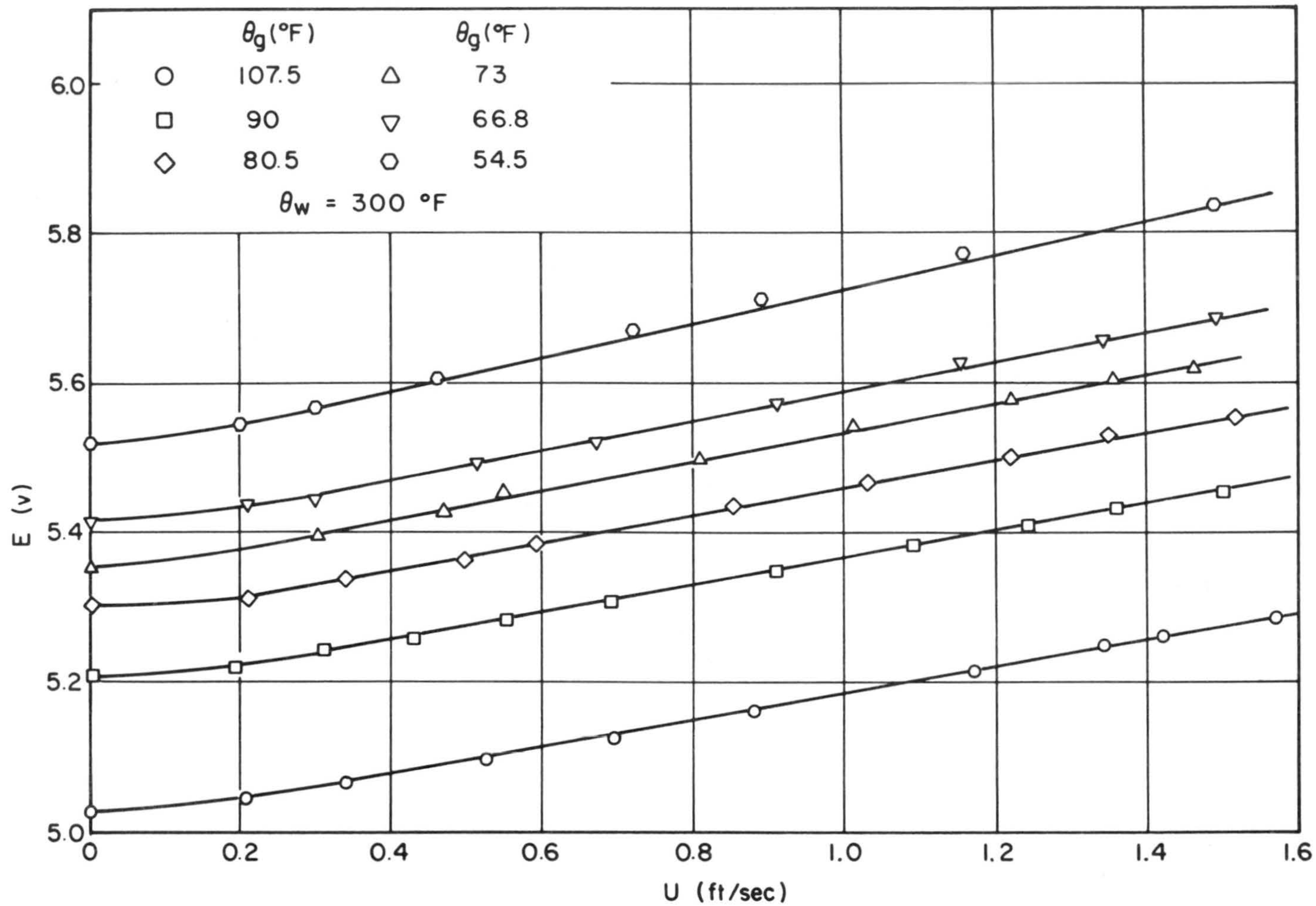

Fig. 14 Calibration curves of wire R_W = 4.37 ohms at various temperatures

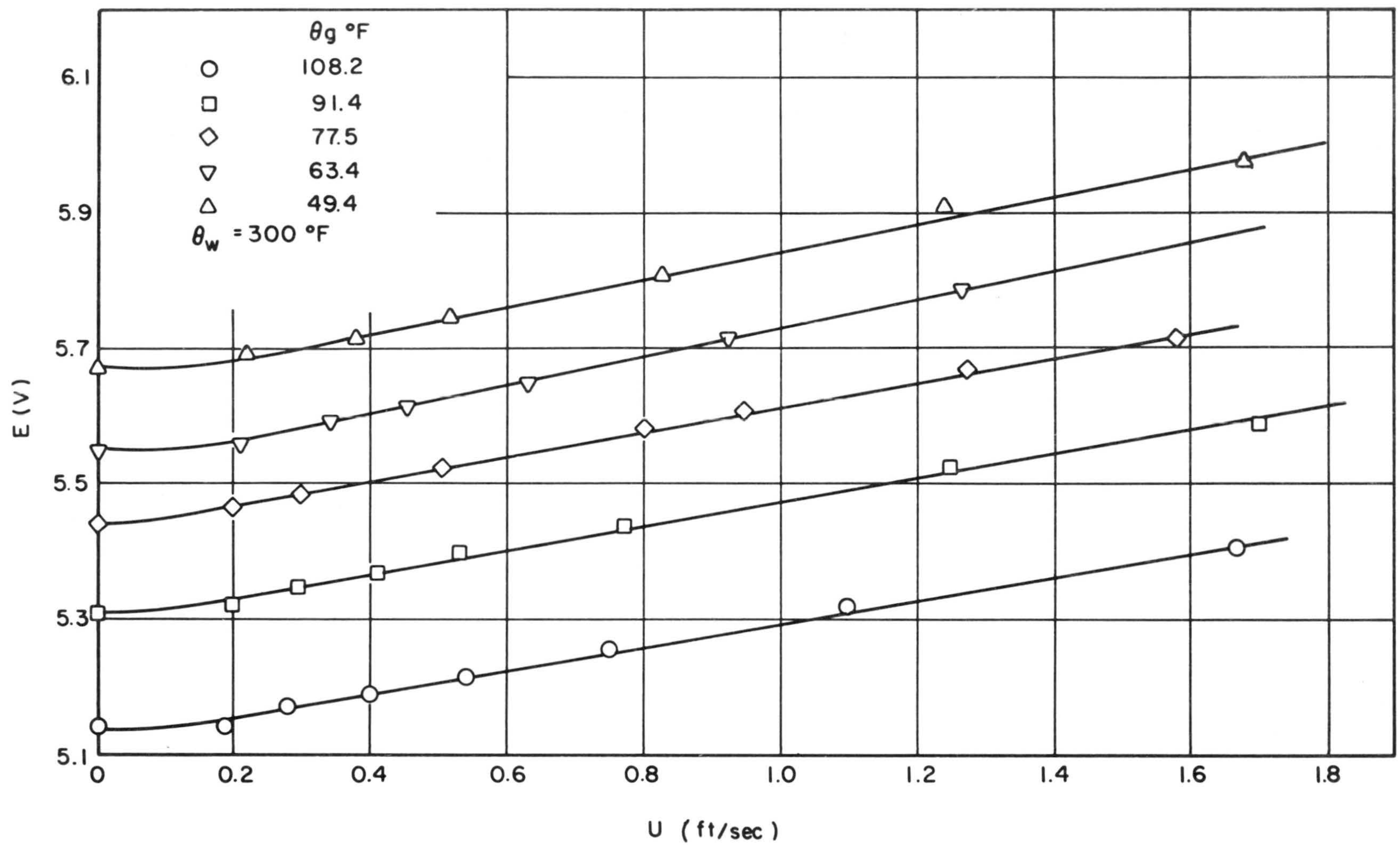

Fig. 15 Calibration curves of wire R_W = 4.39 ohms at various temperatures

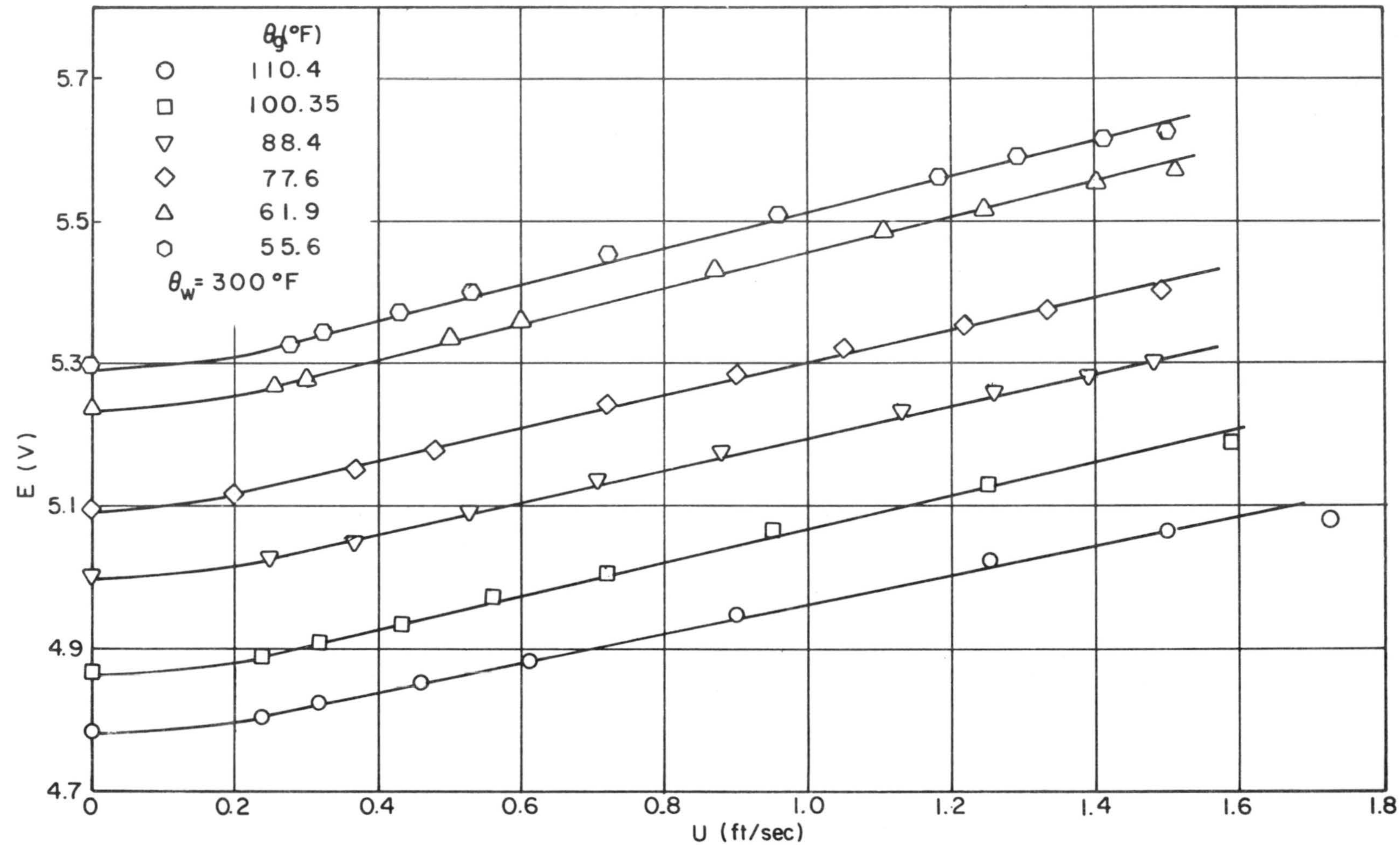

Fig. 16 Calibration curves of wire R_W = 4.64 ohms at various temperatures

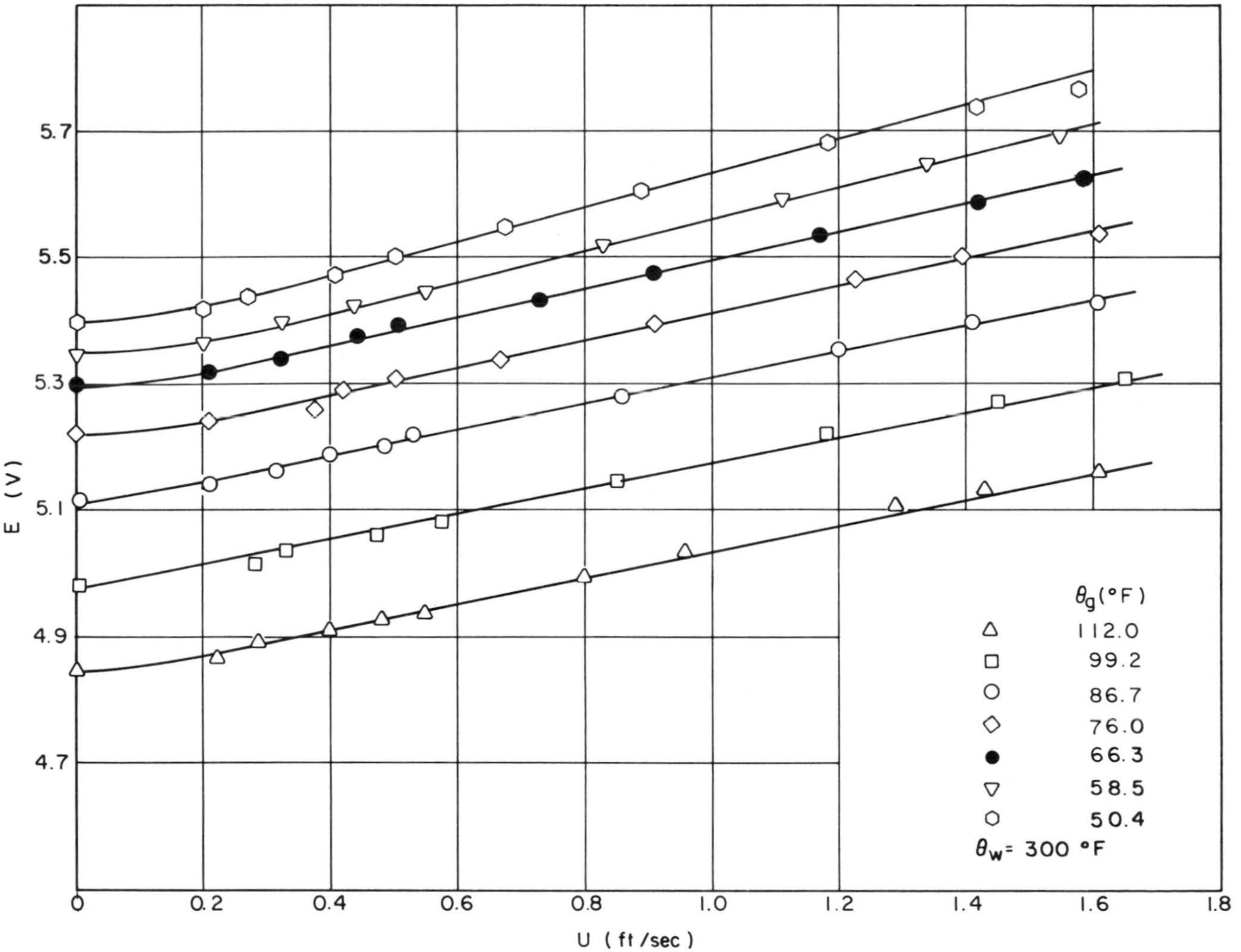

Fig. 17 Calibration curves of wire R_W = 4.7 ohms at various temperatures

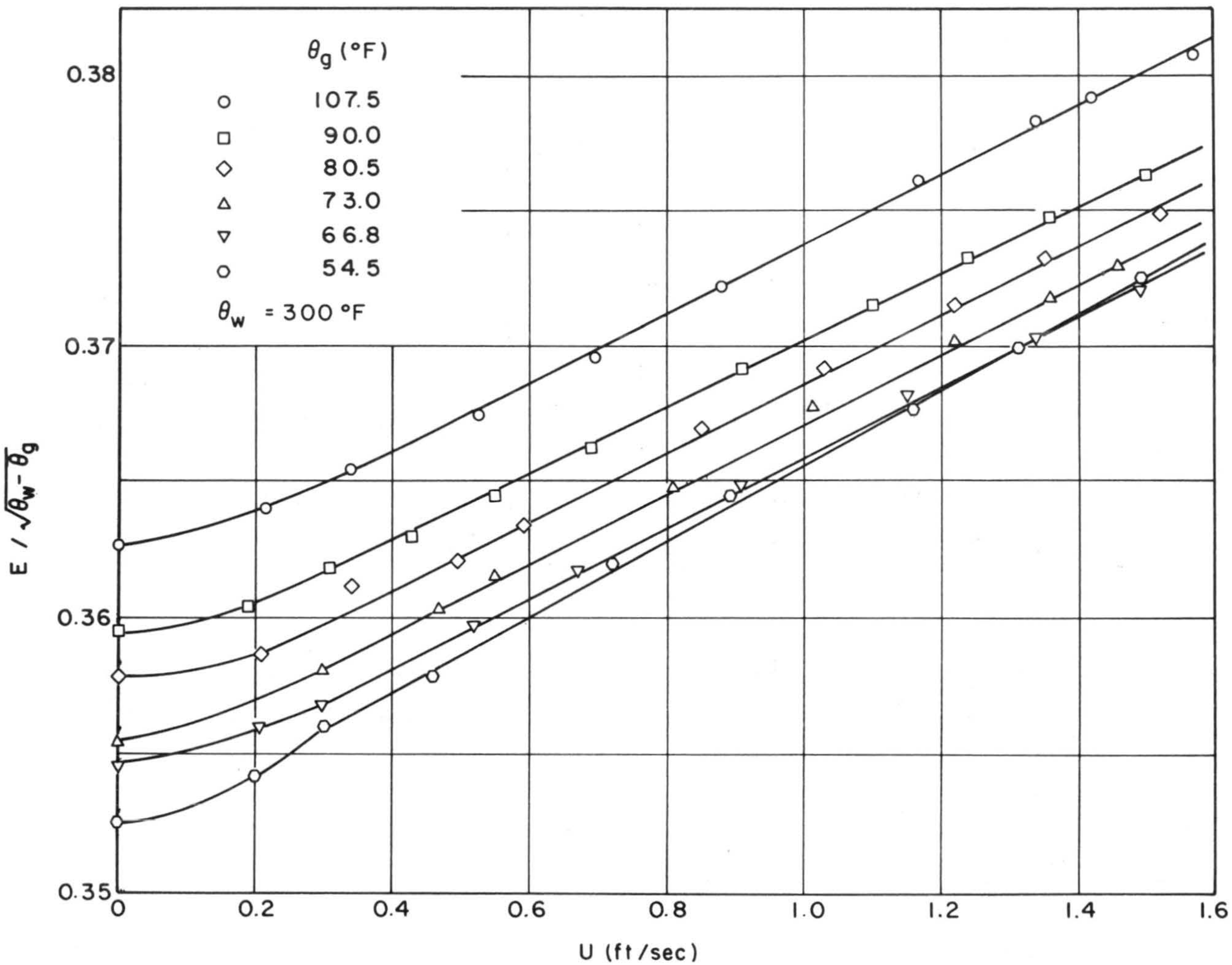

Fig. 18 Partly compensated calibration curves of wire R_w = 4.37 ohms

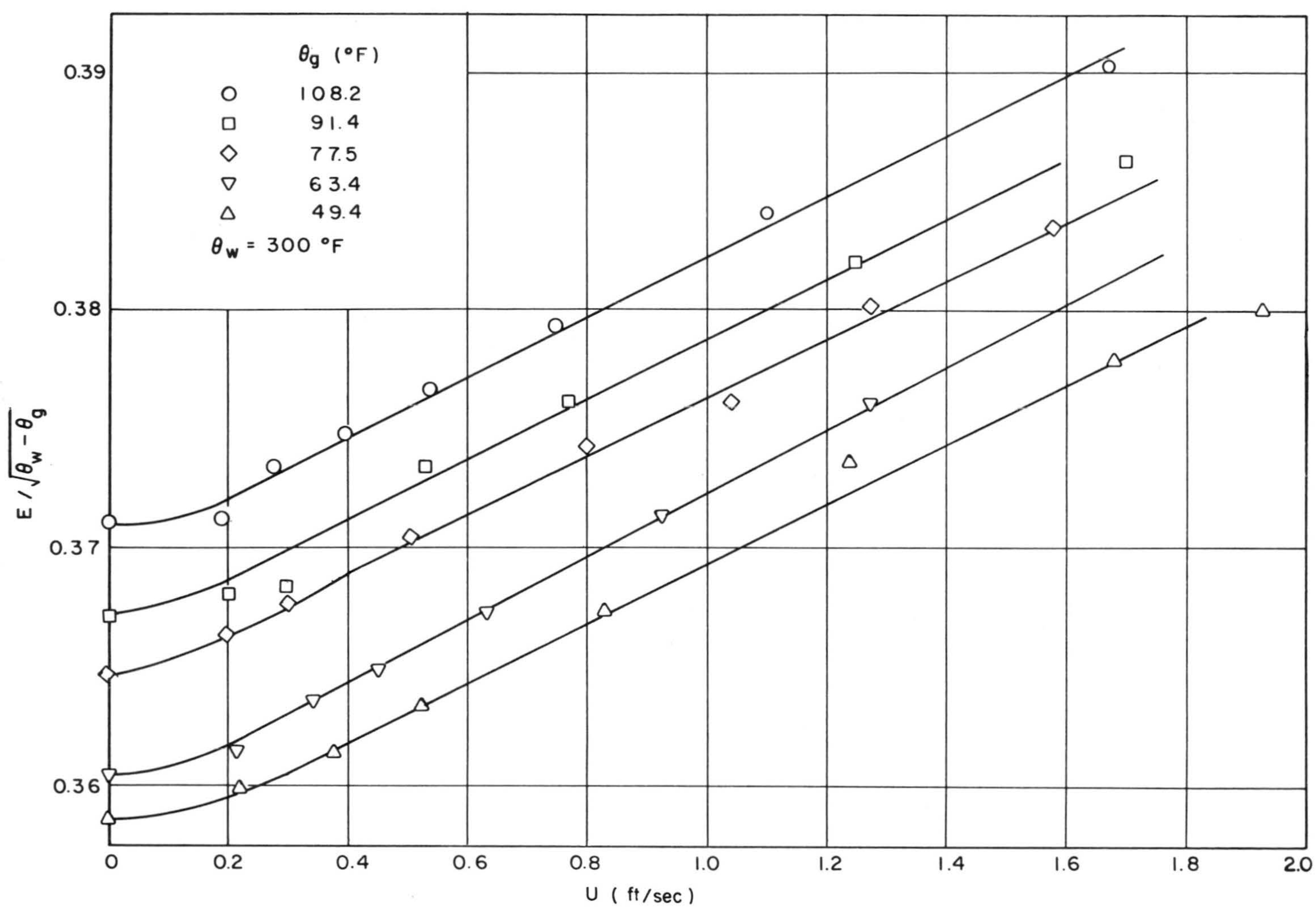

Fig. 19 Partly compensated calibration curves for wire R_W = 4.39 ohms

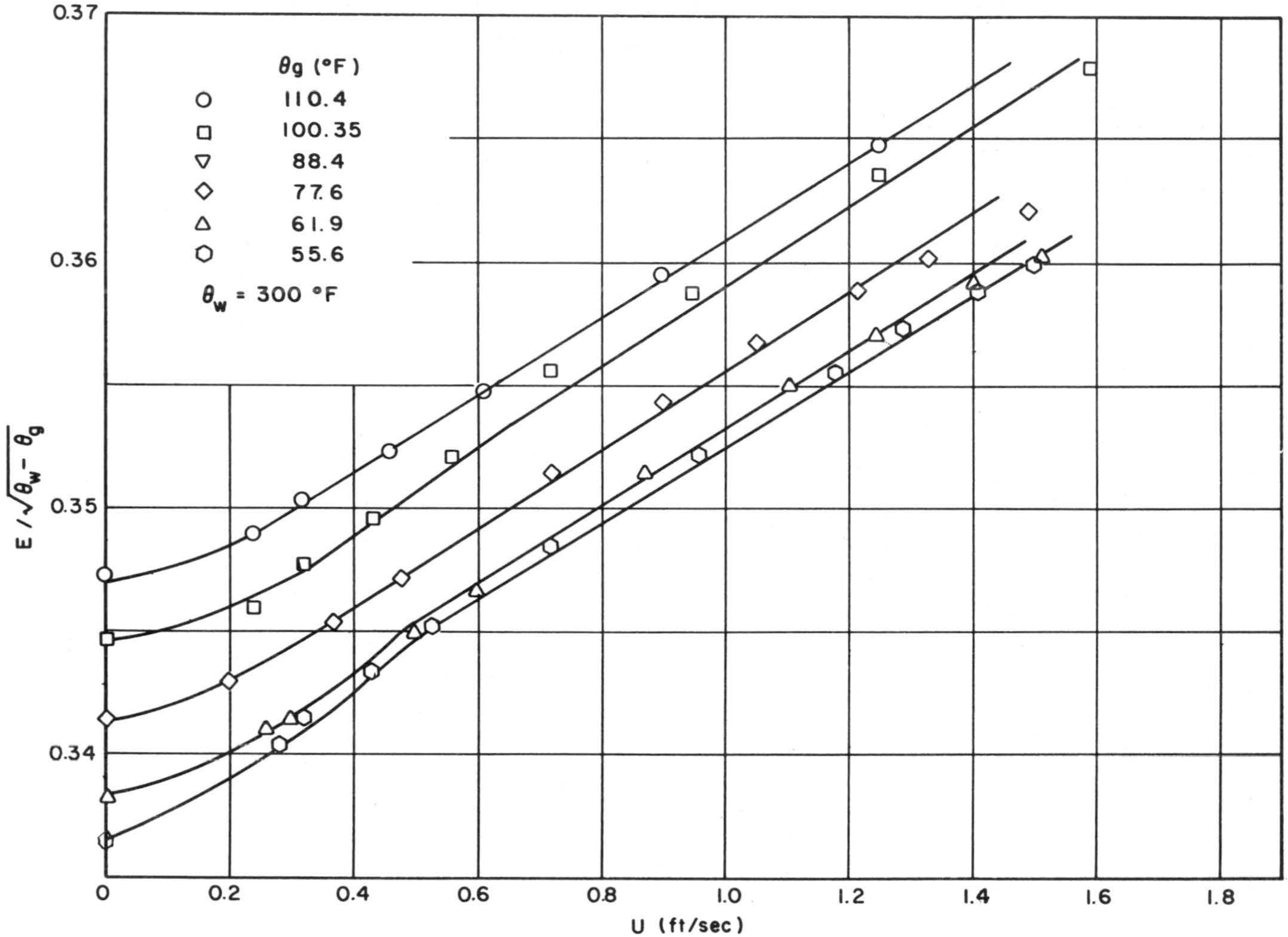

Fig. 20 Partly compensated calibration curves for wire R_W = 4.64 ohms

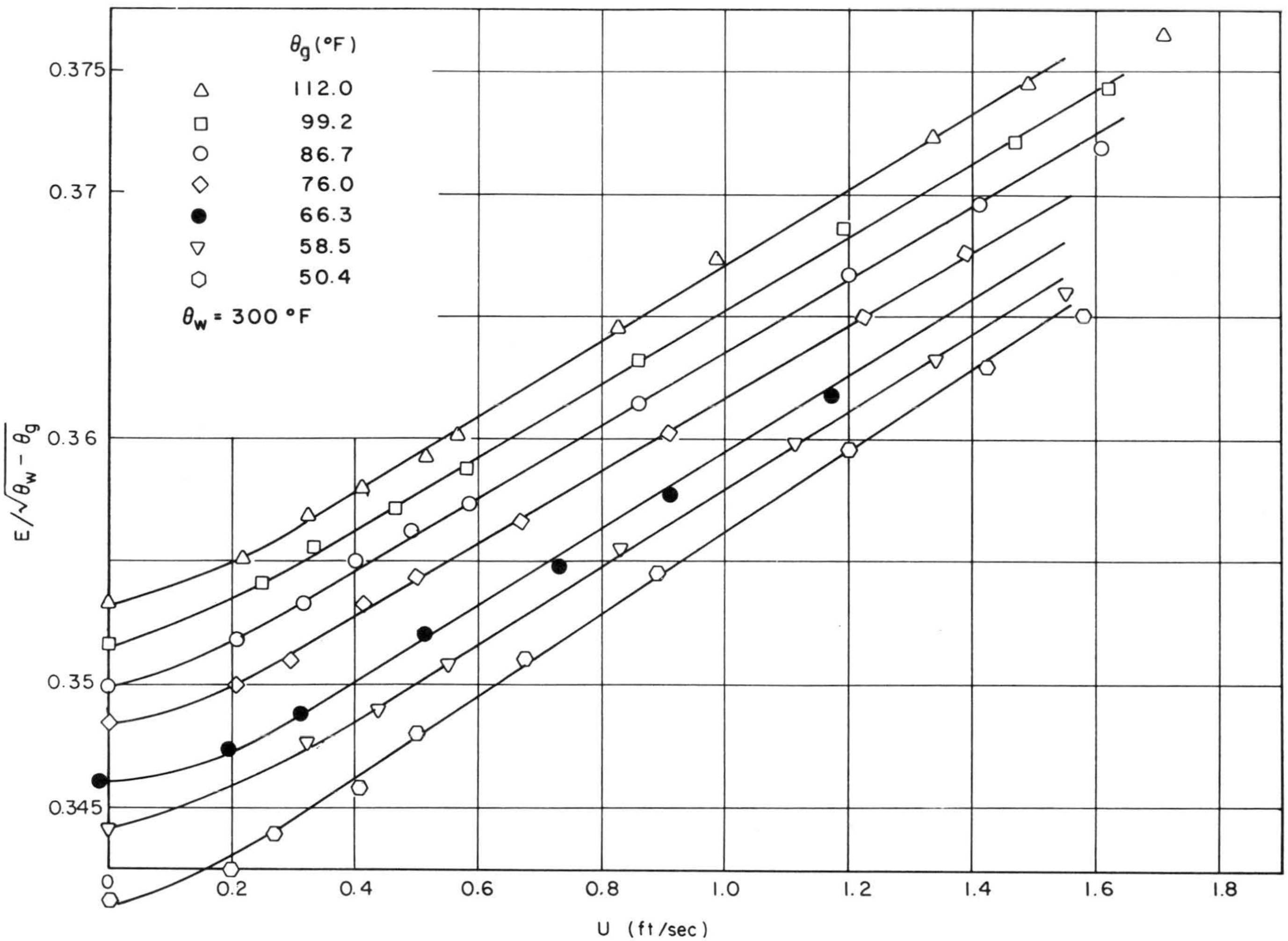

Fig. 21 Partly compensated calibration curves for wire R_W = 4.7 ohms

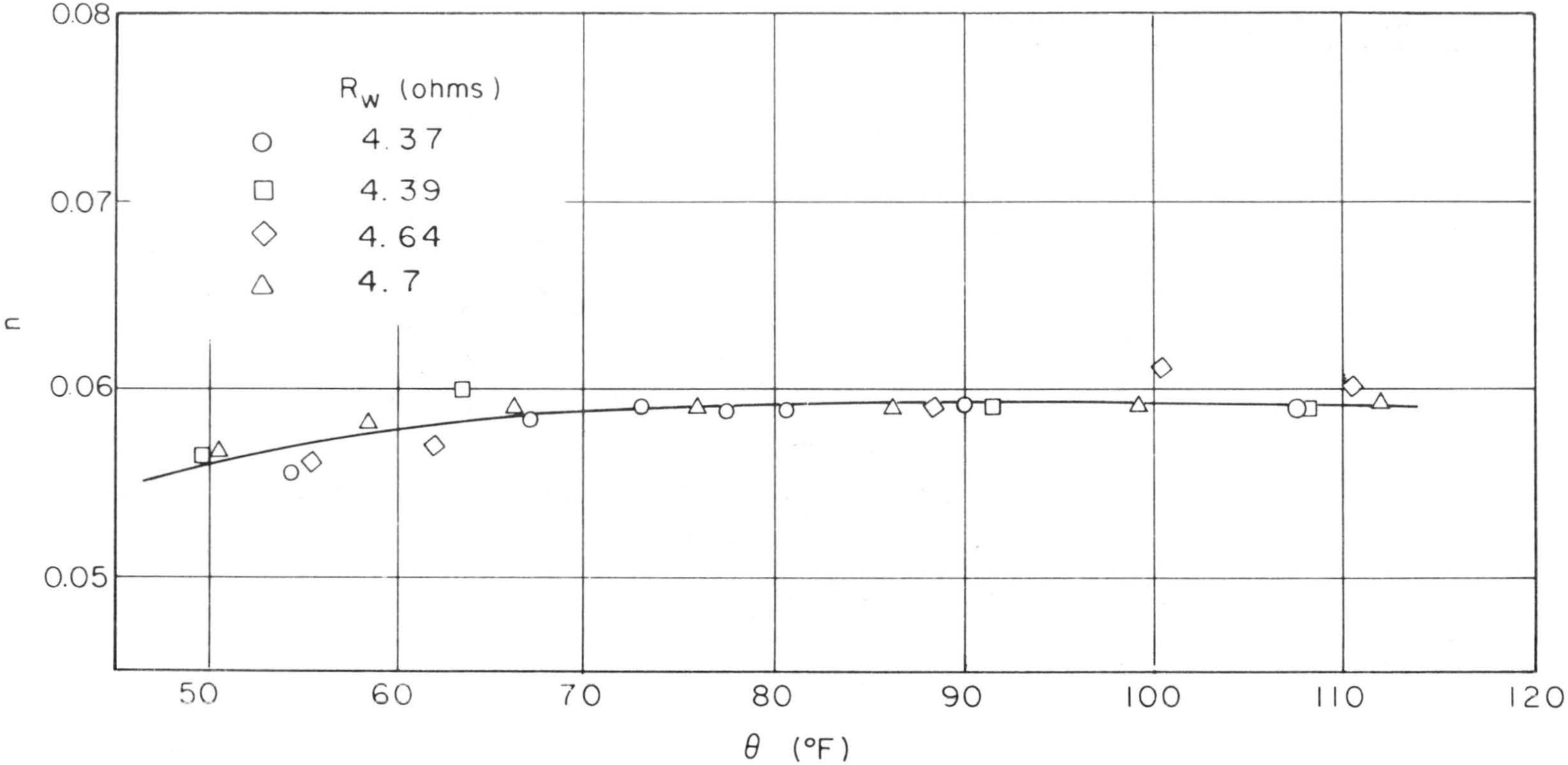

Fig. 22 Values of exponent n as a function of air temperature for four different wires

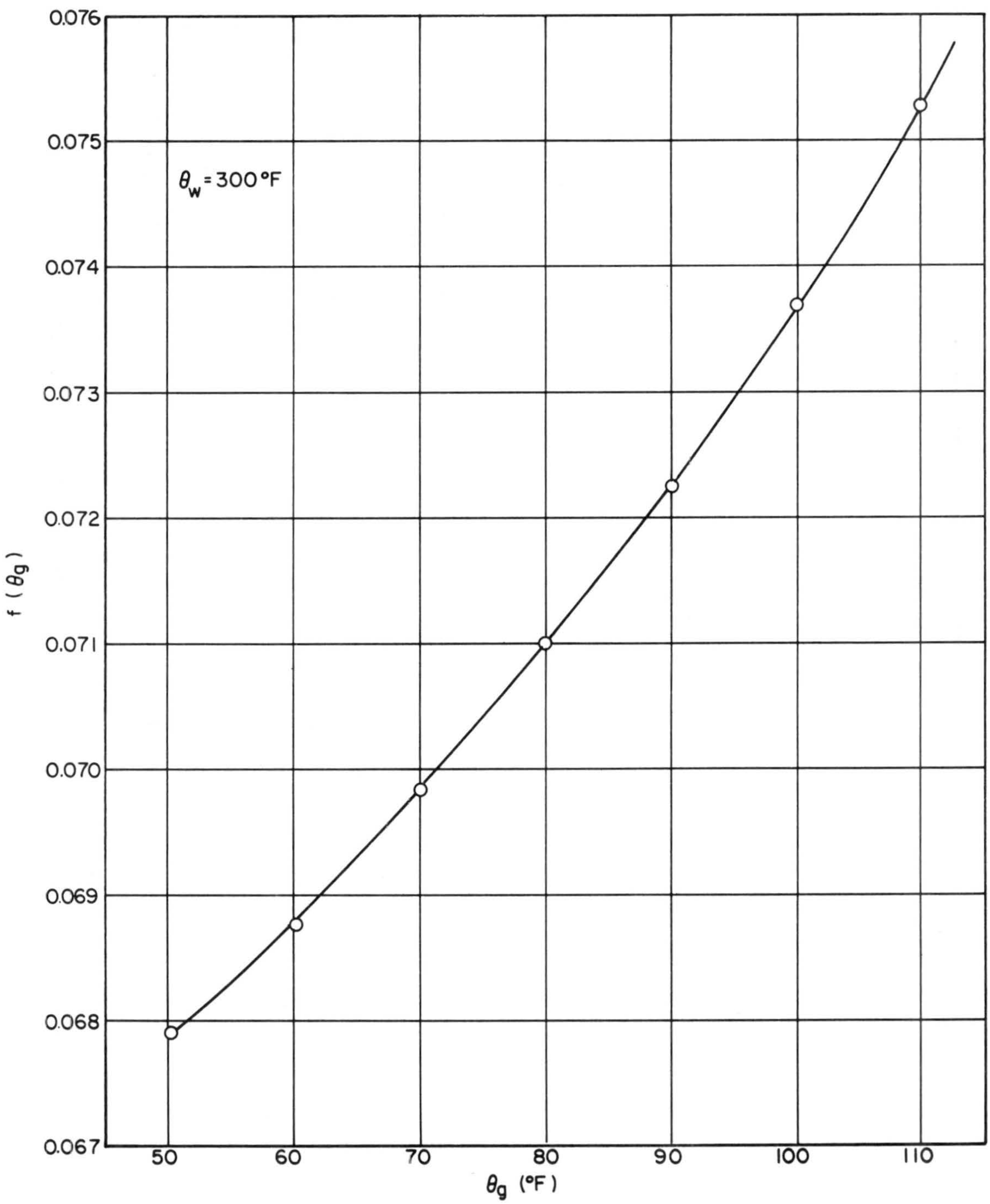

Fig. 23 Values of $f(\theta_g)$ as a function of air temperature

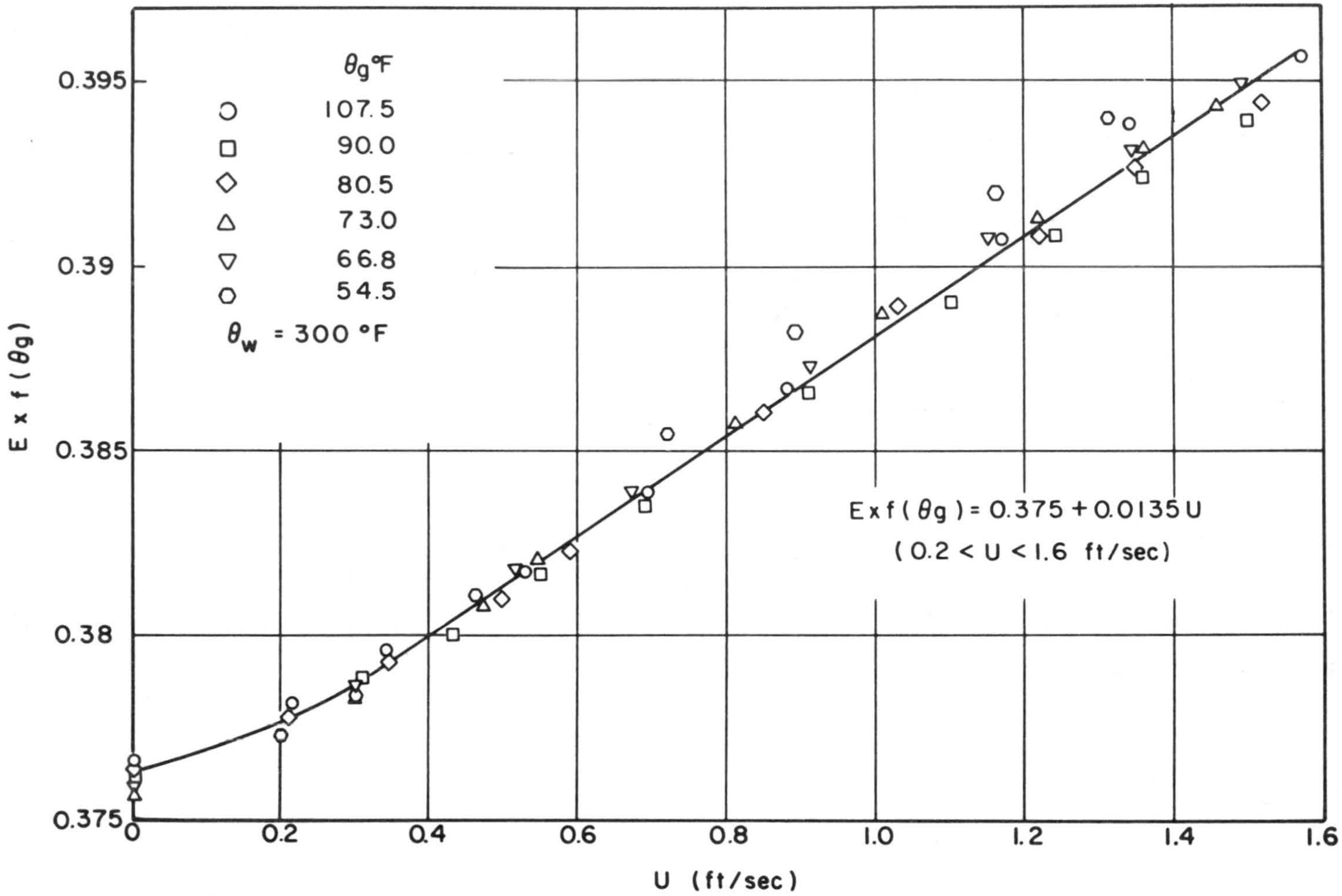

Fig. 24 Temperature compensated calibration curve for wire R_W = 4.37 ohms

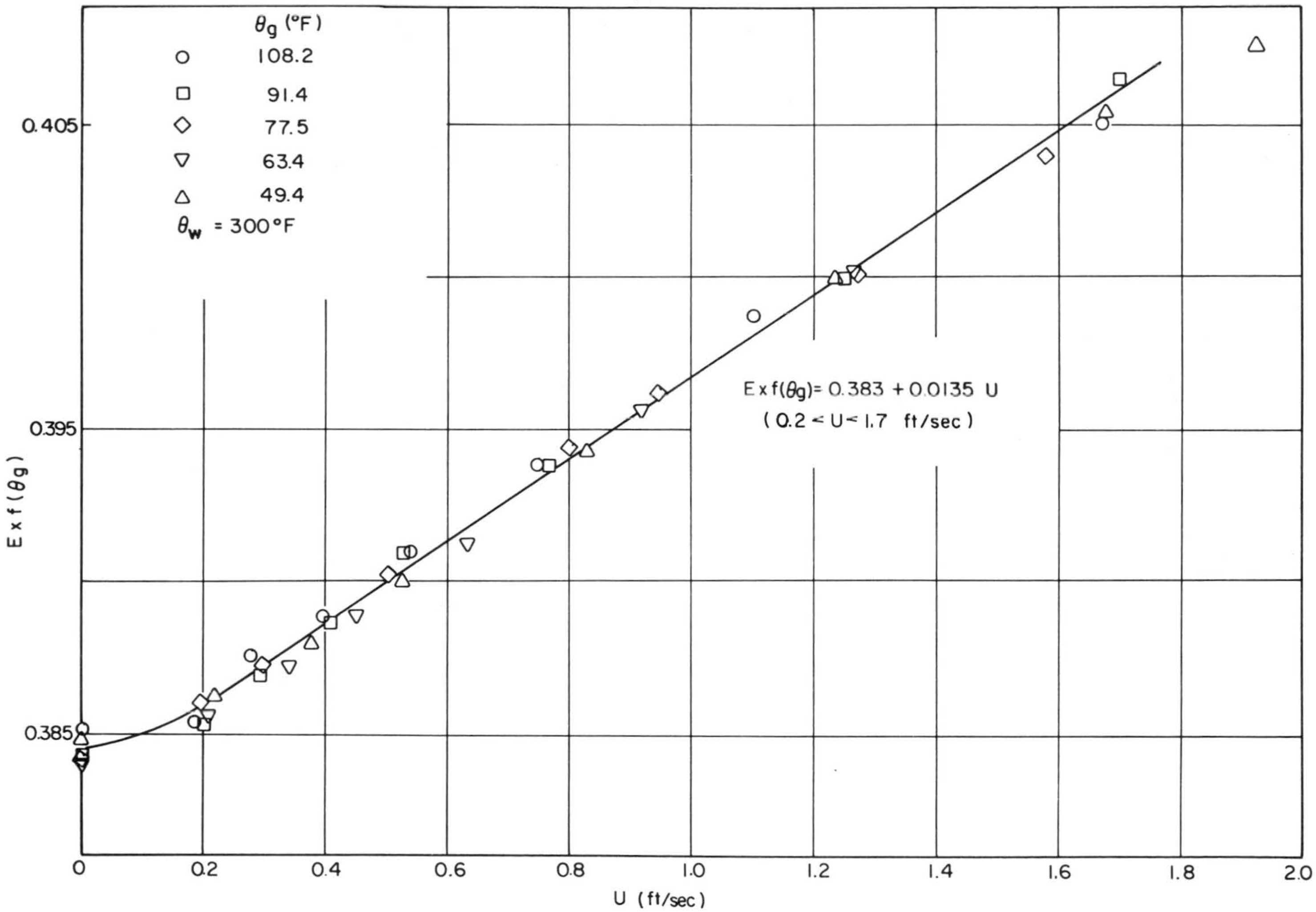

Fig. 25 Temperature compensated calibration curve for wire R_W = 4.39 ohms

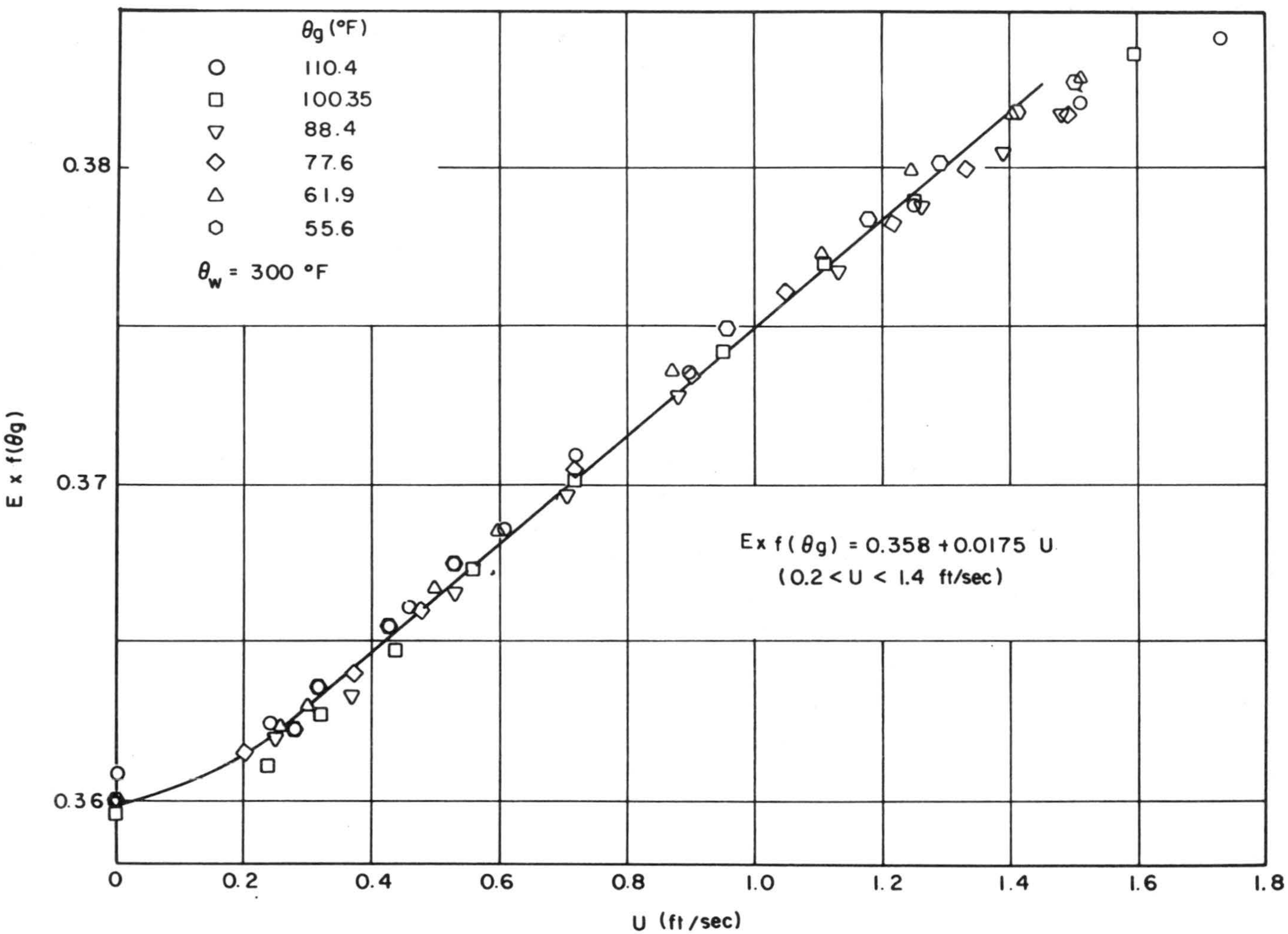

Fig. 26 Temperature compensated calibration curve for wire R_W = 4.64 ohms

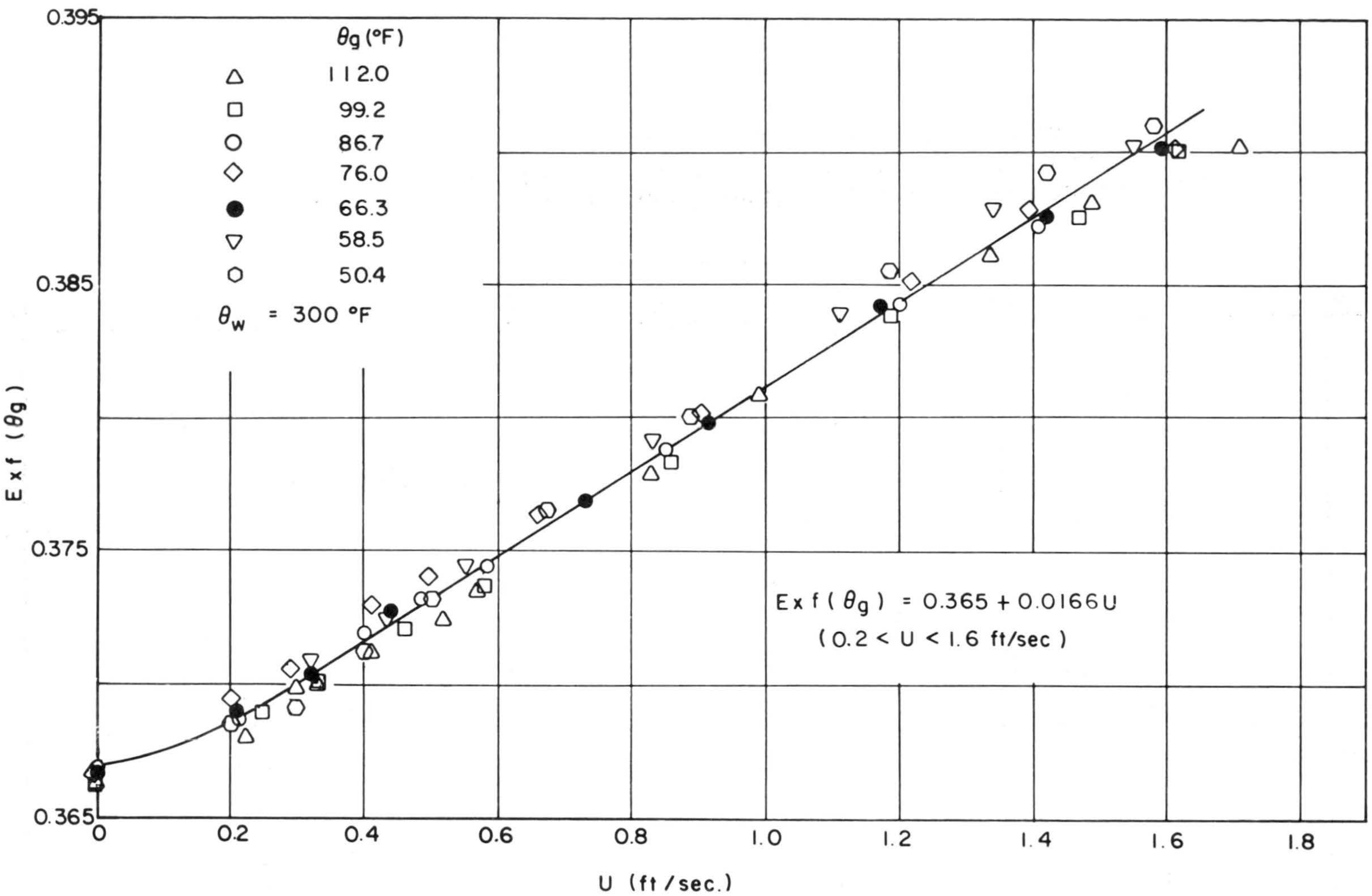

Fig. 27 Temperature compensated calibration curve for wire R_W = 4.7 ohms

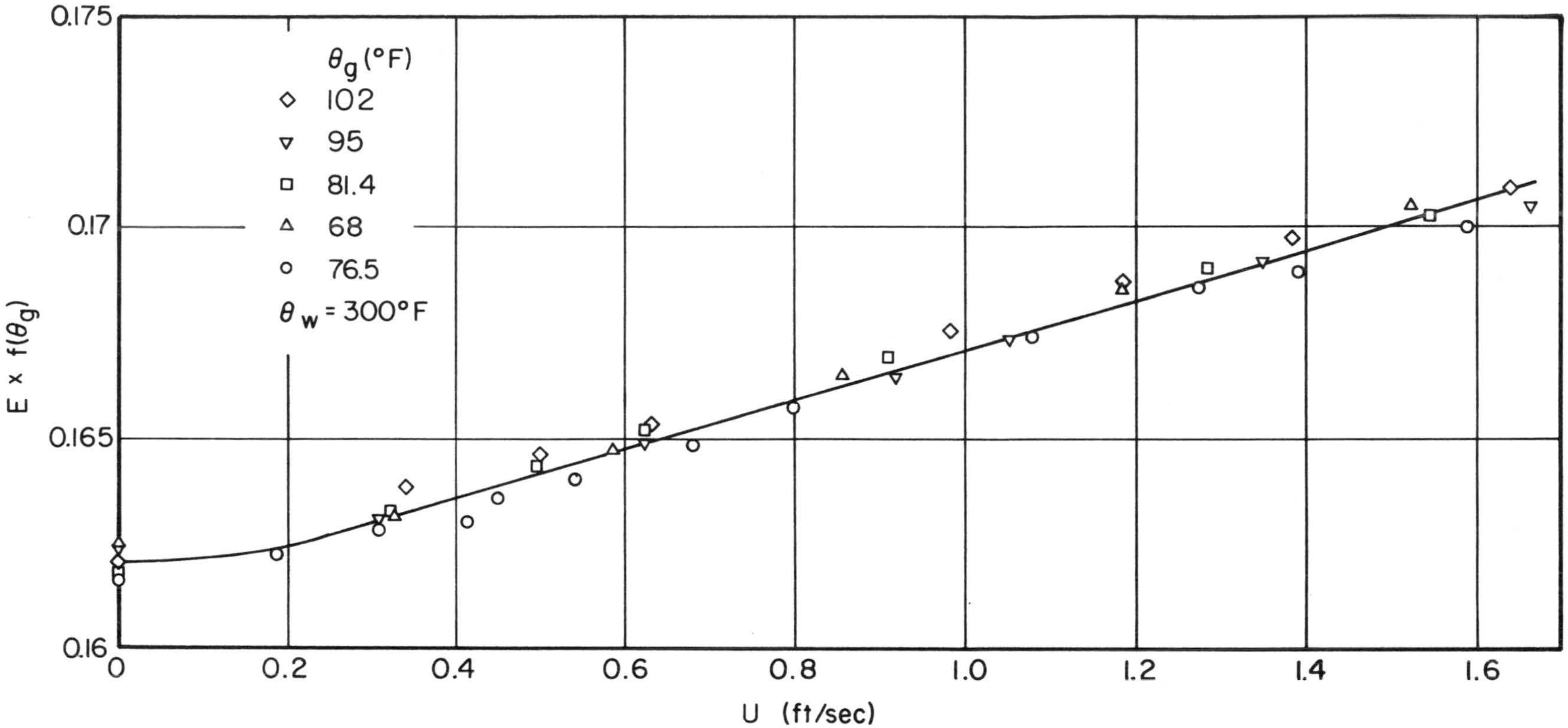

Fig. 28 Temperature compensated calibration curve for wire R_w = 4.69 ohms with Heat Flux System Constant Temperature Anemometer

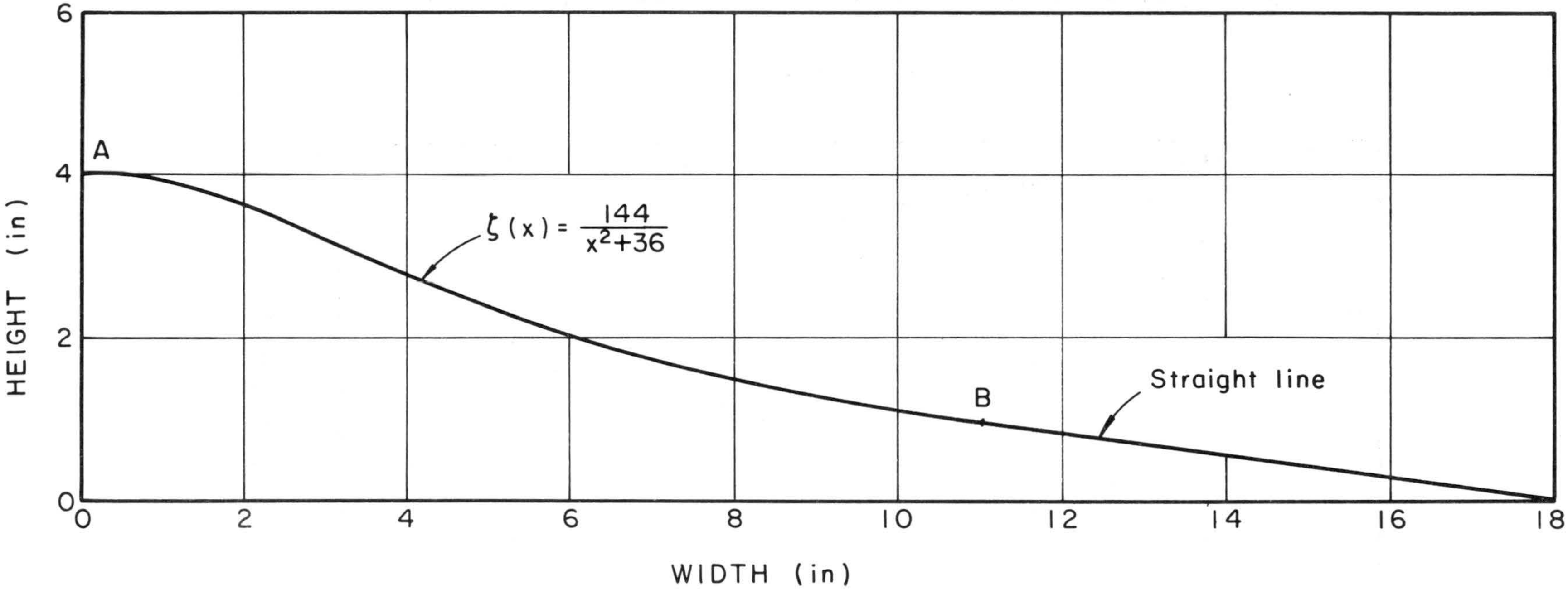

Fig. 29 Dimensions of simulated mountain model I

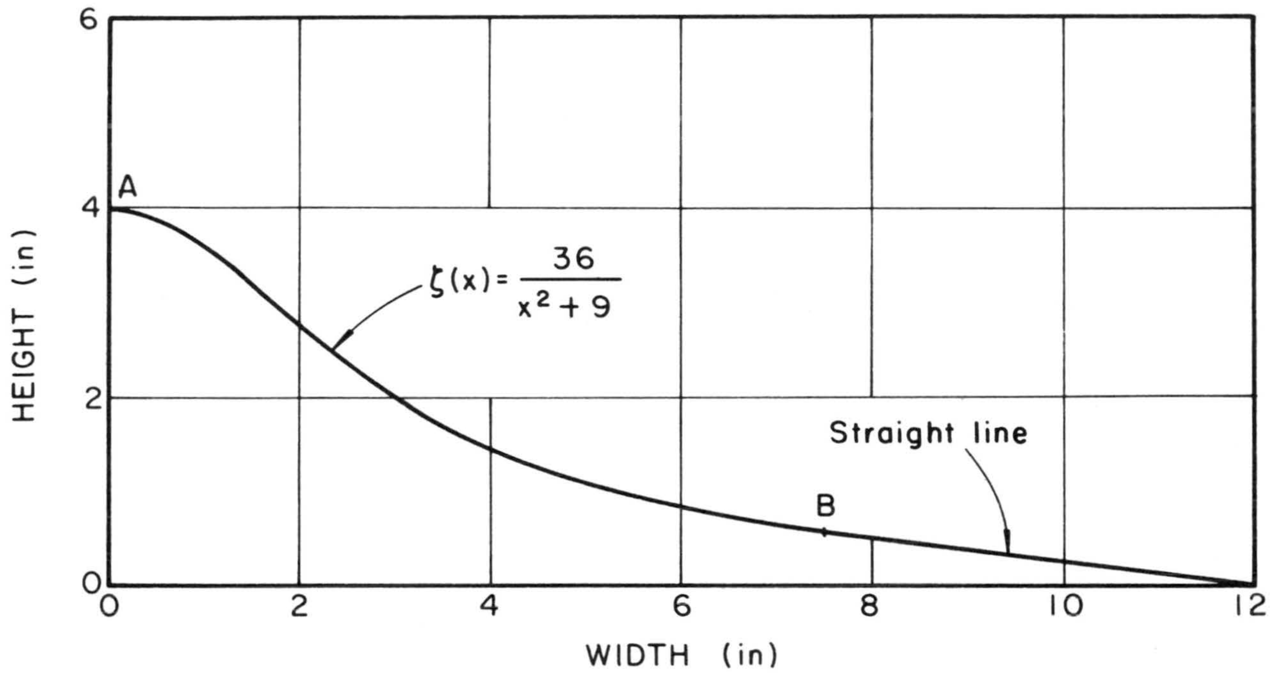

Fig. 30 Dimensions of simulated mountain model II

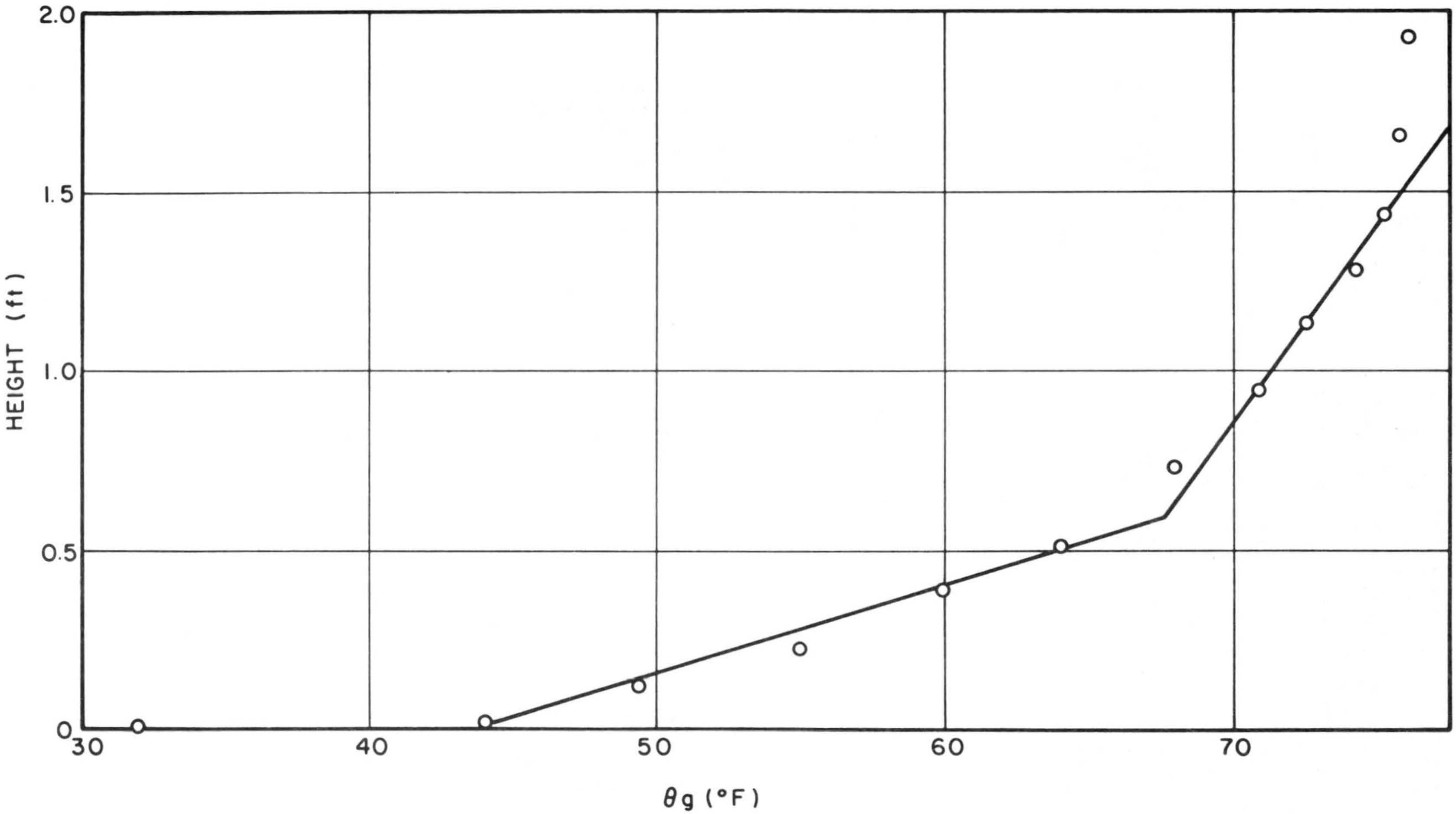

Fig. 31 Undisturbed temperature profile of flow with Fr = 0.308

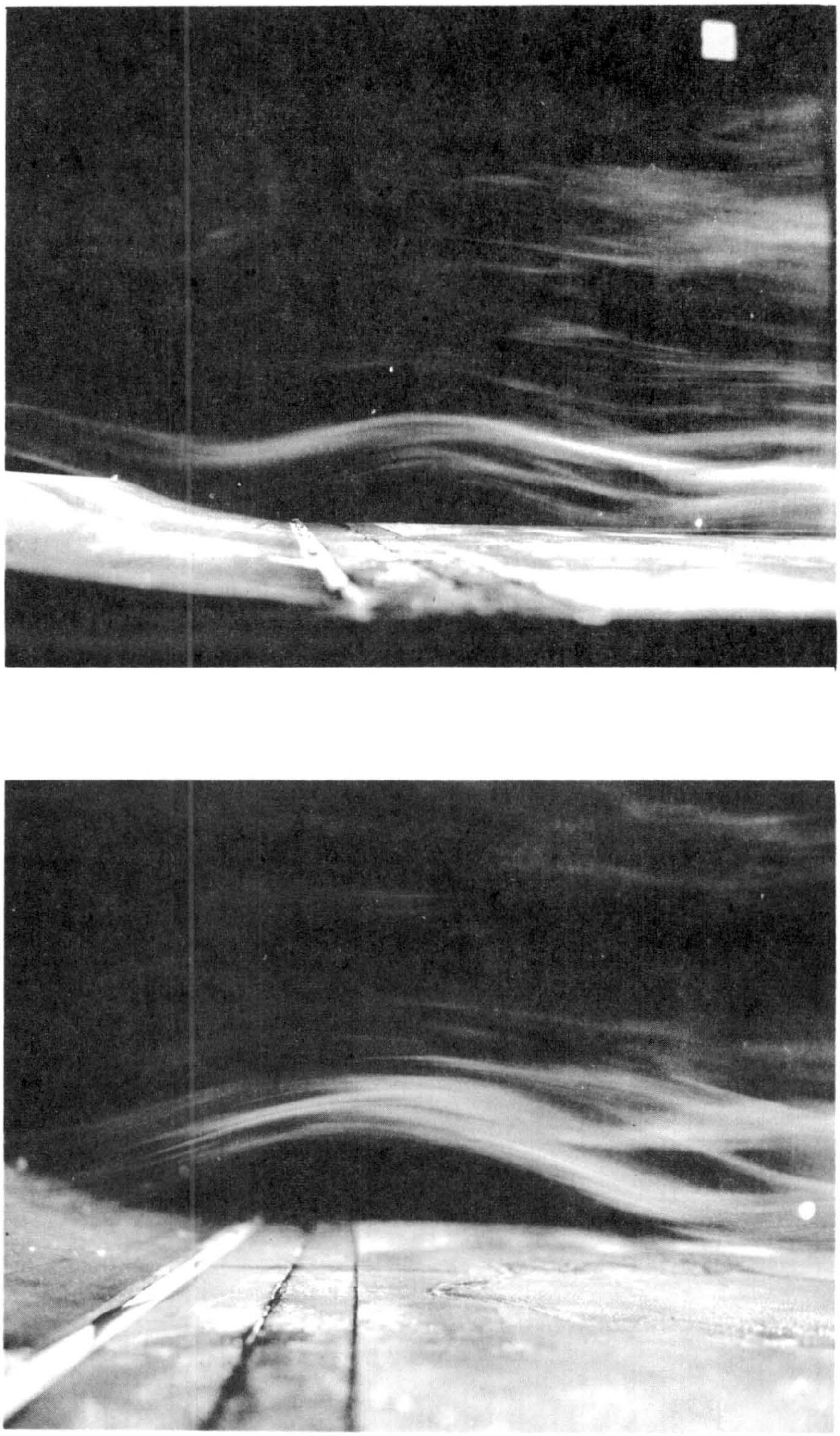

Fig. 32 Observed flow over model I
Fr = 0.308, H = 0.6 ft, U = 0.35 ft/sec
$(1/\overline{\theta})\ (d\theta/dz) = 0.111\ ft^{-1}$

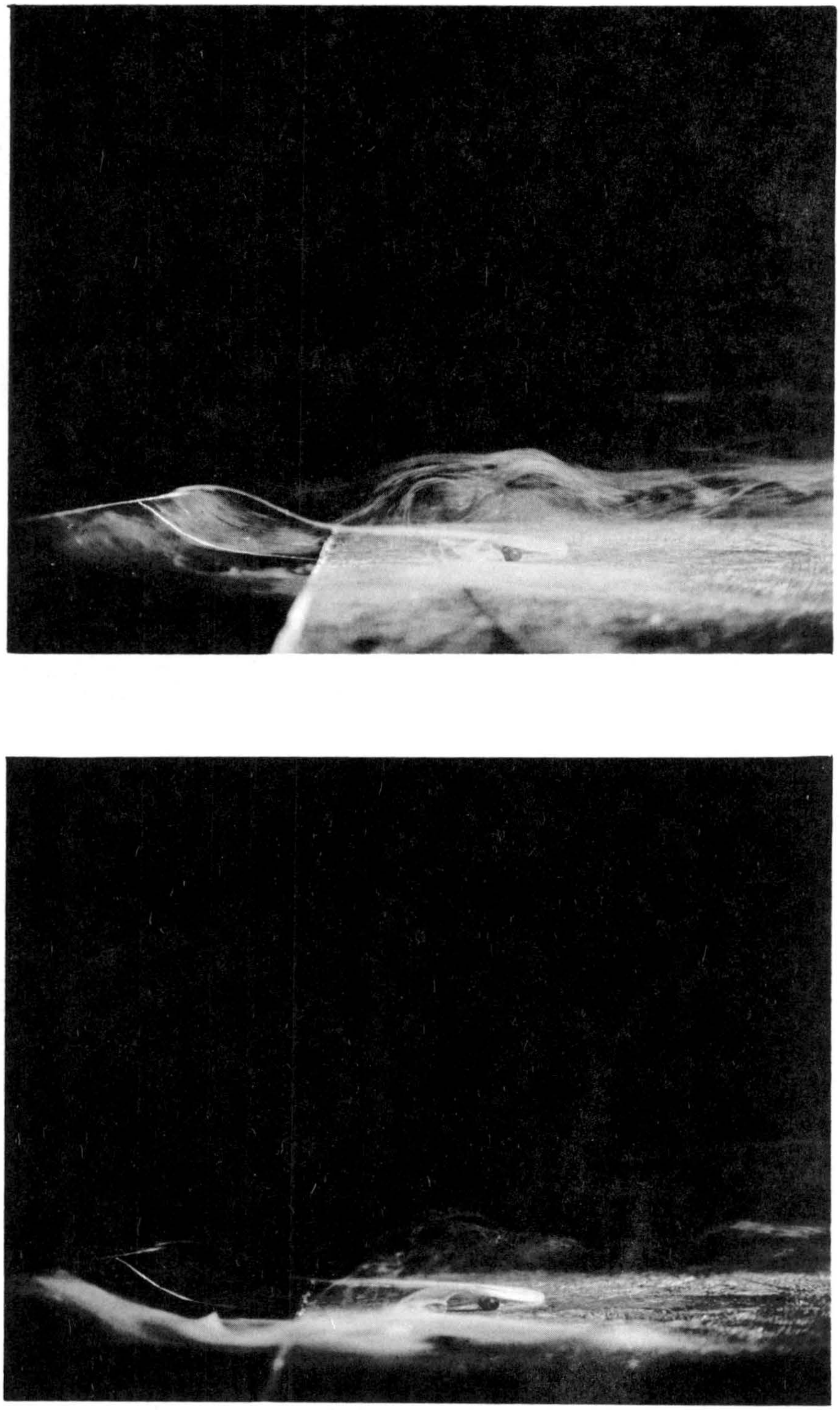

Fig. 33 Observed flow over model II
$Fr = 0.3$, $H = 0.6$ ft, $U = 0.31$ ft/sec
$(1/\overline{\theta})\ (d\theta/dz) = 0.0922\ ft^{-1}$

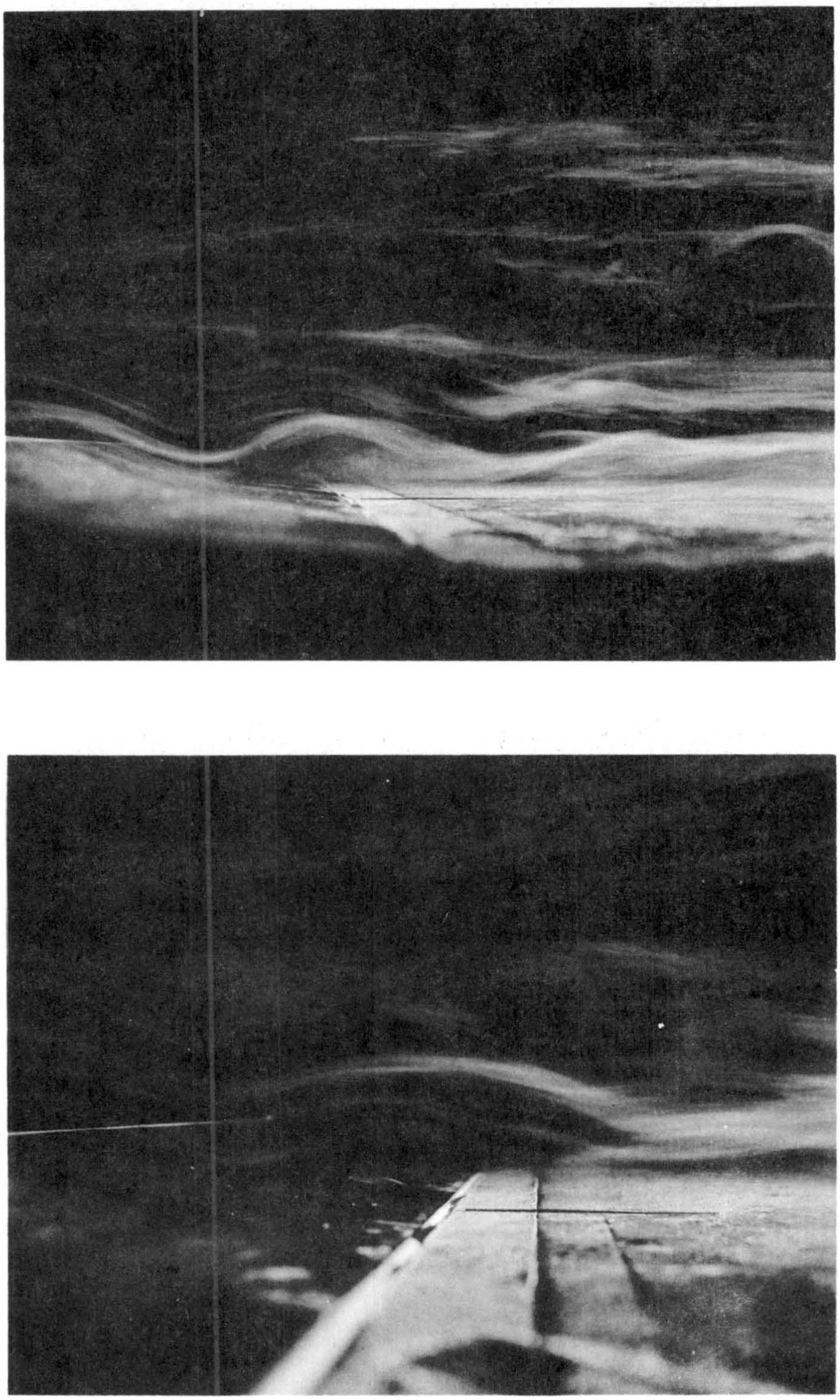

Fig. 34 Observed flow over model I
Fr = 0.254, H = 0.6 ft, U = 0.3 ft/sec
$(1/\overline{\theta})\ (d\theta/dz) = 0.121\ ft^{-1}$

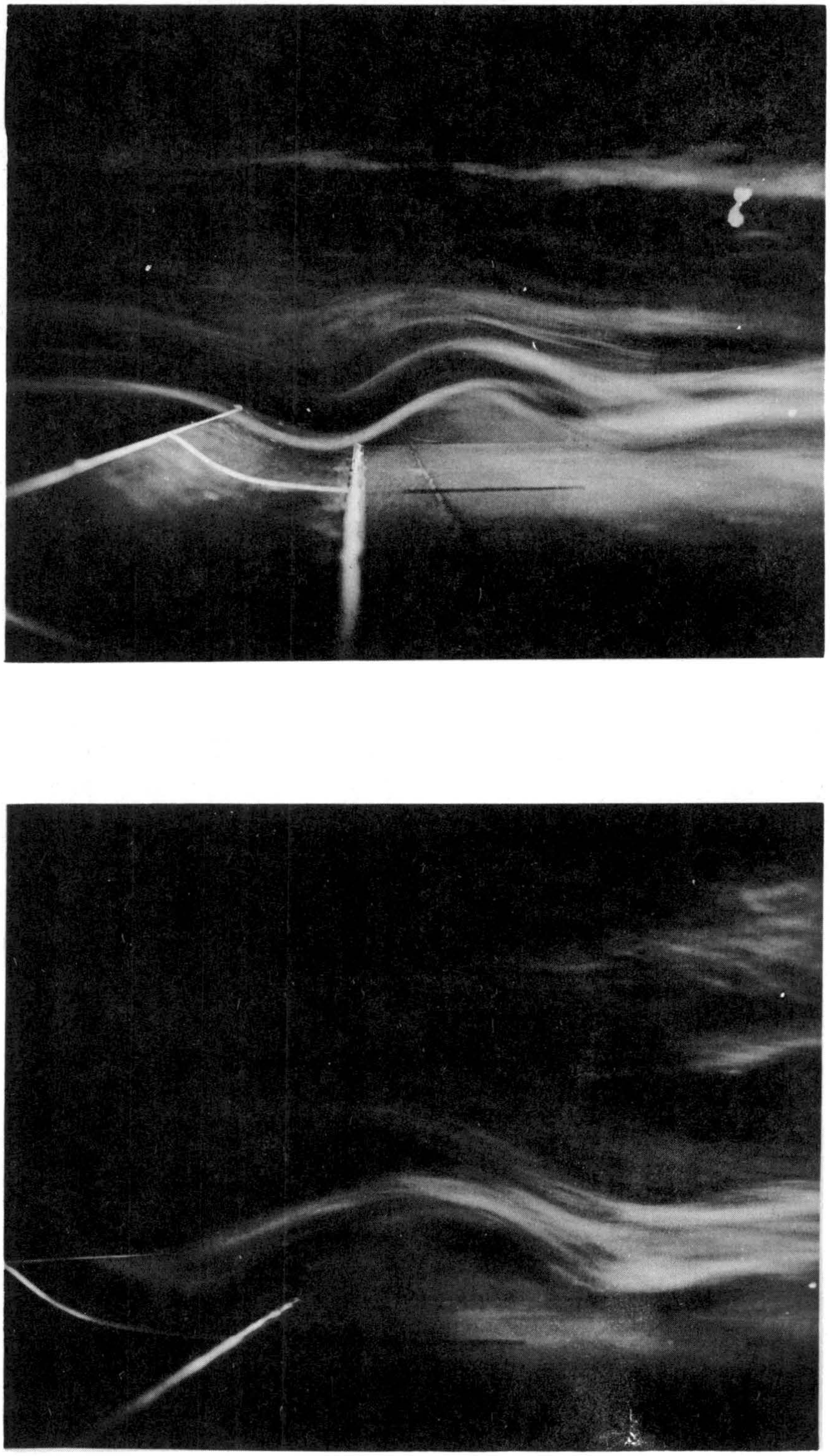

Fig. 35 Observed flow over model II
Fr = 0.247, H = 0.6 ft, U = 0.275 ft/sec
$(1/\overline{\theta})\ (d\theta/dz) = 0.107\ \mathrm{ft}^{-1}$

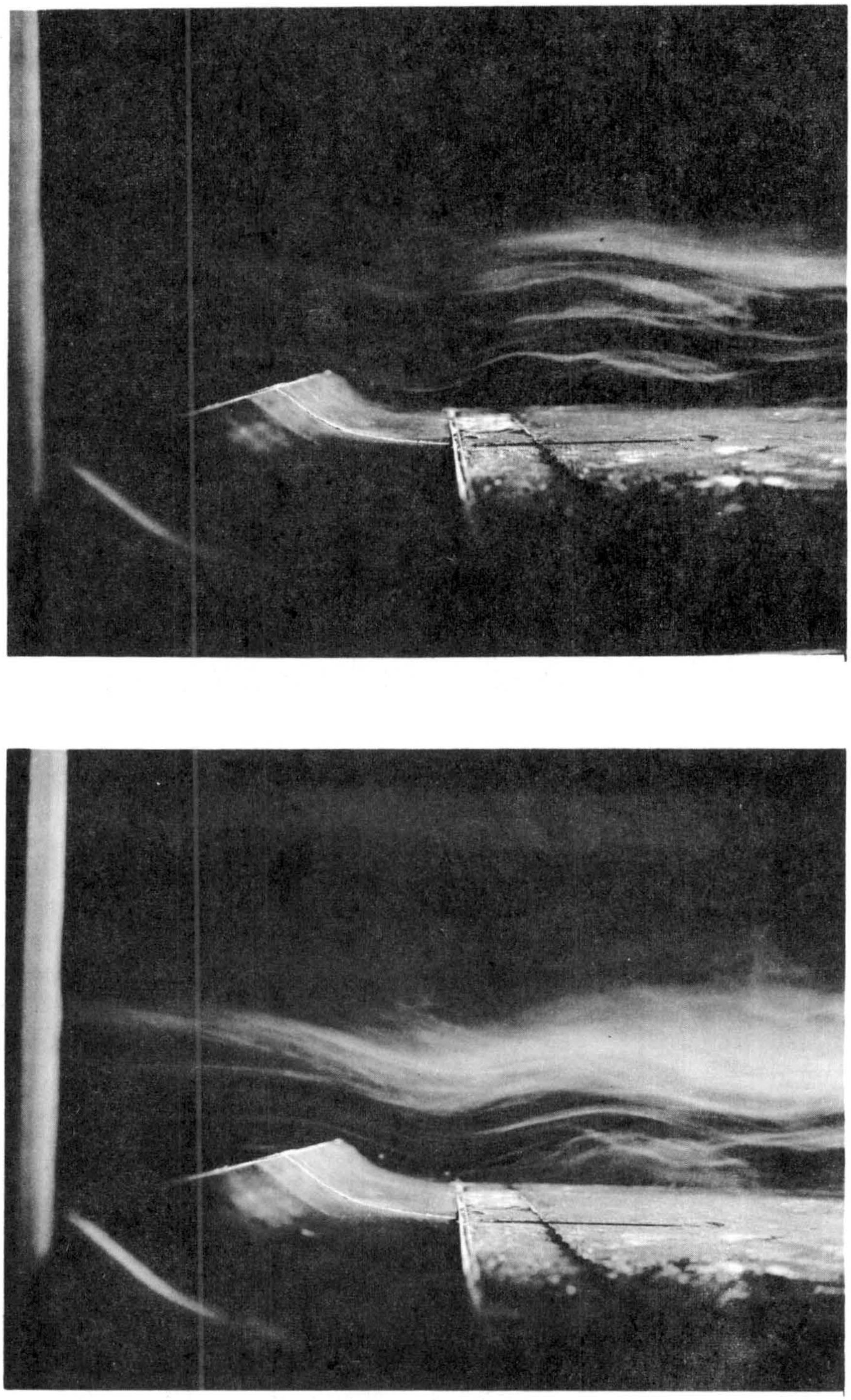

Fig. 36 Observed flow over model II
Fr = 0.238, H = 0.6 ft, U = 0.275 ft/sec
$(1/\bar{\theta})\ (d\theta/dz) = 0.115\ ft^{-1}$

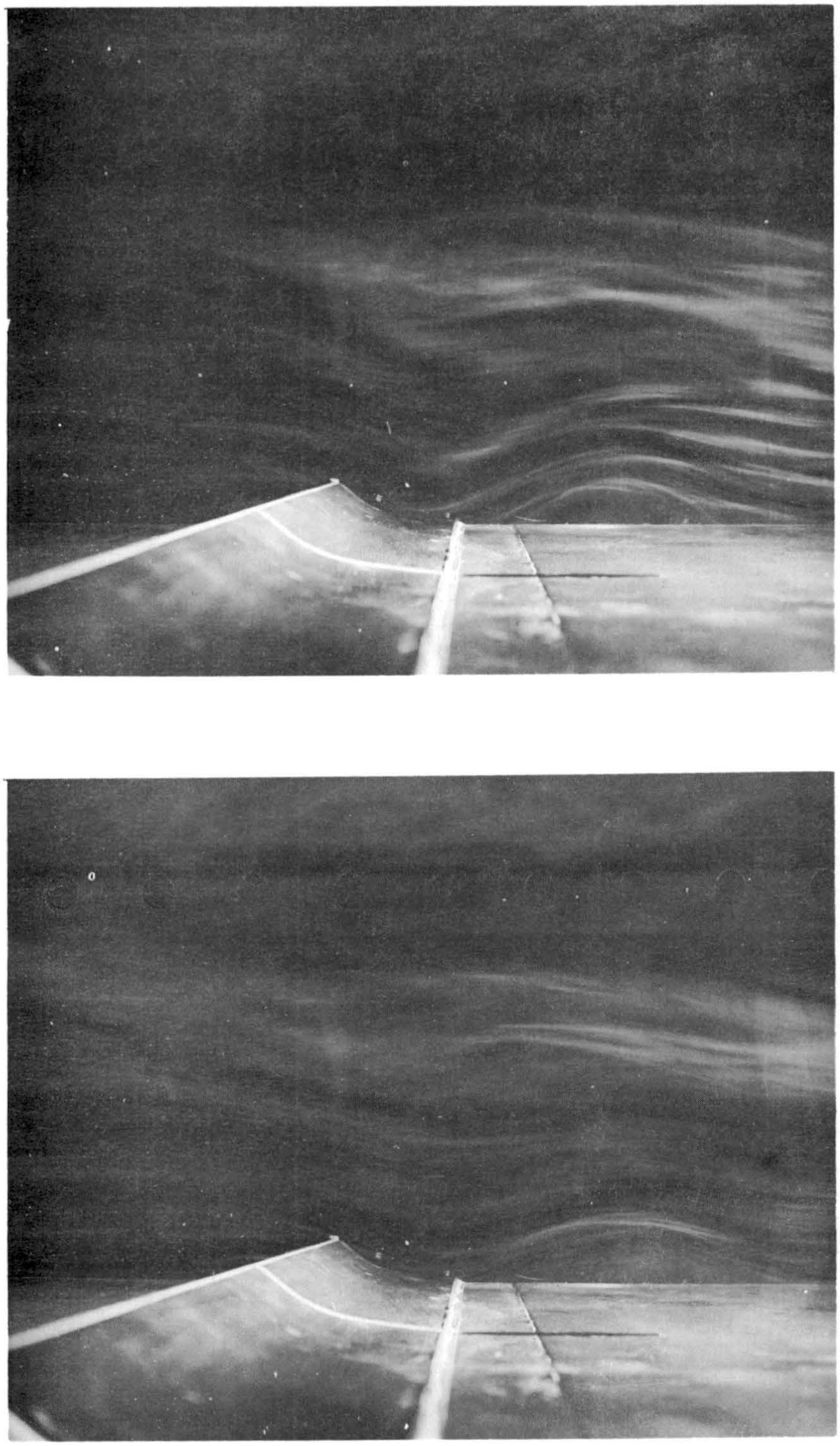

Fig. 37 Observed flow over model II
$Fr = 0.225$, $H = 0.6$ ft, $U = 0.24$ ft/sec
$(1/\overline{\theta})\ (d\theta/dz) = 0.0975\ ft^{-1}$

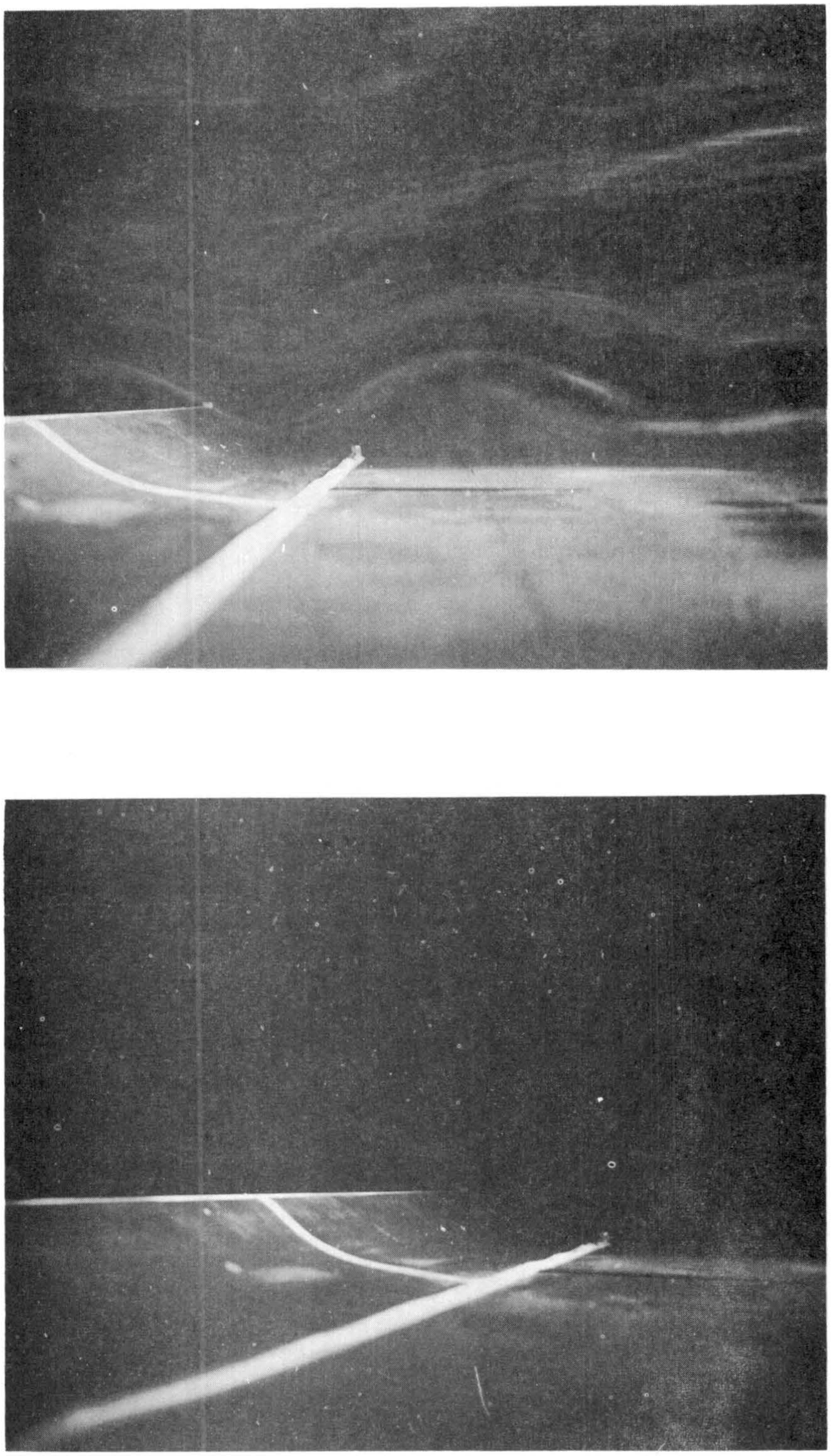

Fig. 38 Observed flow over model II
Fr = 0.214, H = 0.6 ft, U = 0.25 ft/sec
$(1/\overline{\theta})\ (d\theta/dz) = 0.118\ ft^{-1}$

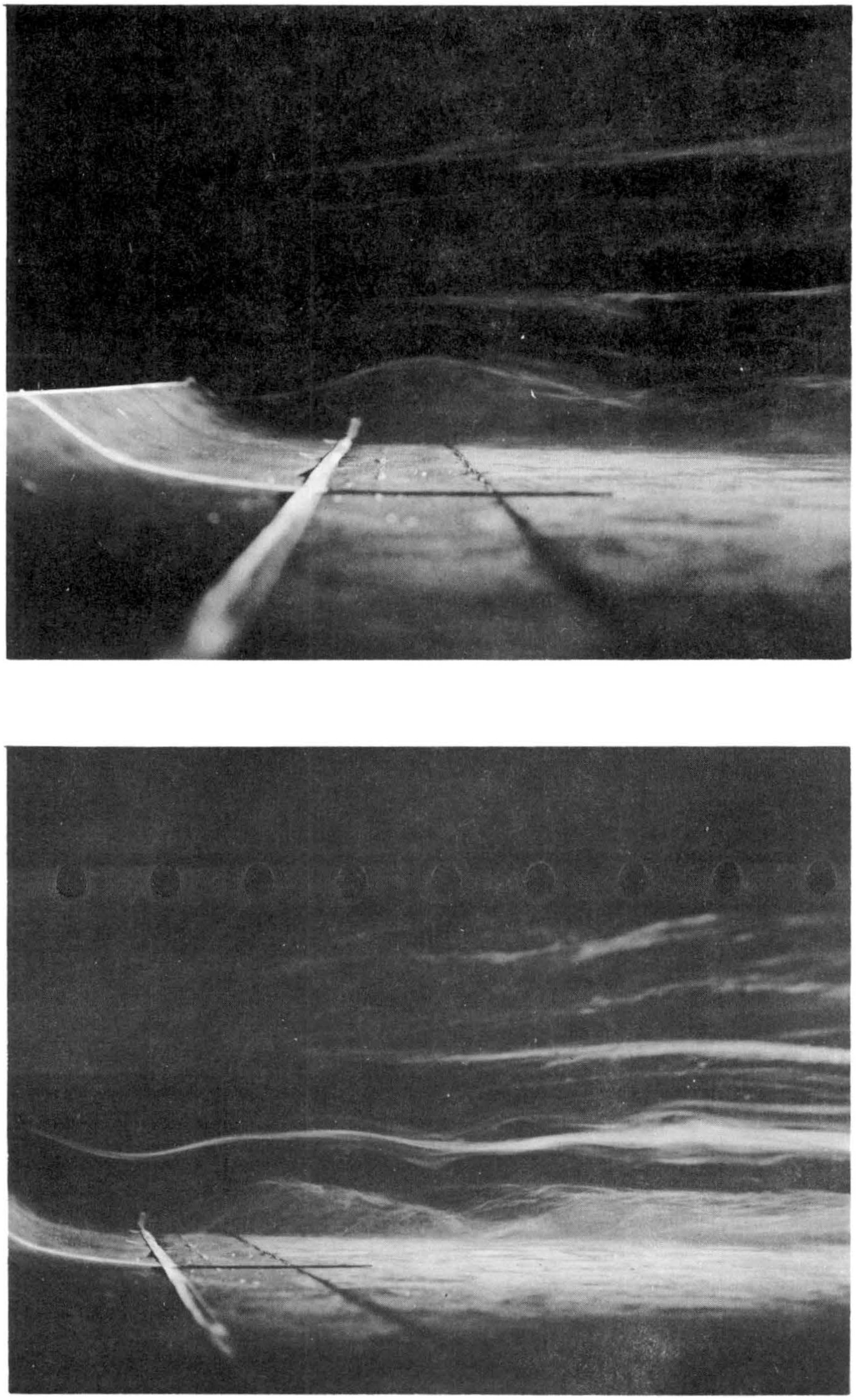

Fig. 39 Observed flow over model II
Fr = 0.205, H = 0.6 ft, U = 0.25 ft/sec
$(1/\bar{\theta})\ (d\theta/dz) = 0.128\ ft^{-1}$

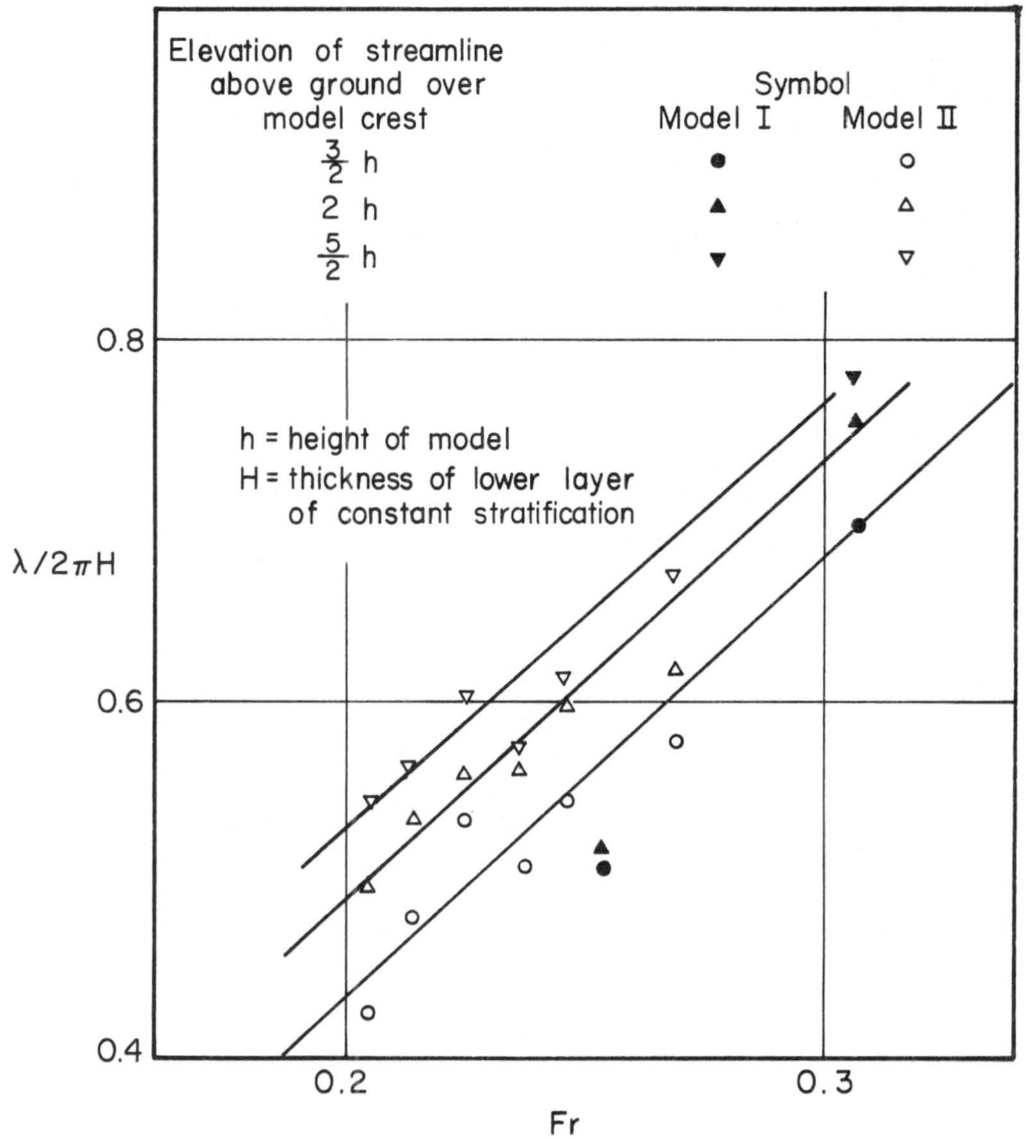

Fig. 40 Lee-wave lengths at different elevations as a function of Froude number

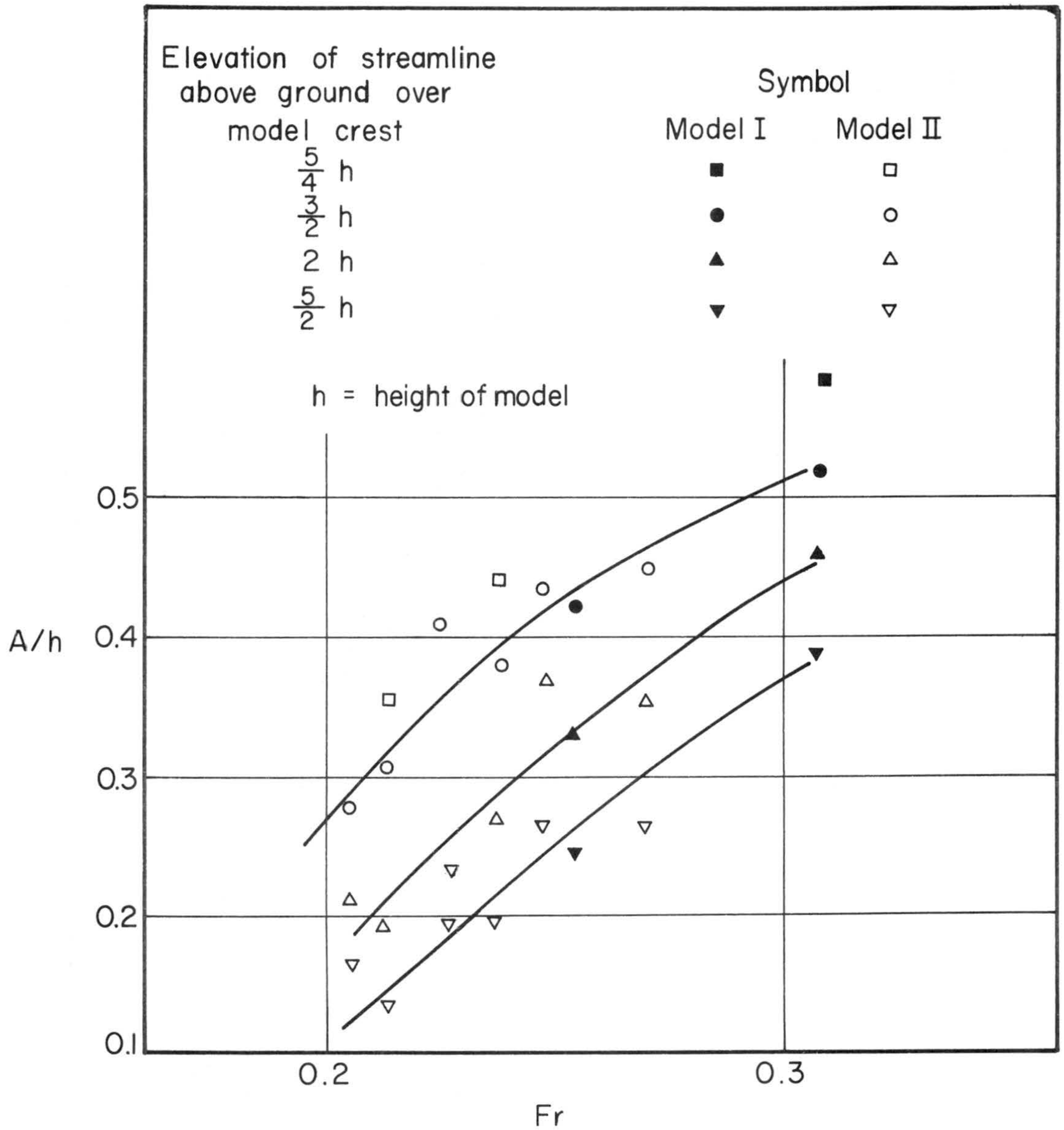

Fig. 41 Lee-wave amplitudes at different elevations as a function of Froude number

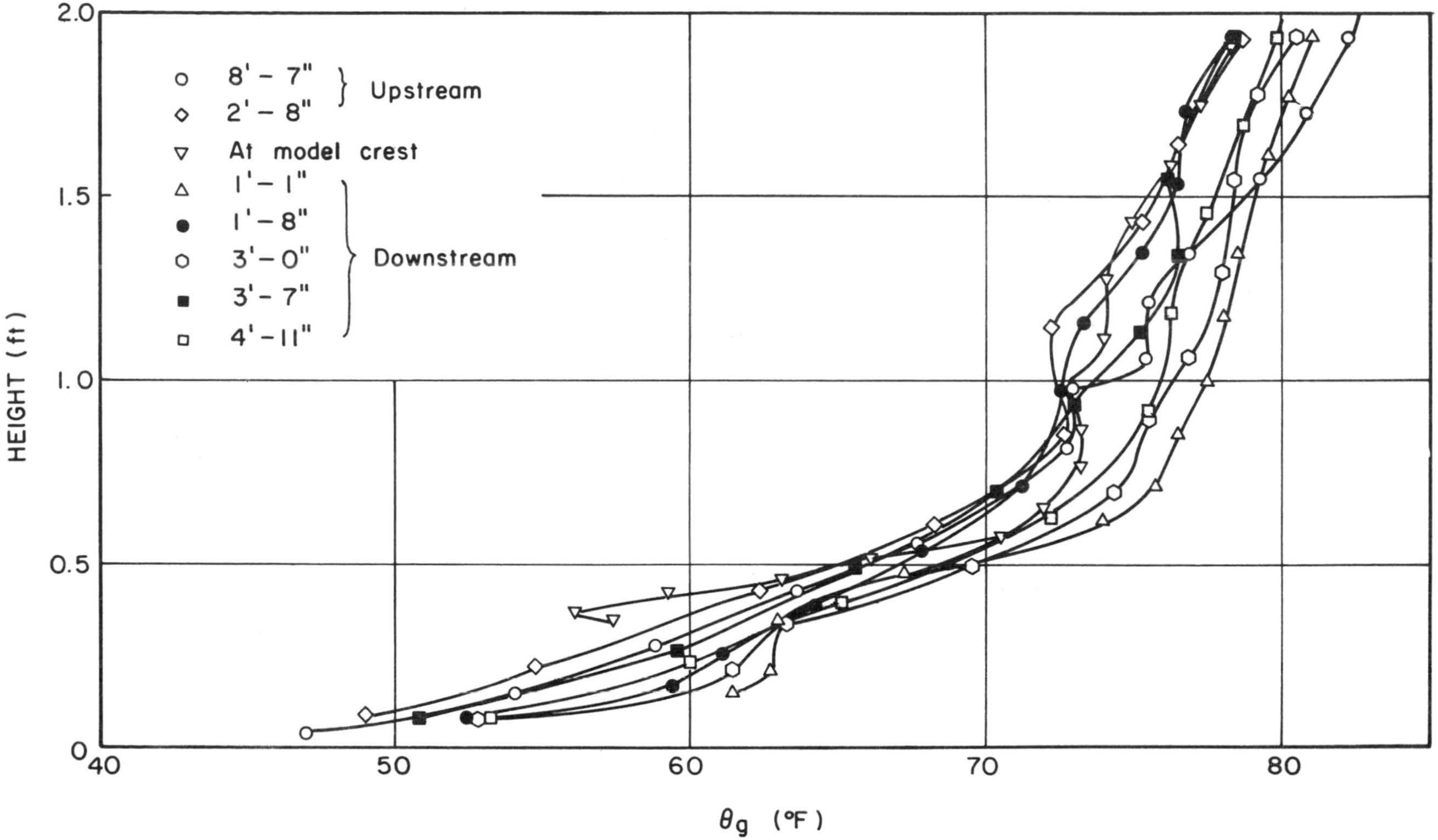

Fig. 42 Temperature profiles of flow with Fr = 0.254

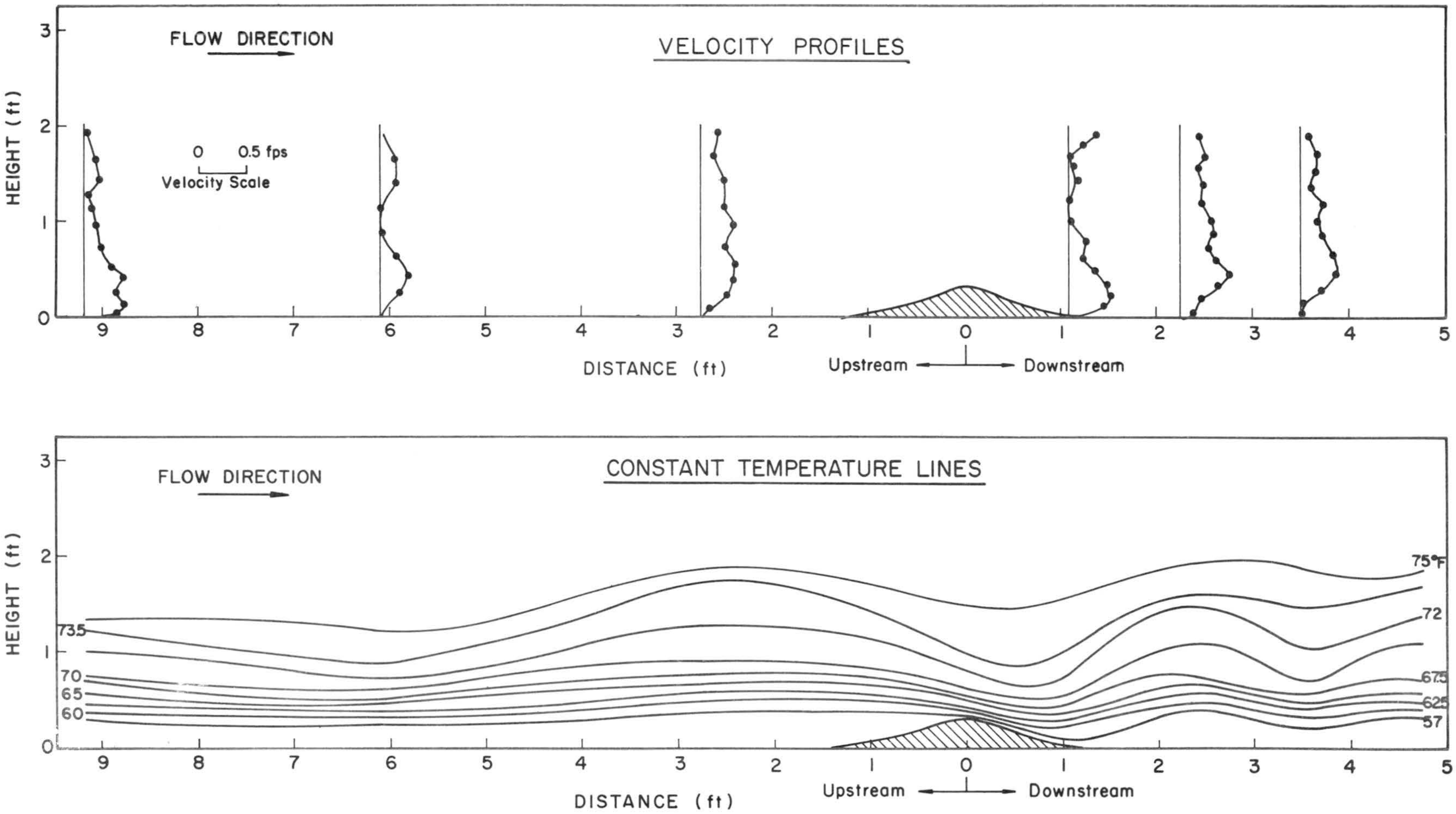

Fig. 43 Constant temperature lines and velocity profiles
$Fr = 0.308$, $U = 0.35$ ft/sec, $H = 0.6$ ft
$(1/\overline{\theta})\ (d\theta/dz) = 0.111\ ft^{-1}$

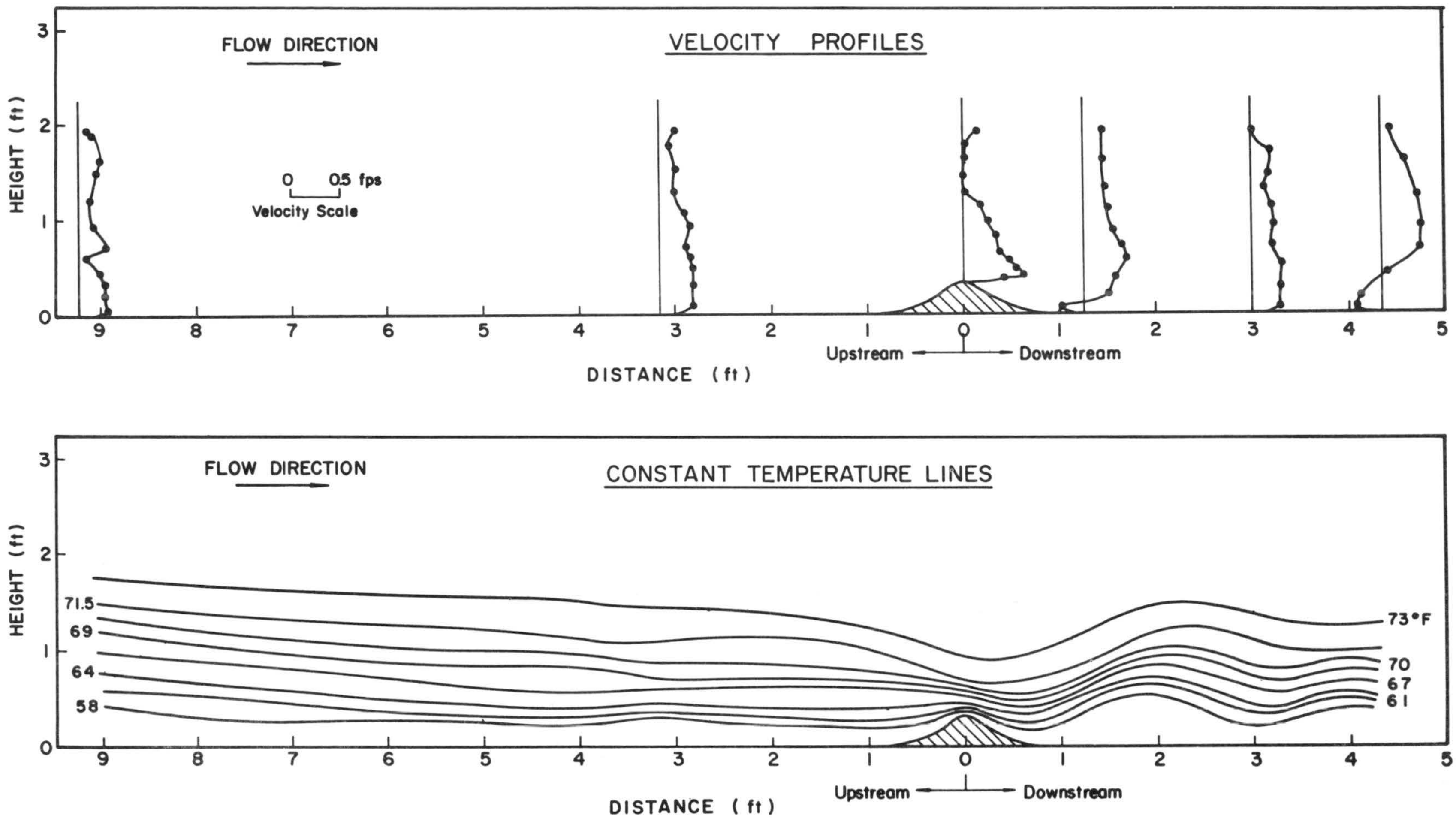

Fig. 44 Constant temperature lines and velocity profiles
$Fr = 0.284$, $U = 0.3$ ft/sec, $H = 0.6$ ft
$(1/\overline{\theta})\ (d\theta/dz) = 0.0962\ ft^{-1}$

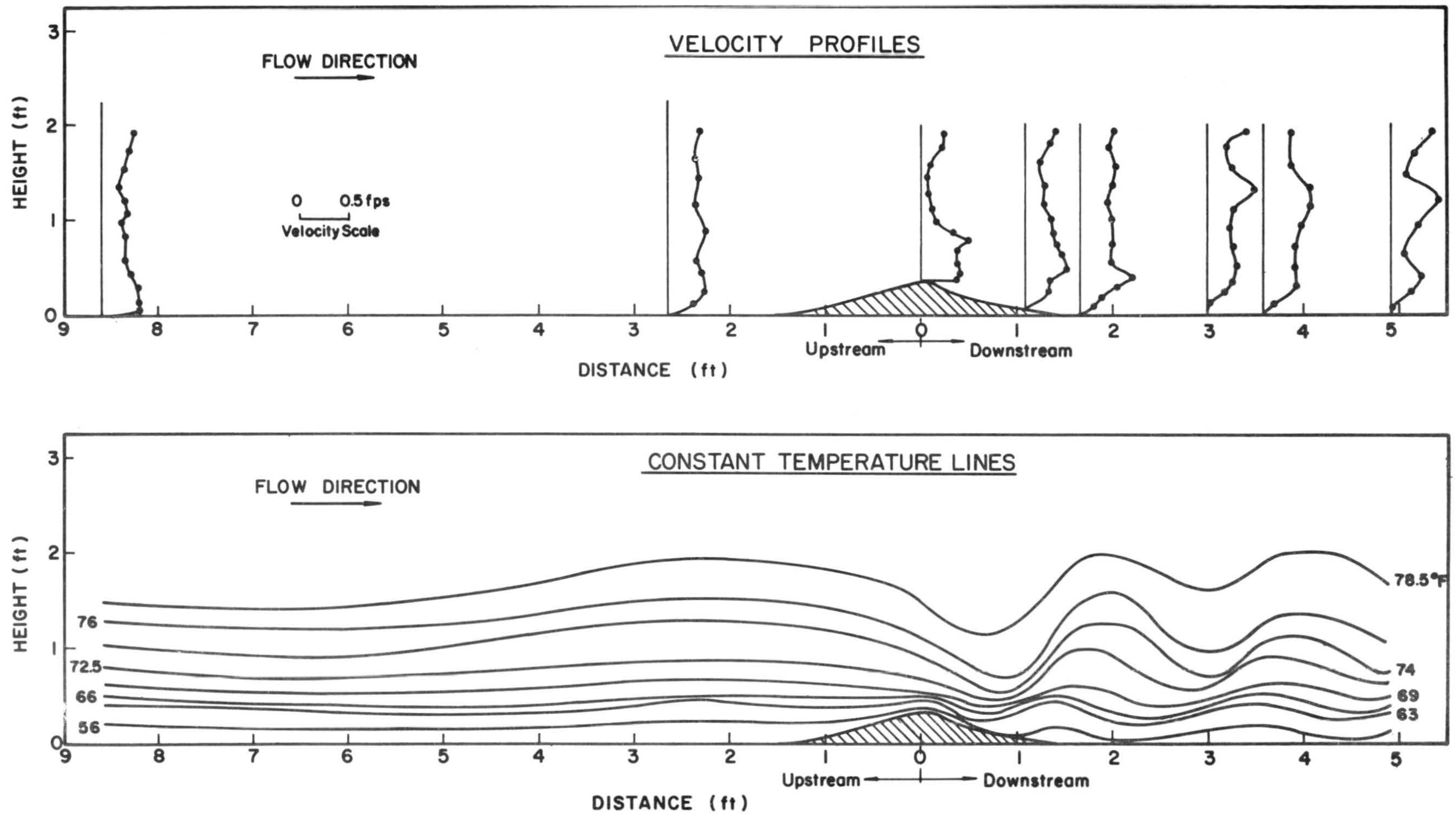

Fig. 45 Constant temperature lines and velocity profiles
Fr = 0.254, U = 0.3 ft/sec, H = 0.6 ft
$(1/\overline{\theta})\ (d\theta/dz) = 0.121\ ft^{-1}$

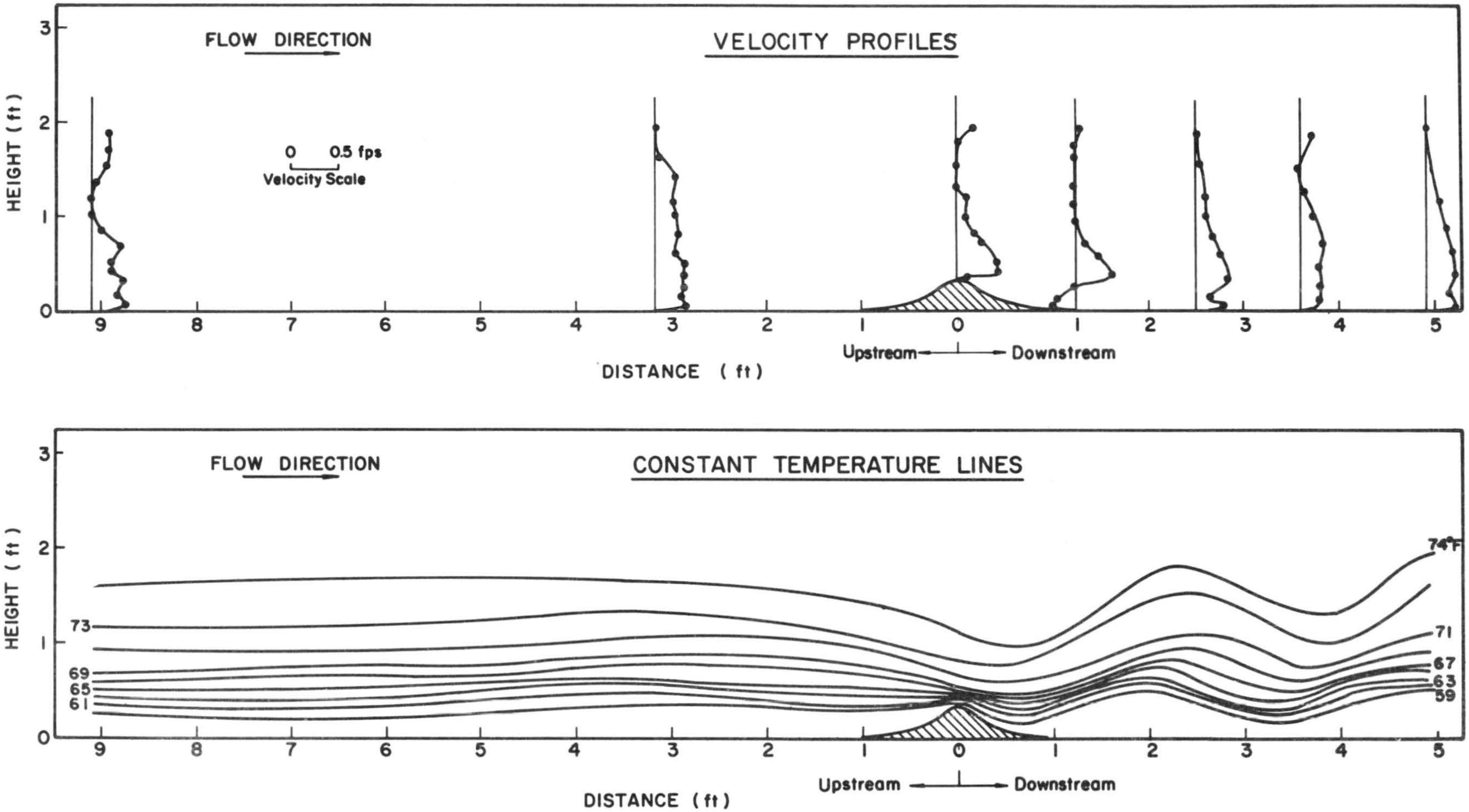

Fig. 46 Constant temperature lines and velocity profiles
Fr = 0.238, U = 0.275 ft/sec, H = 0.6 ft
$(1/\overline{\theta})\ (d\theta/dz) = 0.115\ ft^{-1}$

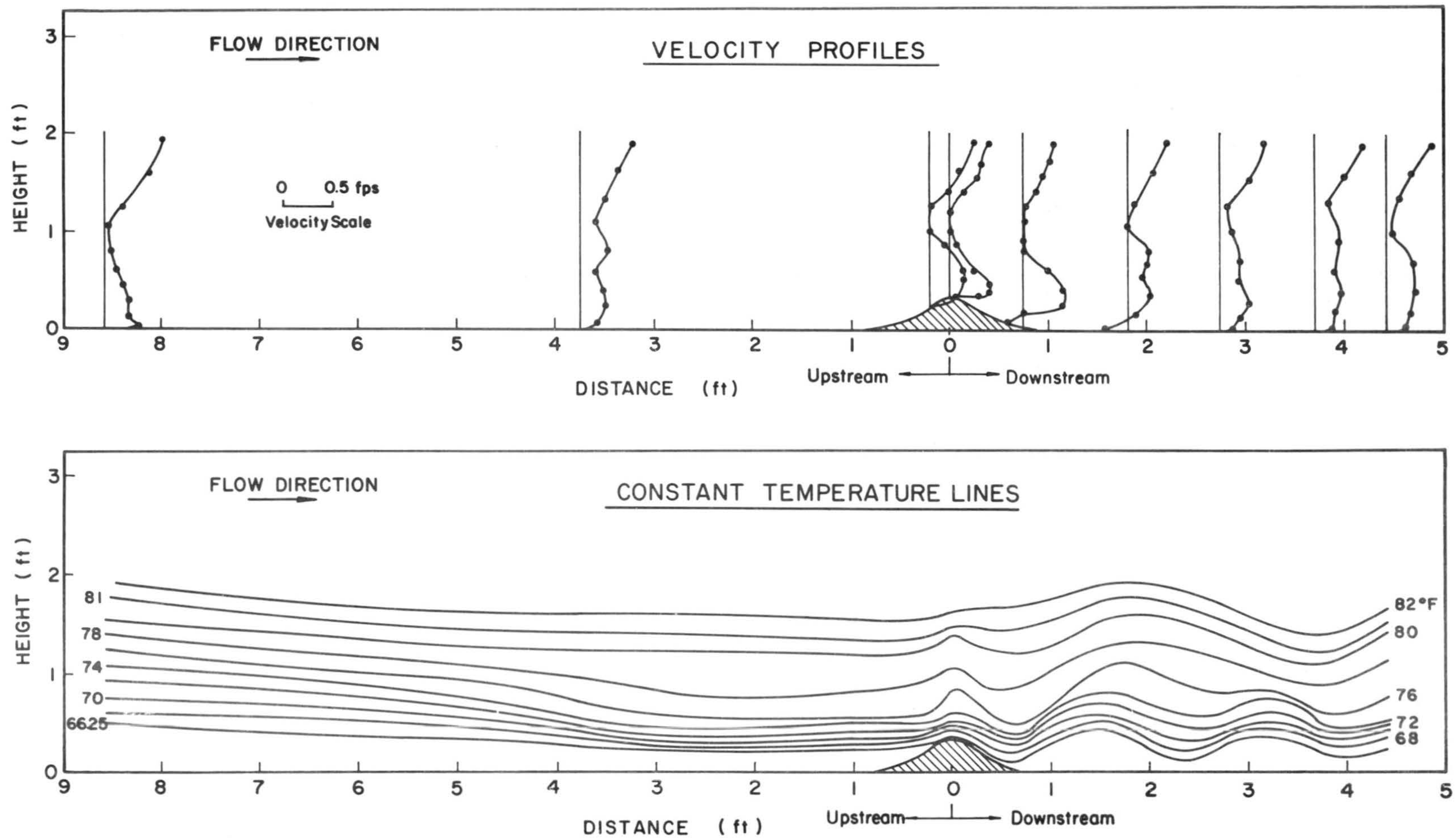

Fig. 47 Constant temperature lines and velocity profiles
$Fr = 0.214$, $U = 0.25$ ft/sec, $H = 0.6$ ft
$(1/\overline{\theta})\ (d\theta/dz) = 0.118\ ft^{-1}$

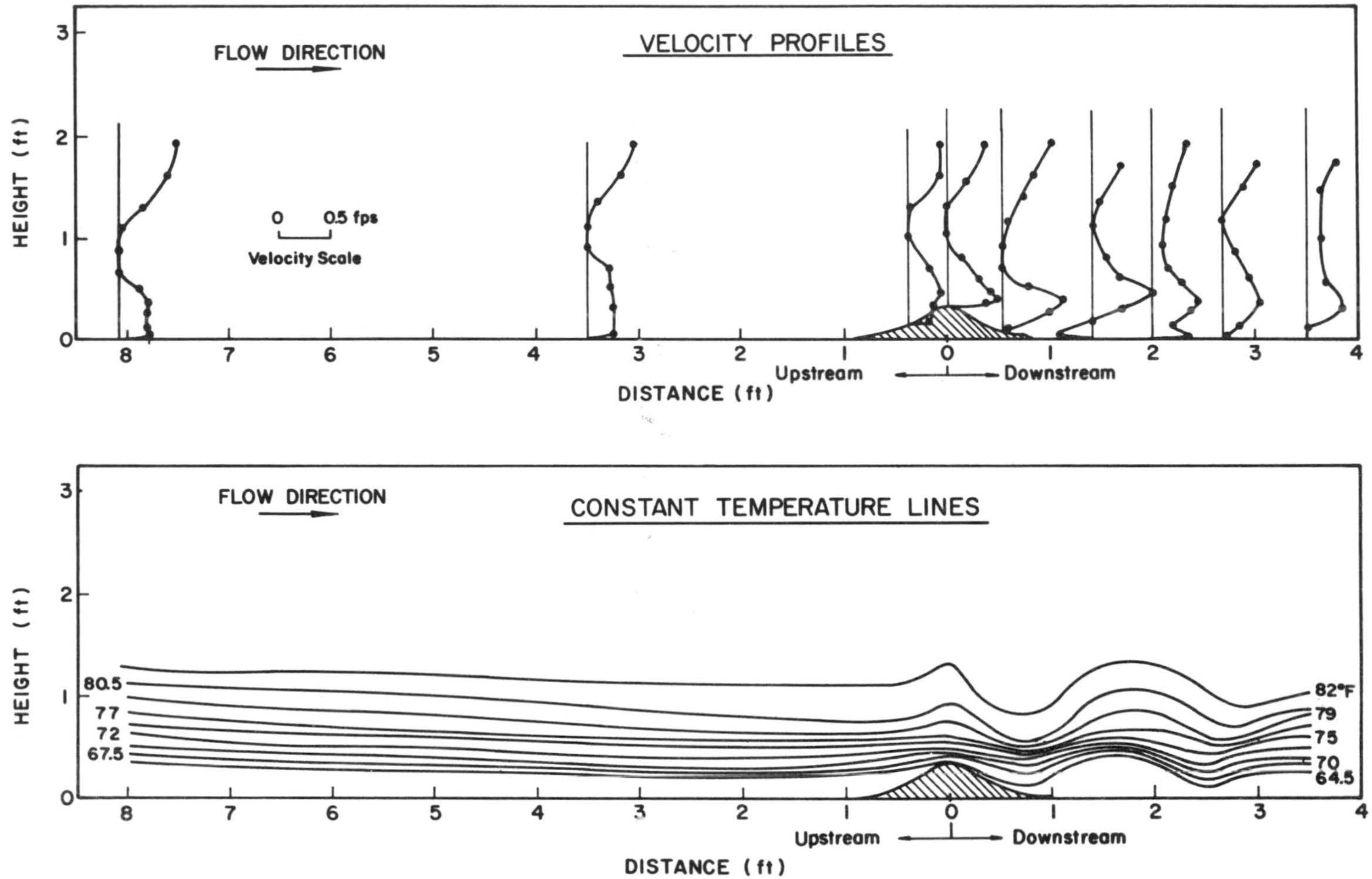

Fig. 48 Constant temperature lines and velocity profiles
$Fr = 0.205$, $U = 0.25$ ft/sec, $H = 0.6$ ft
$(1/\overline{\theta})\ (d\theta/dz) = 0.128\ ft^{-1}$

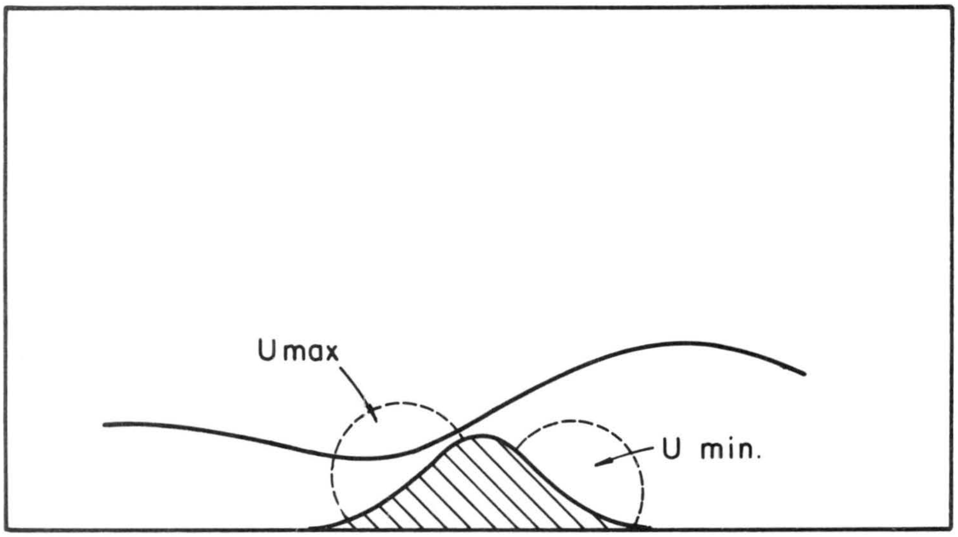

(a) SCORER – TYPE SOLUTION

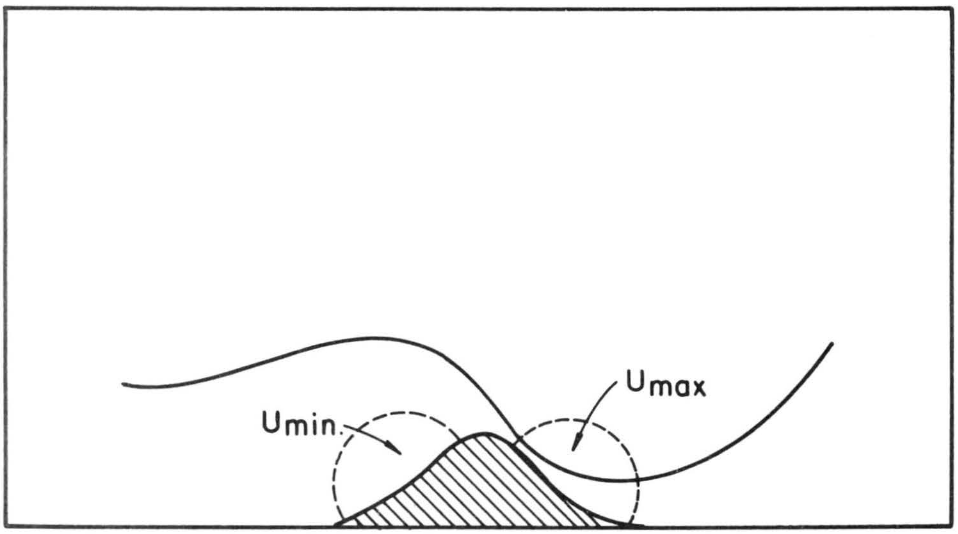

(b) QUENEY – TYPE SOLUTION

Fig. 49 Sketch of lower level streamline of Queney's and Scorer's solution

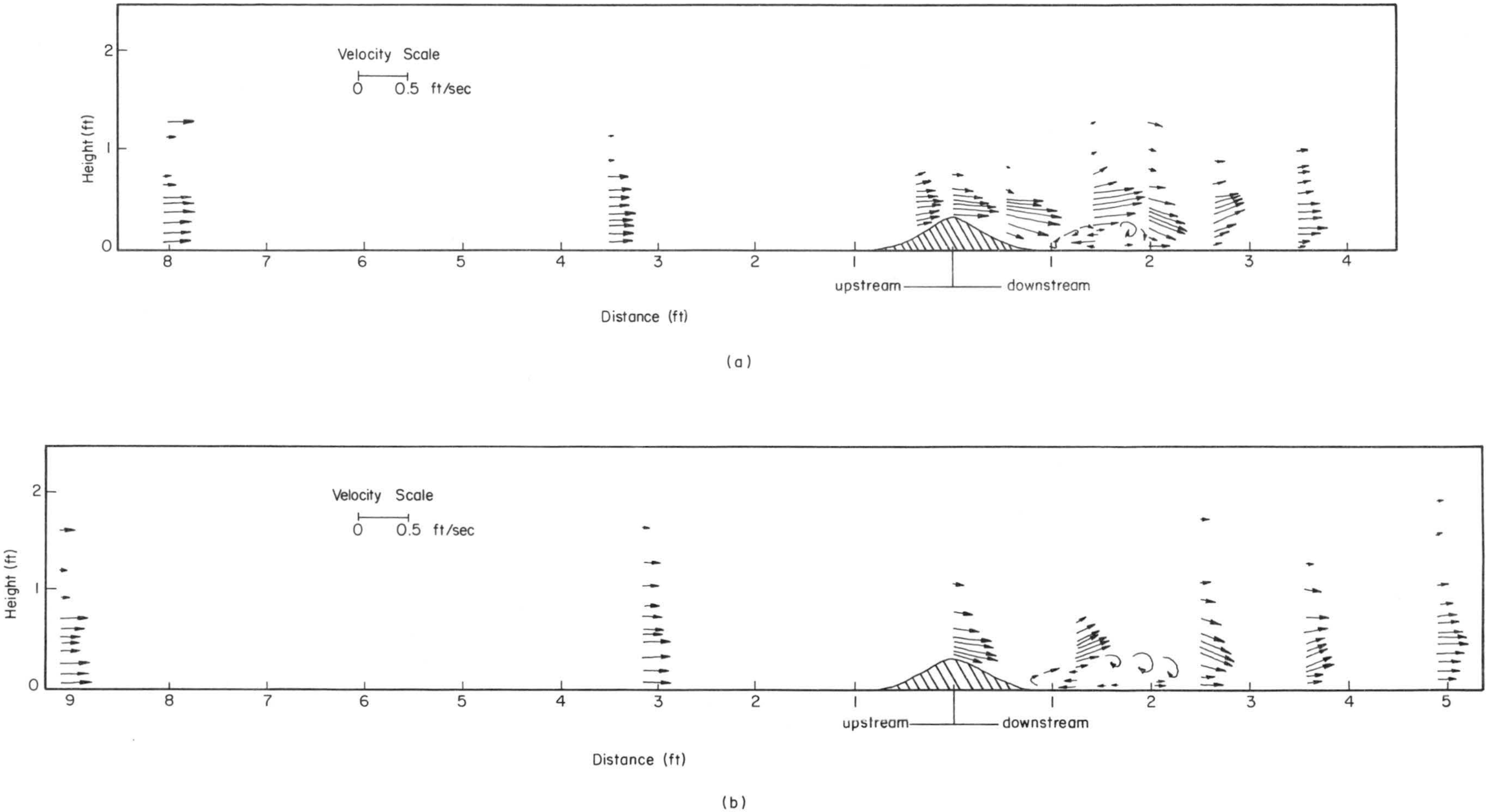

Fig. 50 Velocity fields of lee-waves
a) $Fr = 0.205$, $U = 0.25$ ft/sec, $H = 0.6$ ft
$(1/\overline{\theta})\ (d\theta/dz) = 0.128\ ft^{-1}$
b) $Fr = 0.238$, $U = 0.275$ ft/sec, $H = 0.6$ ft
$(1/\overline{\theta})\ (d\theta/dz = 0.115\ ft^{-1}$

Unclassified

Security Classification

DOCUMENT CONTROL DATA - R&D

(Security classification of title, body of abstract and indexing annotation must be entered when the overall report is classified)

1. ORIGINATING ACTIVITY (Corporate author) Fluid Mechanics Program, College of Engineering Colorado State University, Fort Collins, Colorado	2a REPORT SECURITY CLASSIFICATION Unclassified 2b GROUP

3. REPORT TITLE

SIMULATION OF MOUNTAIN LEE WAVES IN A WIND TUNNEL

4. DESCRIPTIVE NOTES *(Type of report and inclusive dates)*

Technical Report

5. AUTHOR(S) *(Last name, first name, initial)*

Lin, J. T.

Binder, G. J.

6. REPORT DATE	7a. TOTAL NO. OF PAGES	7b. NO. OF REFS
December 1967	120	32

8a. CONTRACT OR GRANT NO. DA-AMC-28-043-65-G20 b. PROJECT NO. 2246 c. d.	9a. ORIGINATOR'S REPORT NUMBER(S) CER67-68JTL-GJB24 9b. OTHER REPORT NO(S) (Any other numbers that may be assigned this report)

10. AVAILABILITY/LIMITATION NOTICES

Distribution of This Document is Unlimited

11. SUPPLEMENTARY NOTES	12. SPONSORING MILITARY ACTIVITY
	U.S. Army Materiel Command

13. ABSTRACT

Mountain lee-waves were simulated in a wind tunnel where the density stratification was produced by heating the ambient air and cooling the lower boundary. The flow patterns were visualized with smoke and were also determined from mapping of the temperature fields measured point by point with thermocouples and platinum resistance thermometers.

The magnitudes of the velocities were measured with a constant temperature hot-wire anemometer. Since this instrument is also temperature sensitive the compensation of this effect at very low velocities (the actual velocities were about 0.5 ft/sec) was experimentally determined.

The flow was composed of two layers of which the lower one (thickness 7-8 in.) had the large stability. The Froude number was calculated on the basis of the height, stability and average velocity in the lower layer. Two bell-shaped model mountains of the same height (4 in.) but of different horizontal scales were used.

This simulation experiment reproduced all the main features of mountain lee-waves, namely the wave profile, the rotor below the crest of the first wave, the strong velocity increase on the lee slope (1.5-1.8 times the average upstream velocity). Strong turbulence was found in the upper part of the rotor. The wave length at a fixed elevation of the lee-waves was found to increase linearly with Froude number; the amplitudes did also increase with Froude number.

DD FORM 1 JAN 64 1473

Unclassified

Security Classification

Unclassified
Security Classification

14. KEY WORDS	LINK A		LINK B		LINK C	
	ROLE	WT	ROLE	WT	ROLE	WT
Mountain Lee Waves, Simulation, Atmospheric Modeling, Stratified Flows, Wind Tunnel Laboratory, Fluid Mechanics, Micrometeorology, Meso Meteorology, Hot-Wire Anemometry						

INSTRUCTIONS

1. ORIGINATING ACTIVITY: Enter the name and address of the contractor, subcontractor, grantee, Department of Defense activity or other organization *(corporate author)* issuing the report.

2*a*. REPORT SECURITY CLASSIFICATION: Enter the overall security classification of the report. Indicate whether "Restricted Data" is included. Marking is to be in accordance with appropriate security regulations.

2*b*. GROUP: Automatic downgrading is specified in DoD Directive 5200.10 and Armed Forces Industrial Manual. Enter the group number. Also, when applicable, show that optional markings have been used for Group 3 and Group 4 as authorized.

3. REPORT TITLE: Enter the complete report title in all capital letters. Titles in all cases should be unclassified. If a meaningful title cannot be selected without classification, show title classification in all capitals in parenthesis immediately following the title.

4. DESCRIPTIVE NOTES: If appropriate, enter the type of report, e.g., interim, progress, summary, annual, or final. Give the inclusive dates when a specific reporting period is covered.

5. AUTHOR(S): Enter the name(s) of author(s) as shown on or in the report. Enter last name, first name, middle initial. If military, show rank and branch of service. The name of the principal author is an absolute minimum requirement.

6. REPORT DATE: Enter the date of the report as day, month, year; or month, year. If more than one date appears on the report, use date of publication.

7*a*. TOTAL NUMBER OF PAGES: The total page count should follow normal pagination procedures, i.e., enter the number of pages containing information.

7*b*. NUMBER OF REFERENCES: Enter the total number of references cited in the report.

8*a*. CONTRACT OR GRANT NUMBER: If appropriate, enter the applicable number of the contract or grant under which the report was written.

8*b*, 8*c*, & 8*d*. PROJECT NUMBER: Enter the appropriate military department identification, such as project number, subproject number, system numbers, task number, etc.

9*a*. ORIGINATOR'S REPORT NUMBER(S): Enter the official report number by which the document will be identified and controlled by the originating activity. This number must be unique to this report.

9*b*. OTHER REPORT NUMBER(S): If the report has been assigned any other report numbers *(either by the originator or by the sponsor)*, also enter this number(s).

10. AVAILABILITY/LIMITATION NOTICES: Enter any limitations on further dissemination of the report, other than those imposed by security classification, using standard statements such as:

(1) "Qualified requesters may obtain copies of this report from DDC."

(2) "Foreign announcement and dissemination of this report by DDC is not authorized."

(3) "U. S. Government agencies may obtain copies of this report directly from DDC. Other qualified DDC users shall request through
_______________________________."

(4) "U. S. military agencies may obtain copies of this report directly from DDC. Other qualified users shall request through
_______________________________."

(5) "All distribution of this report is controlled. Qualified DDC users shall request through
_______________________________."

If the report has been furnished to the Office of Technical Services, Department of Commerce, for sale to the public, indicate this fact and enter the price, if known.

11. SUPPLEMENTARY NOTES: Use for additional explanatory notes.

12. SPONSORING MILITARY ACTIVITY: Enter the name of the departmental project office or laboratory sponsoring *(paying for)* the research and development. Include address.

13. ABSTRACT: Enter an abstract giving a brief and factual summary of the document indicative of the report, even though it may also appear elsewhere in the body of the technical report. If additional space is required, a continuation sheet shall be attached.

It is highly desirable that the abstract of classified reports be unclassified. Each paragraph of the abstract shall end with an indication of the military security classification of the information in the paragraph, represented as *(TS)*, *(S)*, *(C)*, or *(U)*.

There is no limitation on the length of the abstract. However, the suggested length is from 150 to 225 words.

14. KEY WORDS: Key words are technically meaningful terms or short phrases that characterize a report and may be used as index entries for cataloging the report. Key words must be selected so that no security classification is required. Identifiers, such as equipment model designation, trade name, military project code name, geographic location, may be used as key words but will be followed by an indication of technical context. The assignment of links, rules, and weights is optional.

Unclassified
Security Classification

MINIMUM BASIC DISTRIBUTION LIST FOR USAMC SCIENTIFIC AND TECHNICAL REPORTS IN METEOROLOGY AND ATMOSPHERIC SCIENCES

Commanding General (1)
U. S. Army Materiel Command
Attn: AMCRD-RV-A
Washington, D. C. 20315

Commanding General (1)
U. S. Army Electronics Command
Attn: AMSEL-EW
Fort Monmouth, New Jersey 07703

Commanding General (1)
U. S. Army Test and Evaluation Command
Attn: NBC Directorate
Aberdeen Proving Ground, Maryland 21005

Commanding Officer (1)
U. S. Army Ballistics Research Laboratories
Attn: AMXBR-IA
Aberdeen Proving Ground, Maryland 21005

Chief, Atmospheric Physics Division (2)
Atmospheric Sciences Laboratory
U. S. Army Electronics Command
Fort Monmouth, New Jersey 07703

U. S. Army Munitions Command (1)
Attn: Irving Solomon
Operations Research Group
Edgewood Arsenal, Maryland 21010

Commanding Officer (1)
U. S. Army Dugway Proving Ground
Attn: Meteorology Division
Dugway, Utah 84022

Commanding Officer (1)
U. S. Army CDC, CBR Agency
Attn: Mr. N. W. Bush
Fort McClellan, Alabama 36205

Commanding General (1)
U. S. Army Test and Evaluation Command
Attn: AMSTE-EL
Aberdeen Proving Ground, Maryland 21005

Commandant (1)
U. S. Army Signal School
Attn: Meteorological Department
Fort Monmouth, New Jersey 07703

Assistant Chief of Staff for Force Development (1)
CBR Nuclear Operations Directorate
Department of the Army
Washington, D. C. 20310

Director (1)
Atmospheric Sciences Programs
National Sciences Foundation
Washington, D. C. 20550

Assistant Secretary of Defense (1)
Research and Engineering
Attn: Technical Library
Washington, D. C. 20301

R. A. Taft Sanitary Engineering Center (1)
Public Health Service
4676 Columbia Parkway
Cincinnati, Ohio

Dr. Hans A. Panofsky (1)
Department of Meteorology
The Pennsylvania State University
University Park, Pennsylvania

Commanding General (1)
U. S. Continental Army Command
Attn: Reconnaissance Branch ODCS
for Intelligence
Fort Monroe, Virginia 23351

Commander (1)
Air Force Cambridge Research Laboratories
Attn: CRZW
1065 Main Street
Waltham, Massachusetts

President (1)
U. S. Army Artillery Board
Fort Sill, Oklahoma 73504

National Center for Atmospheric Research (1)
Attn: Library
Boulder, Colorado

Dr. J. E. Cermak, Head (15)
Fluid Mechanics Program
Colorado State University
Fort Collins, Colorado 80521

Author (1)

Chief of Research and Development (1)
Department of the Army
Attn: CRD/M
Washington, D. C. 20310

Commanding General (1)
U. S. Army Missile Command
Attn: AMSMI-RRA
Redstone Arsenal, Alabama 35809

Commanding General (1)
U. S. Army Natick Laboratories
Attn: Earth Sciences Division
Natick, Massachusetts 01762

Director, U. S. Army Engineer (1)
Waterways Experiment Station
Attn: WES-FV
Vicksburg, Mississippi 39181

Chief, Atmospheric Sciences Research Division (5)
Atmospheric Sciences Laboratory
U. S. Army Electronics Command
Fort Huachuca, Arizona 85613

Commanding Officer (1)
U. S. Army Frankford Arsenal
Attn: SMUFA-1140
Philadelphia, Pennsylvania 19137

Commandant (1)
U. S. Army Artillery and Missile School
Attn: Target Acquisition Department
Fort Sill, Oklahoma 73504

Commanding General (1)
U. S. Army Electronics Proving Ground
Attn: Field Test Department
Fort Huachuca, Arizona 85613

Commanding General (1)
U. S. Army Test and Evaluation Command
Attn: AMSTE-BAF
Aberdeen Proving Ground, Maryland 21005

Office of Chief Communications - Electronics (1)
Department of the Army
Attn: Electronics Systems Directorate
Washington, D. C. 20315

Chief of Naval Operations (1)
Department of the Navy
Attn: Code 427
Washington, D. C. 20350

Director (1)
Bureau of Research and Development
Federal Aviation Agency
Washington, D. C. 20553

Director of Meteorological Systems (1)
Office of Applications (FM)
National Aeronautics and Space Administration
Washington, D. C. 20546

Director (1)
Atmospheric Physics and Chemistry Laboratory
Environmental Science Services Administration
Boulder, Colorado

Andrew Morse (1)
Army Aeronautical Activity
Ames Research Center
Moffett Field, California 94035

Commanding Officer (2)
U. S. Army Cold Regions Research and
Engineering Laboratories
Attn: Environmental Research Branch
Hanover, New Hampshire 03755

Mr. Ned L. Kragness (1)
U. S. Army Aviation Materiel Command
SMOSM-E
12th and Spruce Streets
Saint Louis, Missouri 63166

Commanding Officer, U. S. Army (1)
Artillery Combat Development Agency
Fort Sill, Oklahoma 73504

Commander, USAR Air Weather Service (MATS) (1)
Attn: AWSSS/TIPD
Scott Air Force Base, Illinois

Dr. John Bogusky (1)
7310 Cedardale Drive
Alexandria, Virginia 22308

Commanding General (1)
U. S. Army Combat Development Command
Attn: CDCMR-E
Fort Belvoir, Virginia 22060

Commanding General (1)
U. S. Army Munitions Command
Attn: AMSMU-RE-R
Dover, New Jersey 07801

Commanding Officer (1)
U. S. Army Ballistics Research Laboratories
Attn: AMXBR-B
Aberdeen Proving Ground, Maryland 21005

Director (2)
Atmospheric Sciences Laboratory
U. S. Army Electronics Command
Fort Monmouth, New Jersey 07703

Chief, Atmospheric Sciences Office (2)
Atmospheric Sciences Laboratory
U. S. Army Electronics Command
White Sands Missile Range, New Mexico 88002

Commanding Officer (1)
U. S. Army Picatinny Arsenal
Attn: SMUPA-TV-3
Dover, New Jersey 07801

Commanding Officer (1)
U. S. Army Communications - Electronics
Combat Development Agency
Fort Monmouth, New Jersey 07703

Commanding General (1)
Deseret Test Center
Attn: Design and Analysis Division
Fort Douglas, Utah 84113

Commandant (1)
U. S. Army CBR School Micrometeorological
Section
Fort McClellan, Alabama 36205

Assistant Chief of Staff for Intelligence (1)
Department of the Army
Attn: ACSI-DERSI
Washington, D. C. 20310

Officer in Charge (1)
U. S. Naval Weather Research Facility
U. S. Naval Air Station, Building 4-28
Norfolk, Virginia 23500

Chief, Fallout Studies Branch (1)
Division of Biology and Medicine
Atomic Energy Commission
Washington, D. C. 20545

Director (1)
U. S. Weather Bureau
Attn: Librarian
Washington, D. C. 20235

Dr. Albert Miller (1)
Department of Meteorology
San Jose State College
San Jose, California 95114

Mrs. Francis L. Wheedon (1)
Army Research Office
3045 Columbia Pike
Arlington, Virginia 22201

Commander (1)
Air Force Cambridge Research Laboratories
Attn: CRXL
L. G. Hanscom Field
Bedford, Massachusetts

Harry Moses, Asso. Meteorologist (1)
Radiological Physics Division
Argonne National Laboratory
9700 S. Cass Avenue
Argonne, Illinois 60440

Defense Documentation Center (20)
Cameron Station
Alexandria, Virginia 22314

Office of U. S. Naval Weather Service (1)
U. S. Naval Air Station
Washington, D. C. 20390

Dr. Gerald Gill (1)
University of Michigan
Ann Arbor, Michigan 48103